BOUNDARY-LAYER INVESTIGATION
ON A BODY OF REVOLUTION WITH FINS

By N. M. Burstein

Technical Memorandum
File No. TM 504.2461-07
September 15, 1965
Contract NOw 65-0123-d
Copy No. 19

# NTIS DISCLAIMER

Abstract:   The properties of the flow near the trailing edge
            of a body of revolution with fins has been
            investigated experimentally and compared with
            predicted values based on existing theories.  The
            theoretical predictions were based on the solution
            to the axisymmetric boundary-layer equations of
            Truckenbrodt and the flat-plate solution of
            Von Kármán and Pohlhausen.

            Experimental work included measurements with a
            hot-wire anemometer to determine some statistical
            properties of the randomly fluctuating velocity
            field.  These properties include correlation
            functions and their related power-spectral densities
            and steady mean values and root-mean-square values
            of the velocity fluctuations.

            Further properties of the flow field were established
            with a pitot-static tube and a vorticity meter that
            measured streamwise vorticity arising from the fin-
            and-body configuration.  Measurements were also made
            for the body with a propeller located at 0.97 per
            cent of the body length from the nose.  The results
            obtained establish that the aft fins are the major
            cause of the radial and circumferential fluctuation
            of the mean velocity, which give rise to unsteady
            forces in the propulsor.

ACKNOWLEDGMENTS

The author wishes to express his sincere appreciation for the help and guidance rendered throughout this undertaking by his advisor, Dr. Maurice Sevik. He also wishes to thank the staff of the Garfield Thomas Water Tunnel for their diligence in helping to complete this investigation: Samuel M. Laposata for his aid in computer programming; Merlin W. McBride and his tunnel-operating crew for their efforts during the experiments; John F. McMahon for his indulgence during the many hours of consultation regarding the theoretical aspects of the problem; Richard E. Bland for his comments and suggestions regarding the utilization of the electronic equipment and analysis of data; Jeffrey O. Young for reviewing the thesis; and to the various members of the staff of the Department of Aeronautical Engineering and the Ordnance Research Laboratory for their patience and understanding.

Acknowledgment is also made to Dr. George F. Wislicenus, Professor and Head of the Department of Aeronautical Engineering and Director of the Garfield Thomas Water Tunnel, without whose guidance and direction this study would not have been possible.

# TABLE OF CONTENTS

LIST OF TABLES

## LIST OF FIGURES

## LIST OF SYMBOLS

| | |
|---|---|
| A,C | calibration constants |
| $A_n$ | Fourier coefficient for cosine series |
| a,b,c,d,e | constants relating laminar shape factors |
| $B_n$ | Fourier coefficient for sine series |
| b( ) | factor defined by equation 7 |
| $C_n$ | Fourier coefficient modulus |
| $C_1^*$ | constant defined by equation 3 |
| c | chord length |
| $c_f$ | coefficient of skin friction, turbulent flow |
| $c_{f\ell}$ | coefficient of skin friction, laminar flow |
| D | maximum body diameter |
| H | heat loss; shape factor |
| Im | imaginary part |
| J | advance ratio, proportional to $U/nR_p$ |
| K | time parameter; shape factor |
| L | shape factor defined by equation 4 |
| $\ell$ | body length |
| m | empirical constant |
| n | harmonic number; empirical constant; and measure of rotational speed |
| R | Reynolds number, $U\ell/\mathcal{D}$ ; radius of cross-section |
| Re | real part |
| $R_p$ | propeller radius |

| | |
|---|---|
| $R_{xx}$, $R_{yy}$ | coefficient of autocorrelation function |
| $R_{xy}$, $R_{yx}$ | coefficient of cross-correlation function for positive and negative time delay |
| $r$ | independent variable in the radial direction |
| $s$ | independent variable in the streamwise direction, parallel to body surface |
| $T$ | temperature; time |
| $U$ | Velocity of flow |
| $\bar{u}$ | steady mean value of randomly fluctuating velocity |
| $u'$ | root-mean-square value of randomly fluctuating velocity, $\sqrt{\overline{u^2}}$ |
| $x$ | axial coordinate, parallel to axis |
| $x_1, x_2, x_3$ | linear distance in the axial, radial, and circumferential directions |
| $y$ | vertical coordinate, normal to axis in radial direction |
| $y_F$ | final approximation for the body height, $y_0 + \delta^*$ |
| $\delta$ | actual thickness of boundary layer |
| $\delta^*$ | displacement thickness of boundary layer |
| $\delta^{**}$ | energy thickness of boundary layer |
| $\theta$ | independent variable in the circumferential direction |
| $\Lambda$ | Von Kármán-Pohlhausen laminar shape factor |
| $\mu$ | fluid viscosity |
| $\nu$ | kinematic viscosity, $\mu/\rho$ |
| $\xi$ | dummy variable of integration defined by equation 5; ratio of distance behind trailing edge of fin to fin chord length, $x/c$ |
| $\rho$ | fluid density |
| $\tau$ | time parameter |
| $\vartheta$ | momentum thickness of boundary layer |

$\bar{\phi}$      normalized power spectra

$\omega$      signal frequency

## Subscripts

crit     critical value

m      maximum value

n      successive approximation, n = 1,2,3,...; normalized value

$t$      variables referred to transition point

O      initial values

1      value of parameter at transition

$\infty$      free-stream condition

CHAPTER I

INTRODUCTION

A. Discussion of the General Field of Study

The flow behind a body of revolution with fins is of
practical importance in aeronautical and marine engineering.
Although the flow of real fluids over bodies of revolution and over
airfoils are well understood, the fluid motion over a body of
revolution equipped with fins cannot be predicted. In particular,
the effects of viscosity on the flow at the intersection of a fin
and a cylinder (or even a flat plate) still awaits a theoretical
explanation. It should be noted that this effect largely determines
the characteristics of the flow field in which, for instance, the
propulsor of an underwater vehicle operates. In such an application,
the designer requires an accurate knowledge of the inflow velocity
field to be able to establish the geometry of a propulsor capable of
developing the necessary thrust with a minimum level of unsteady
forces.

The solution to the above-mentioned problem can be obtained
from the solution to its separate parts:

a) In the first stage, the properties of the flow near the
trailing edge of a body of revolution with fins must be
established experimentally and compared with predicted
values based on existing theories. This information will

reveal the true nature of the flow and the limitations
of the theoretical approaches.

b) In the second stage, detailed experimental and
theoretical studies of special flow problems must be made
in order to explain the discrepancies observed. As an
example, the flow of a real fluid near the intersection
of a strut and a flat plate must be studied.

c) In the third stage, attempts must be made to control the
nature of the wake by practical or technically simple
means that can be used on existing vehicles.

B. Statement of the Problem

The primary objectives of this thesis are those stated in
paragraph a). In particular it was proposed to measure various
properties of the flow near the trailing edges of a slender body of
revolution with fins and to compare these measurements with
theoretically predicted values. In addition, the effects of a
propeller on these observations was assessed. More precisely, the
experimental work included the following measurements:

1. Circumferential and radial variations of mean velocity
and the associated harmonic content

2. Boundary-layer profiles

3. Circumferential and radial variations of the random
velocity fluctuations

4. Auto- and cross-correlation functions of the random
velocity fluctuations

5. Spectral and cross-power spectral densities of the random

velocity fluctuations

6. The detection and measurement of streamwise vortices
   originating at the fin-and-body intersections

7. A preliminary assessment of the effects of blowing at the
   fin-and-body intersections.

The theoretical work consisted of predictions of the
following quantities:

1. The velocity field for a streamlined body of revolution
   without fins in a real fluid

2. The velocity field behind the fins

3. The interaction between body and fins.

CHAPTER II

SUMMARY OF THE INVESTIGATION

The flow near the trailing edge of a slender body of
revolution with fins has been investigated by means of three
different instruments: Pitot tubes, hot-wire anemometers, and a
vorticity meter. The measurements were made in an axial plane at a
distance from the leading edge of the model equivalent to 95 per
cent of the body length, i.e., in a region normally occupied by the
propulsor of a typical underwater vehicle. The mean-velocity
profiles as well as some statistical properties of the random
velocity fluctuations were established. In addition, the streamwise
vortices formed at the body-and-fin intersections were investigated.
The experiments were performed in a wind tunnel at a Reynolds number
of $5.5 \times 10^6$, based on body length.

The steady (mean) flow observed near the body showed little
circumferential and radial variations when the body, supported by a
single airfoil strut, had no aft fins. Figure 1 shows a typical
part of the circumferential distribution of mean velocity, and
Fig. 2 shows corresponding harmonic components. When the four aft
fins were attached to the body, just upstream of the plane of the
measurements, the disturbances of the mean flow became more
pronounced, as shown in Figs. 1 and 2.

It was clear from a comparison of calculated and measured
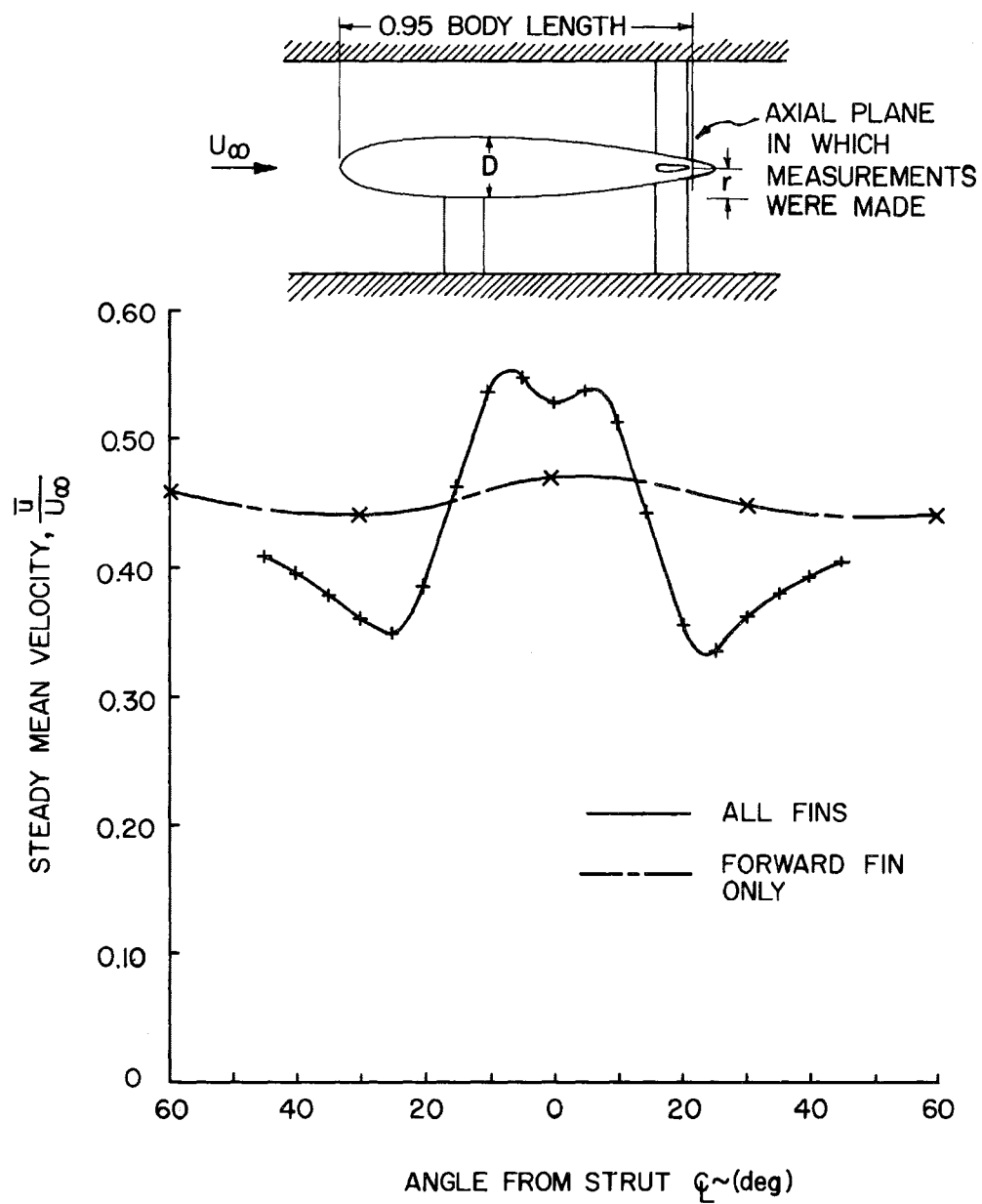
Fig. 1  Mean-Velocity Profile in an Axial Plane at 0.95L
with and without Fins
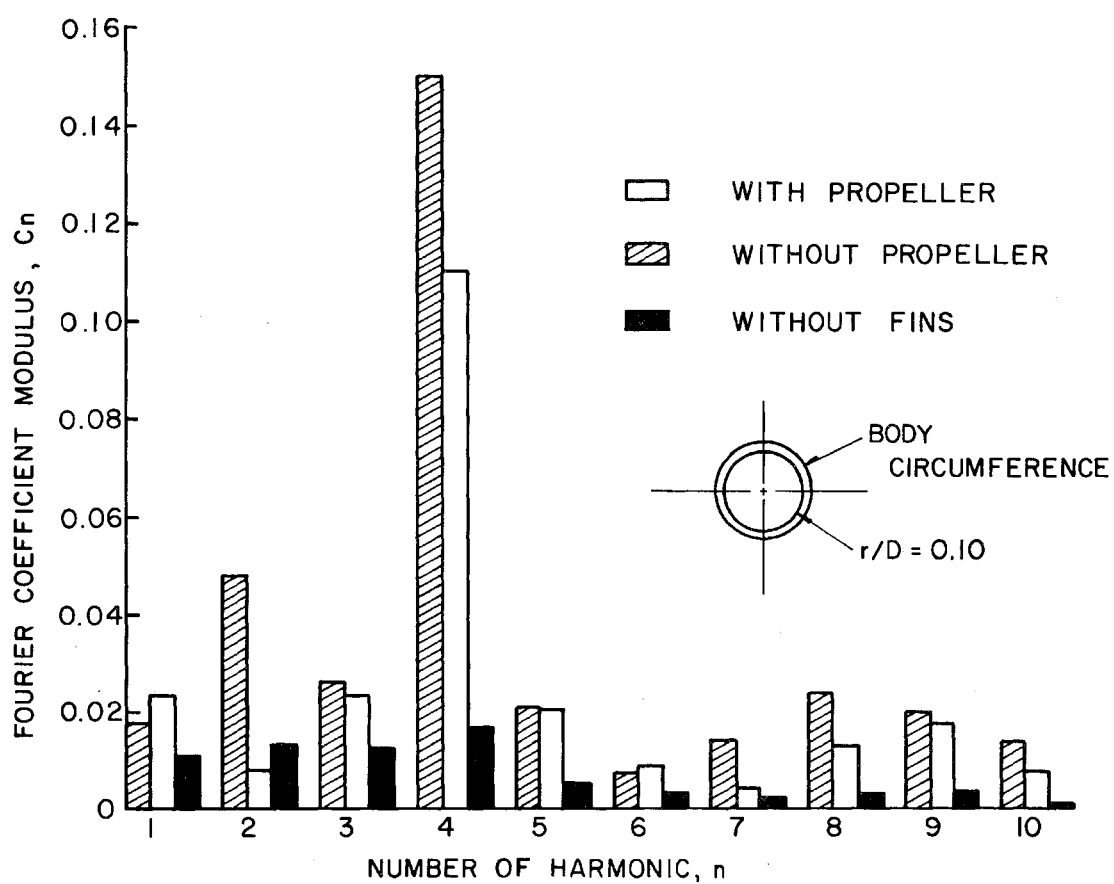
Fig. 2  Harmonic Content for Various Body Configurations
at r/D = 0.10

mean-velocity profiles (Fig. 3) that the aft fins affect the flow in two ways. At relatively large distances from the body axis, such as at $r/D = 0.35$, sharp depressions in the velocity profile are produced that agree with theoretical predictions. Near the body-and-fin intersection, however, vortices were formed as shown in Fig. 4. These vortices entrain fresh fluid into the immediate neighborhood of the fins and displace sluggish fluid from the boundary layer. As a result, large peaks and valleys were created in the velocity profiles (refer to curve for $r/D = 0.10$ in Fig. 3). Thus, Figs. 1 to 4 establish conclusively that the aft fins are the major cause of the radial and circumferential fluctuations of the mean velocity, which often produce strong oscillatory forces in the propulsors.

Before concluding this investigation an attempt was made to "de-spin" the corner vortices by blowing air through a pair of small holes located near the leading edge of one of the fins (Fig. 5). The size and location of the holes were arbitrarily chosen; therefore, the resulting conditions are not to be considered optimum. Nevertheless, the vorticity probe (Fig. 6) indicated a marked decrease in the streamwise rotation. The amplitudes of the mean velocity variations were also reduced, as shown in Fig. 7. This method, therefore, appears to hold promise for the eventual control of the velocity field in which propulsors operate, and further investigations--both theoretical and experimental--will be made.

Measurements made with two constant-temperature hot-wire
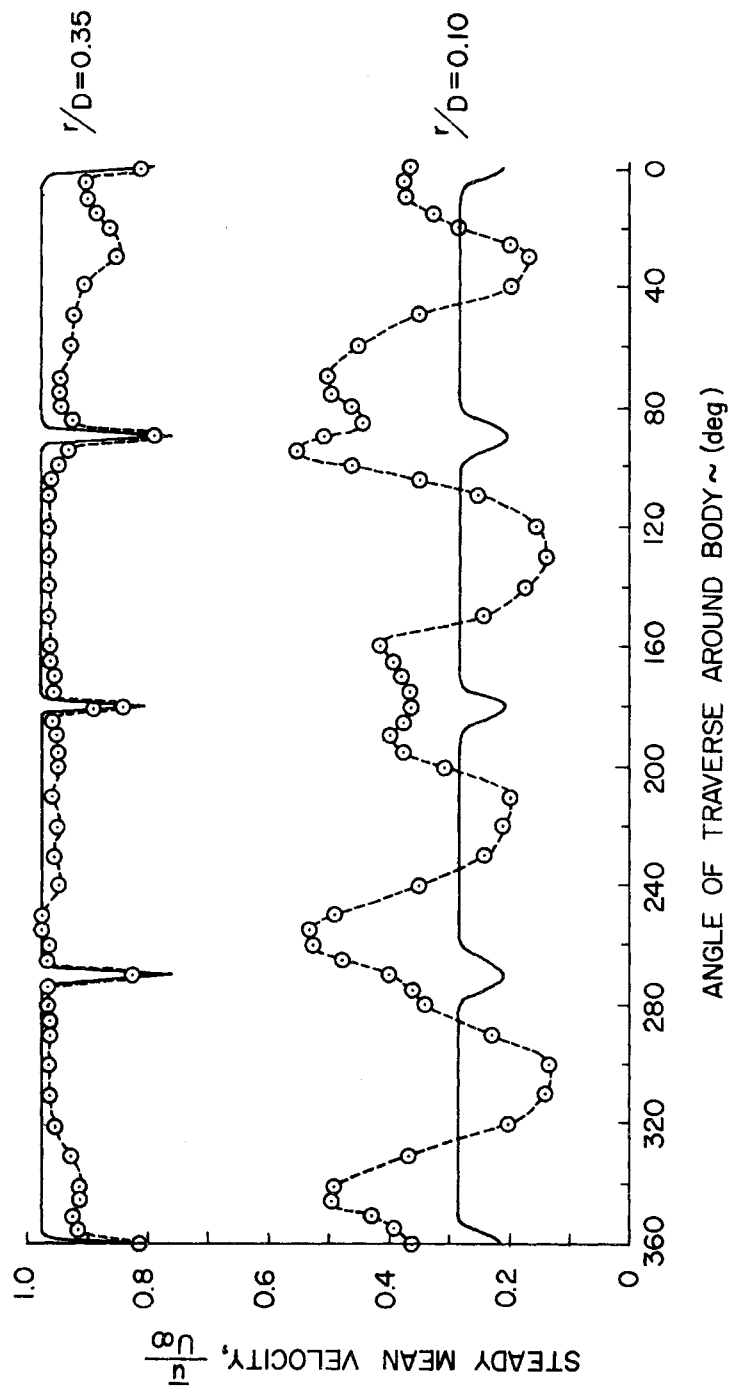
Fig. 3  Comparison of Mean-Velocity Profiles in an Axial
Plane at 0.95L
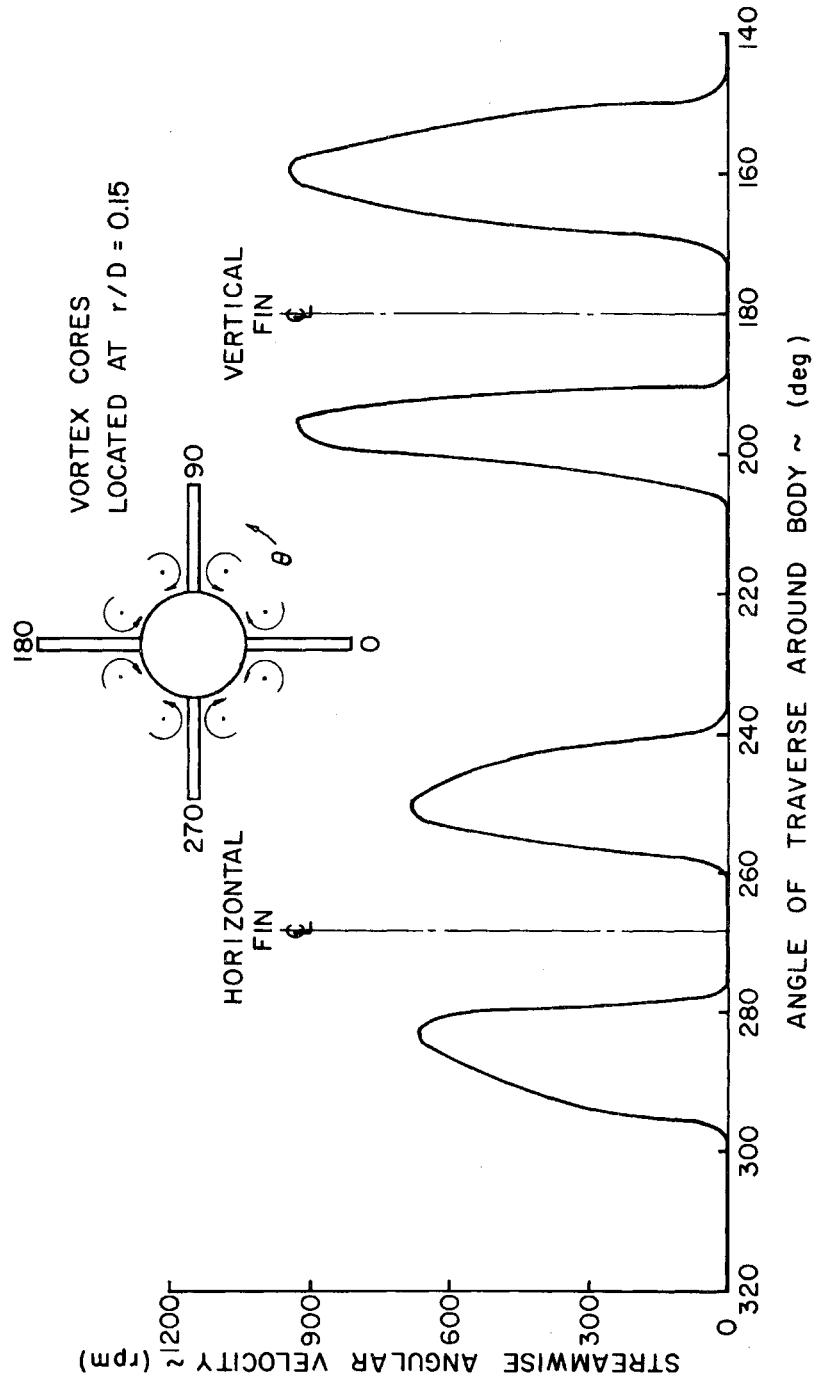
Fig. 4 Vortex Formation on Each Side of Fin-Body Intersection

AIR BLOWN NORMAL TO FREE-STREAM
AT ANGLE $\phi \cong 45$ deg BETWEEN STRUT
AND PLATE

FLOW

$\phi$
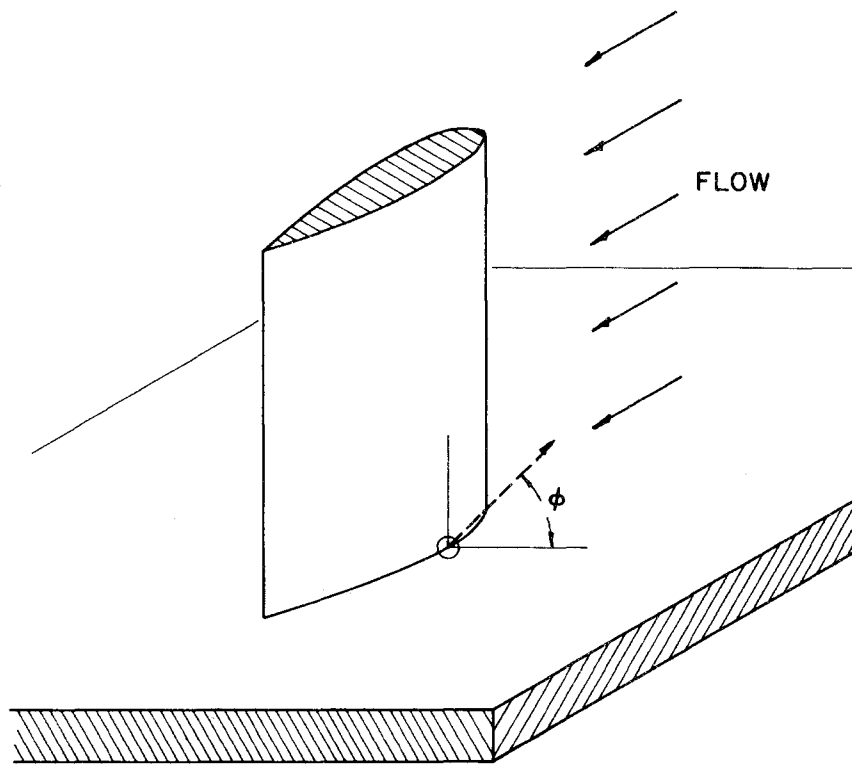
Fig. 5   Location of Holes for Blowing Air to Reduce Intensity
of Vortex

LIGHT BULB

HOLE JEWELS

CAP JEWEL

WINDOW

HOFFMAN PHOTO — VOLTAIC
DETECTOR TYPE EA7EI
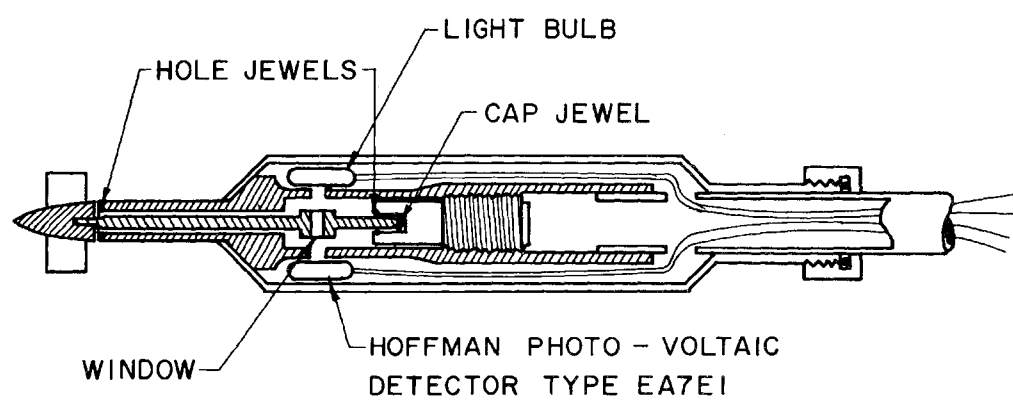
Fig. 6  Vorticity Probe
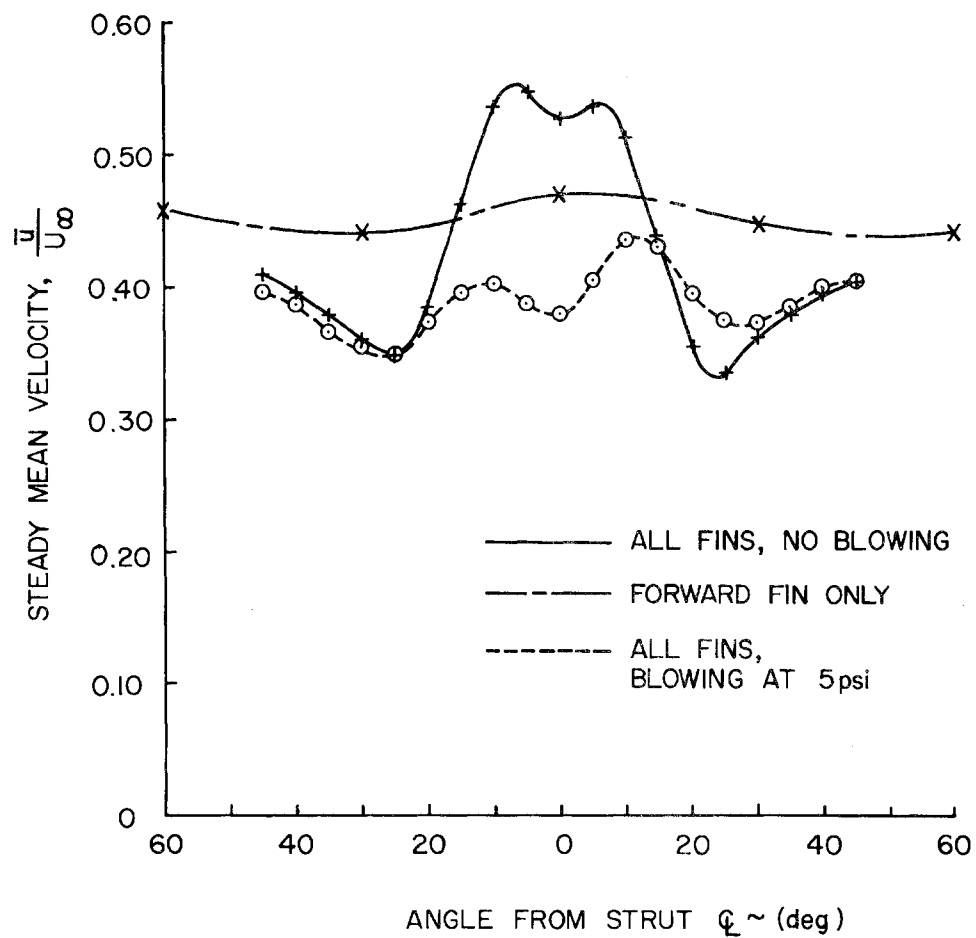
Fig. 7 Effects of Blowing on the Mean-Velocity Profile

anemometers established a number of statistical properties of the turbulent velocity fluctuations. Figure 8 shows a typical circumferential distribution of the root-mean-square values. During the tests, these values varied from a minimum of 3 per cent to a maximum of 10 per cent. The power spectra corresponding to various test conditions are shown in Fig. 9. The peak energy occurs at a nondimensional frequency where the characteristic length is the maximum diameter of the body. Finally, Figs. 10 to 13 show typical autocorrelation and cross-correlation functions, as well as cross-power spectral densities. These were calculated from magnetic tape recordings made during the tests with the aid of special analog-to-digital converters and high-speed digital computers. Most of the measurements were made both with propeller operating at its design advance ratio and with no propeller.

The effects of a propeller are most notable in Fig. 2. The propeller creates a favorable pressure gradient at a critical position on the body thereby reducing the mean velocity fluctuations as well as the intensity of the turbulent motions of the flow. Figure 2, which shows a reduction in the harmonic content, illustrates some of the beneficial influences produced by the propeller; however, it is difficult to distinguish the influences produced by the induction effects from those resulting from viscosity.
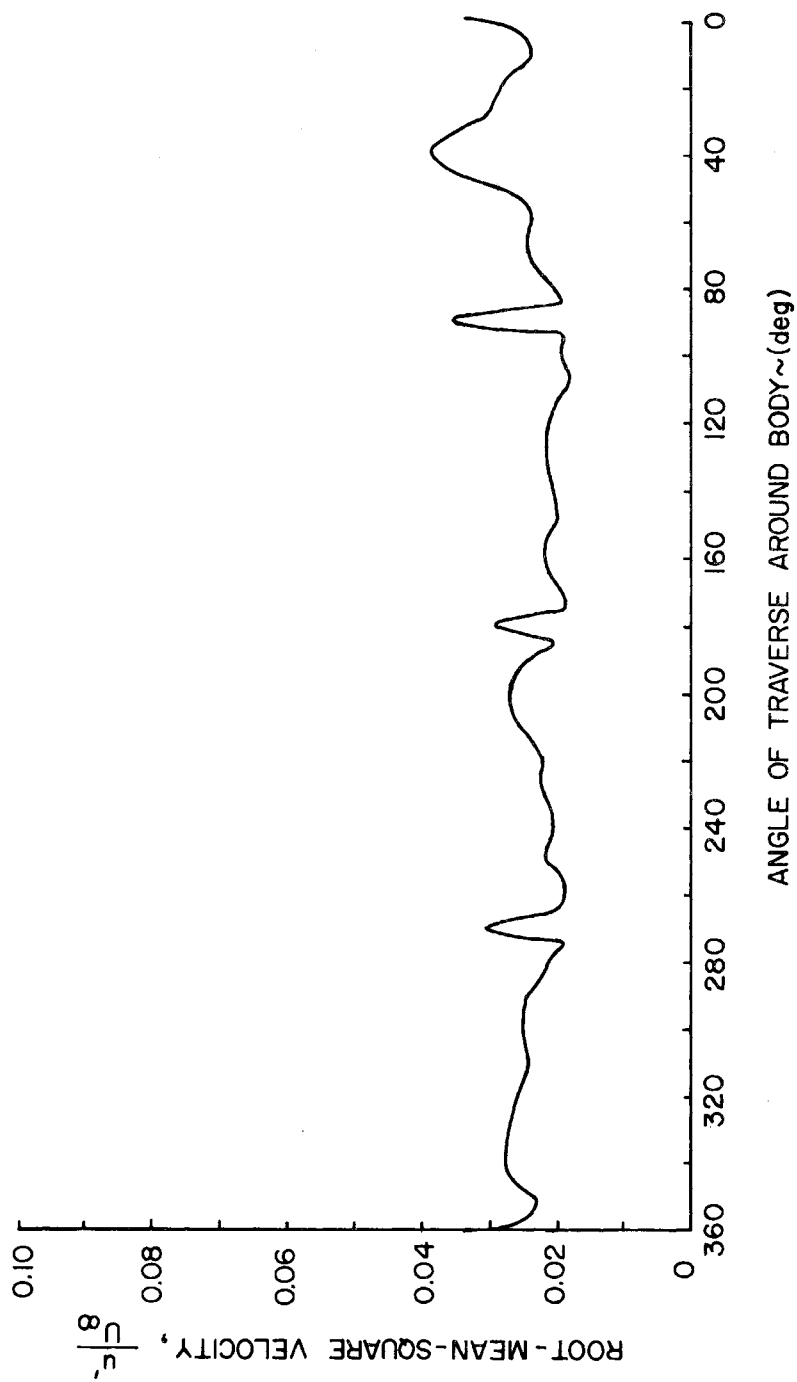
Fig. 8  Typical Root-Mean-Square Values of the Random-Velocity
Fluctuations for Body with Fins
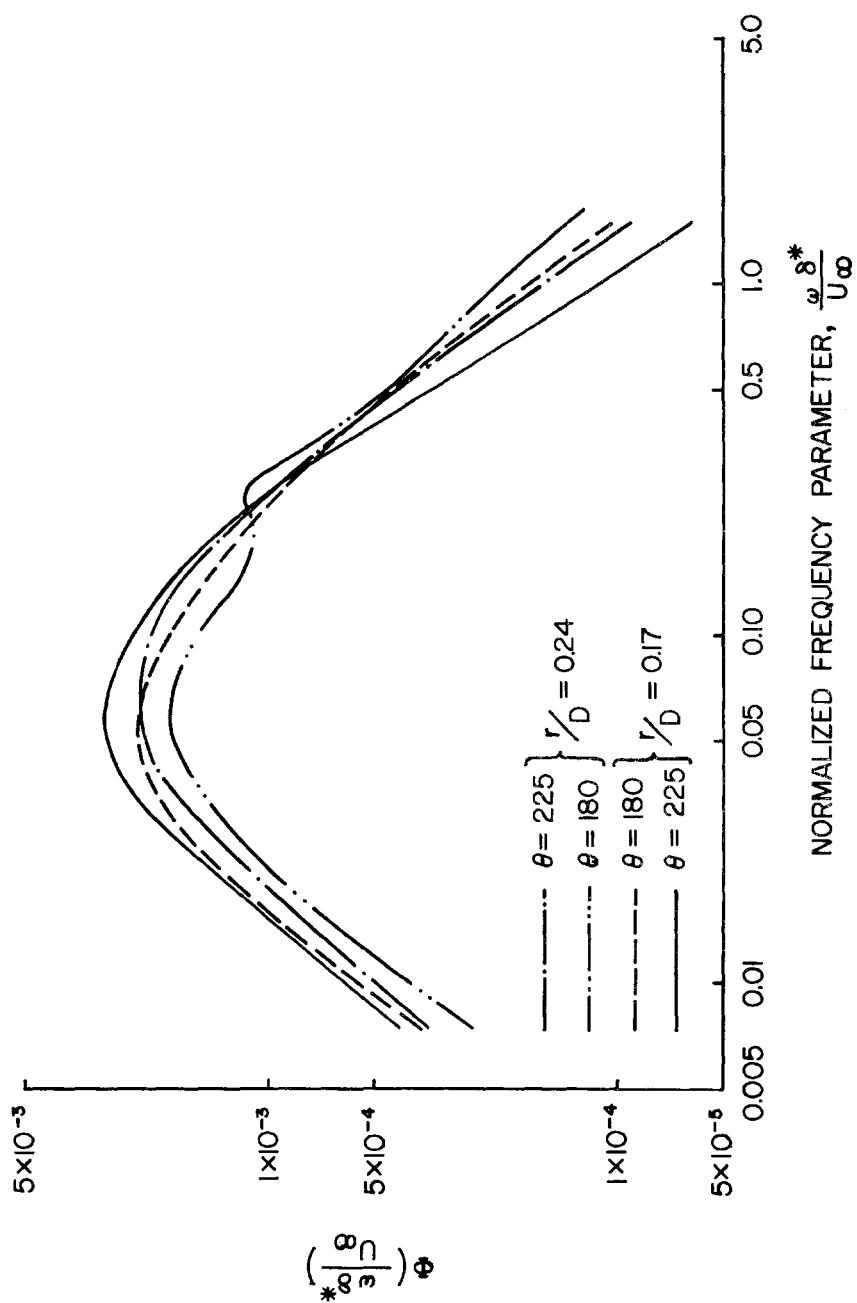
Fig. 9 Normalized Power Spectra
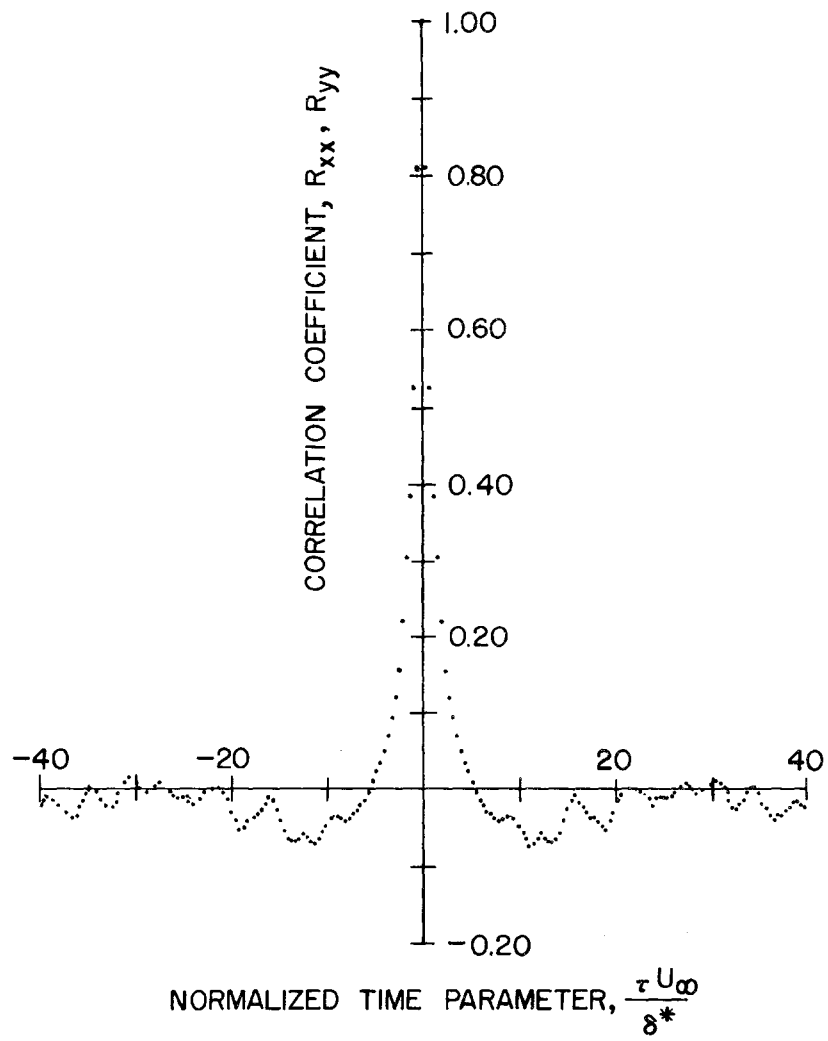
Fig. 10  Typical Normalized Autocorrelation Function
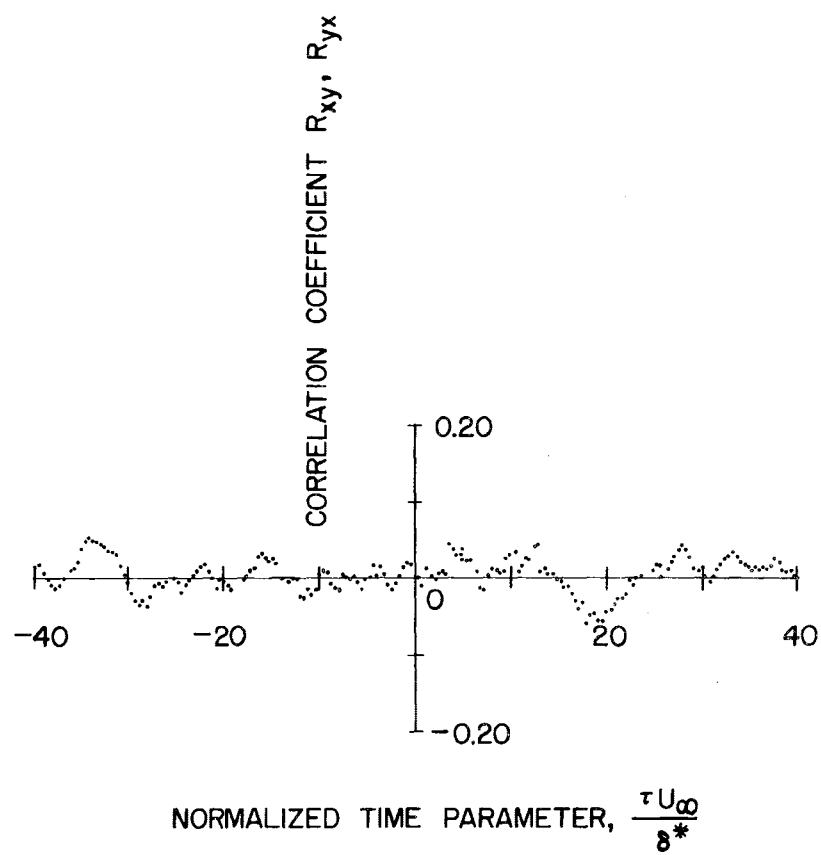
Fig. 11  Typical Normalized Cross-Correlation Function
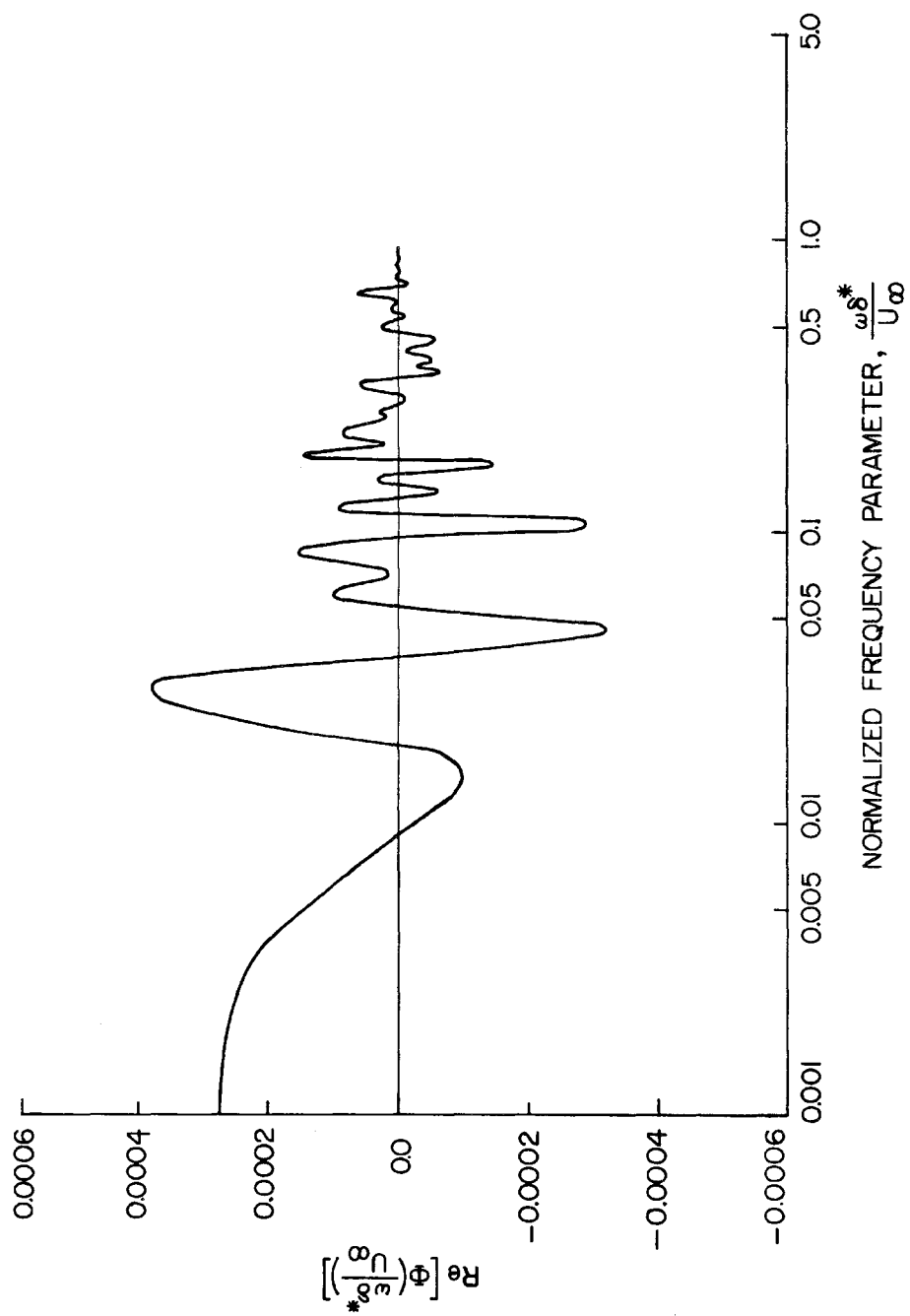
Fig. 12   Real Part of Cross-Power Spectral Density Associated
with Fig. 11
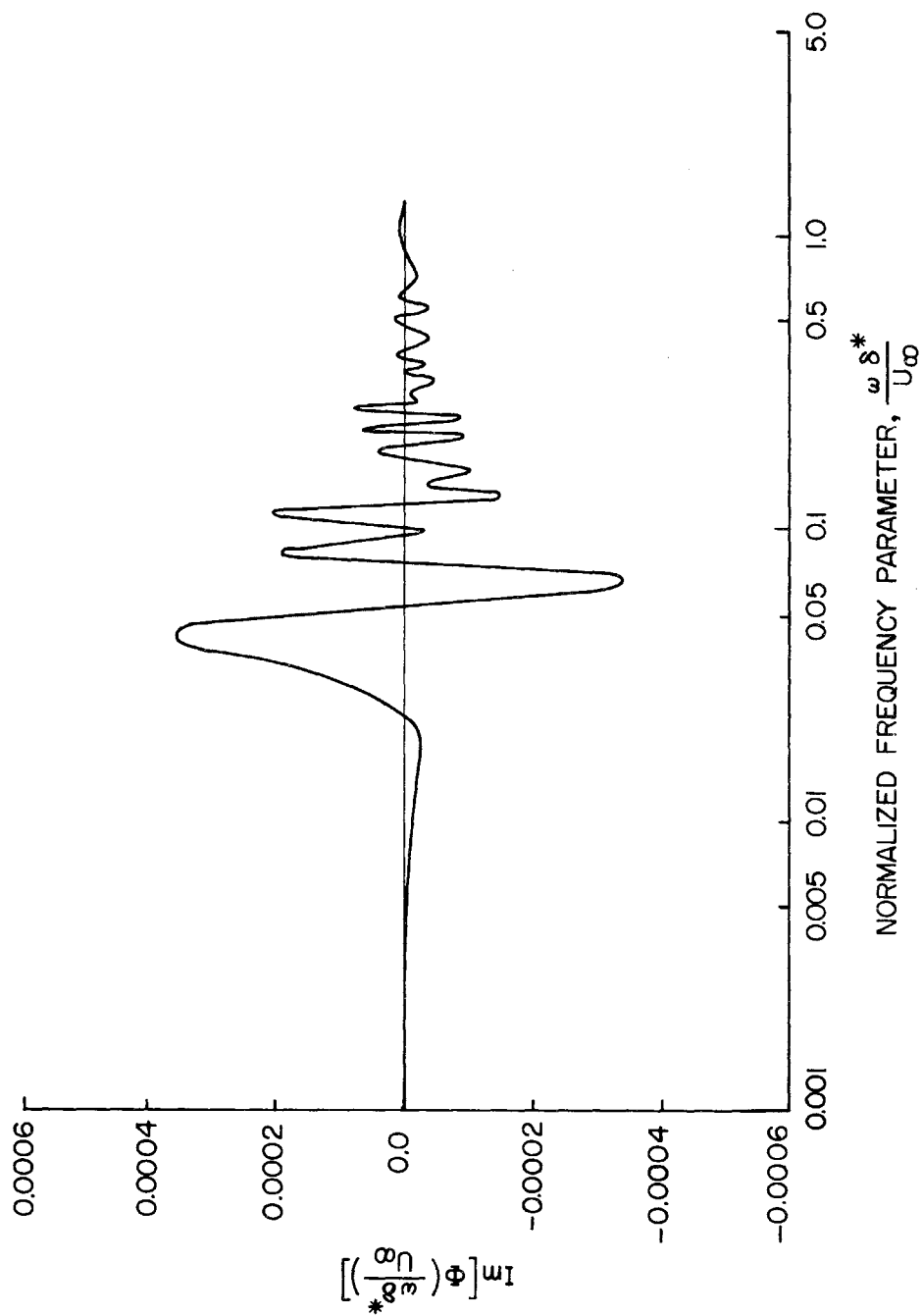
Fig. 13 Imaginary Part of Cross-Power Spectral Density
Associated with Fig. 11

CHAPTER III


EXPERIMENTAL STUDY


A. Discussion of Test Procedure and Aims

The experimental measurements were made in the wake of a streamlined body of revolution with fins. The body configuration approximated an 8:1 ellipsoid of revolution as shown in Fig. 14.

The main objective of the investigation was to obtain the flow characteristics at the region of inflow to the propeller. The measurements were made at various axial and radial locations as well as circumferential positions. Steady-state components were obtained from which mean-velocity distributions were obtained. Measurements were also made of the root-mean-square (rms) values of the randomly fluctuating velocity components. This resulted in the determination of the turbulence level of the flow field. Auto- and cross-correlation functions were calculated on the basis of measurements taken at different points in the flow field. Inherent in the reduction of the correlation data are several mathematical techniques: these consisted of performing Fourier Transforms to obtain normalized power spectra and Fourier Analyses to obtain harmonic content. The normalized power spectra were also obtained directly from the measurements by recording the signals from the measuring device on magnetic tape and playing them back through a wave analyzer and integrator.
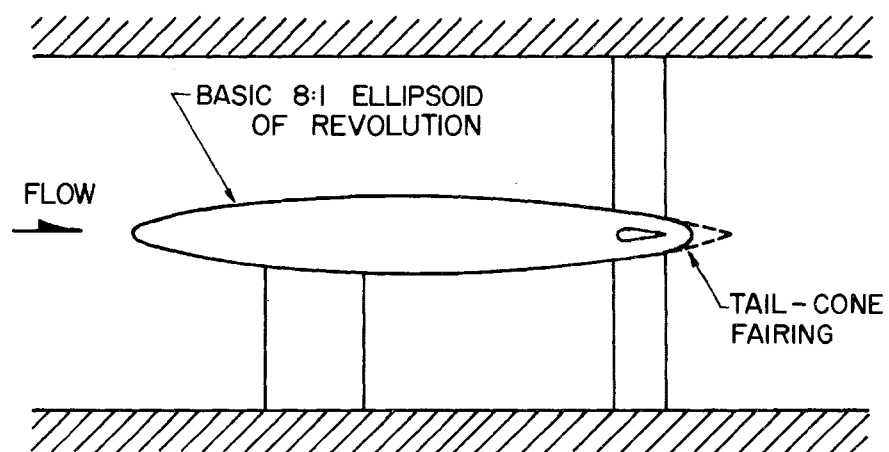
Fig. 14  Body Configuration Used in the Experiments

The tests were conducted in the 48-inch diameter, 16-foot long octagonal test section of the wind tunnel at the Garfield Thomas Water Tunnel, Ordnance Research Laboratory, at The Pennsylvania State University. For this investigation, the air speed in the tunnel was maintained at approximately 100 fps. A detailed description of this closed-circuit tunnel will be found in Reference 1.

To maintain a complete but efficient test program, the position variables were kept at a minimum. The measurements were made at a constant axial location, between the control surface trailing edge and the propeller leading edge. The radial positions were varied outward from the body while circumferential traverses were made completely around the body.

To present the results in as general a manner as possible, certain constants were chosen by which the variable quantities were nondimensionalized. Thus, linear dimensions were non-dimensionalized with respect to body length, body diameter, or displacement thickness. Velocity measurements were normalized with respect to the free-stream value or some other characteristic parameter, such as the mean velocity in the boundary layer.

The primary independent variables were the radial and circumferential positions around the body. The radial positions chosen were at values for $r/D$ of 0.10, 0.17, 0.24, and 0.35; where r is the normal distance from the body axis to the point of interest and D is the maximum body diameter. The circumferential traverses were performed completely around the body for each value

of r/D.

The measurements were performed without the propeller and then repeated after the propeller was added; thus, any difference in the measurements was due solely to the presence of the propeller.

Figure 15 shows the radial positions of the measurements and the coordinate system chosen to describe the circumferential traverses. All measurements were performed with a constant-temperature hot-wire anemometer and checked against a pitot-static probe that was used as a reference. The hot-wire-anemometer equipment and its use are described in a later section. The repeatability of the data was within 3 to 5 per cent from day to day and from week to week.

The model is approximated by an 8:1 ellipsoid of revolution with fins (Fig. 14). The model was supported in the tunnel by the large fin at the forward part of the body rather than sting-mounted to eliminate any vibrations that would occur as a result of cantilevered mounting.

Referring to Fig. 15, the lower strut was designated zero angle; positive angles were those measured counterclockwise when viewed upstream. The other fins were located on the aft part of the body and spaced equidistantly. The profile of all struts, fore and aft, was an NACA-0015 airfoil section.

To eliminate any effects produced by tunnel-wall interference, a "liner" was used in the test section. The resulting inner contour in the test section was determined by a potential flow solution for the body and approximated a stream surface. This procedure is

RADIAL PROBE POSITIONS

| | | |
|---|---|---|
| 1 | r/D | =0.35 |
| 2 | " | =0.24 |
| 3 | " | =0.17 |
| 4 | " | =0.10 |
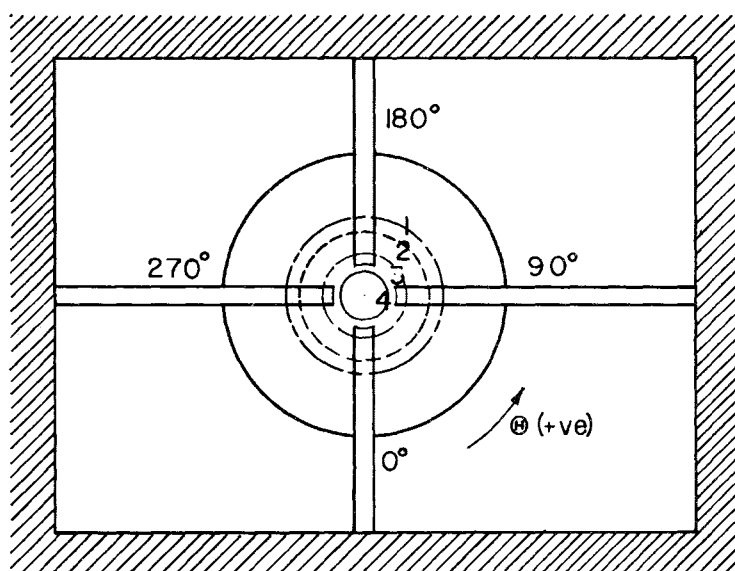


Fig. 15  Radial- and Circumferential-Probe Locations and
Coordinate System

necessary when the ratio of body to test-section diameter becomes greater than 1:6. (In this case the ratio is about 1:3). As a result of this modification, the flow field in the tunnel was almost axisymmetric.

Two hot-wire probes were used for the velocity measurements. One probe was placed at a constant axial position along the body and at a constant angular position between two control surfaces. This probe was moved only in a radial direction. The second probe was at the same axial station, but its position was varied in both the radial and circumferential directions. This probe, referred to as the "movable" probe, was mounted on a traversing mechanism attached to the external surface of the tunnel wall.

The moveable probe was mounted on a strut that, in turn, was mounted on a platform. The platform was mounted on bars that passed completely through the tunnel such that it could slide along the bars to various positions behind the body. The strut could be rotated by an external control. Thus, the second probe could be fixed at a radial position and rotated to make the required circumferential measurements.

The signals from the probes were recorded simultaneously on magnetic tape. These signals were later played back and re-recorded for a computer that introduced the proper time lags so that correlation functions could be obtained.

The testing procedure was the same both with and without the propeller installed on the model. During tests with the propeller in place, all measurements were made at its design advance ratio.

For these tests the moveable probe was modified so that measurements could be made at the inflow region. The probe holder was extended so that the probe was in a vertical position in front of the propeller instead of horizontal. This new orientation of the probe did not affect the ability of the wire to sense axial velocity, because it will respond only to fluctuations normal to its own axis. The position of the extension device was such that it did not interfere with the operation of the propeller or disturb the flow field.

B. Test Equipment

The primary piece of test equipment was a constant-temperature hot-wire anemometer designed by Kovasznay and constructed at the Johns Hopkins University.(2,3)

Briefly, the hot-wire anemometer is used to measure random velocity fluctuations by producing a voltage that is proportional to velocity. The wire (usually 0.00015-in.-dia tungsten) is placed in a resistance bridge and bridge balance is maintained by closing the feedback loop with a d-c amplifier. The air flowing over the wire cools it, thus changing its resistance and unbalancing the bridge. The unbalance produced by the air flow is recorded as a fluctuating voltage about some predetermined mean.

The physical law that describes the phenomenon of heat loss from the wire is assumed to follow King's law:

$$H = \Delta T \left( A\sqrt{U} + C \right)$$

where H the heat loss of the wire, $\Delta T$ the difference between the temperature of the unheated wire and the actual operating

temperature of the wire, U the air-flow velocity, and A and C are constants that are determined by calibration. In the equilibrium stage of operation, this heat loss is equal to the electrical power input.

The appropriate nonlinear circuit to invert King's law consists of two squaring circuits and an adjustable bias. The circuit device, called a "linearizer," converts the output of the hot-wire anemometer into a voltage that is proportional to velocity. The amplifier and linearizer are shown in Fig. 16.

Figure 17 is a block diagram of the amplifier and linearizer with the peripheral equipment used for recording data. Table I lists this equipment.

Appendix I outlines a method for checking the response of the hot-wire anemometer and comparing this response with that of a pitot-static probe.

C. Method for Obtaining and Presenting Test Results

The testing procedure is described here in detail to show the evolution of the work.

    1. Body with fins and without propeller

        a. Mean-velocity distribution

        b. Root-mean-square velocity distribution

        c. Boundary-layer profiles

    2. Body with fins and propeller

        a. Mean-velocity distribution

        b. Root-mean-square velocity distribution

        c. Boundary-layer profiles
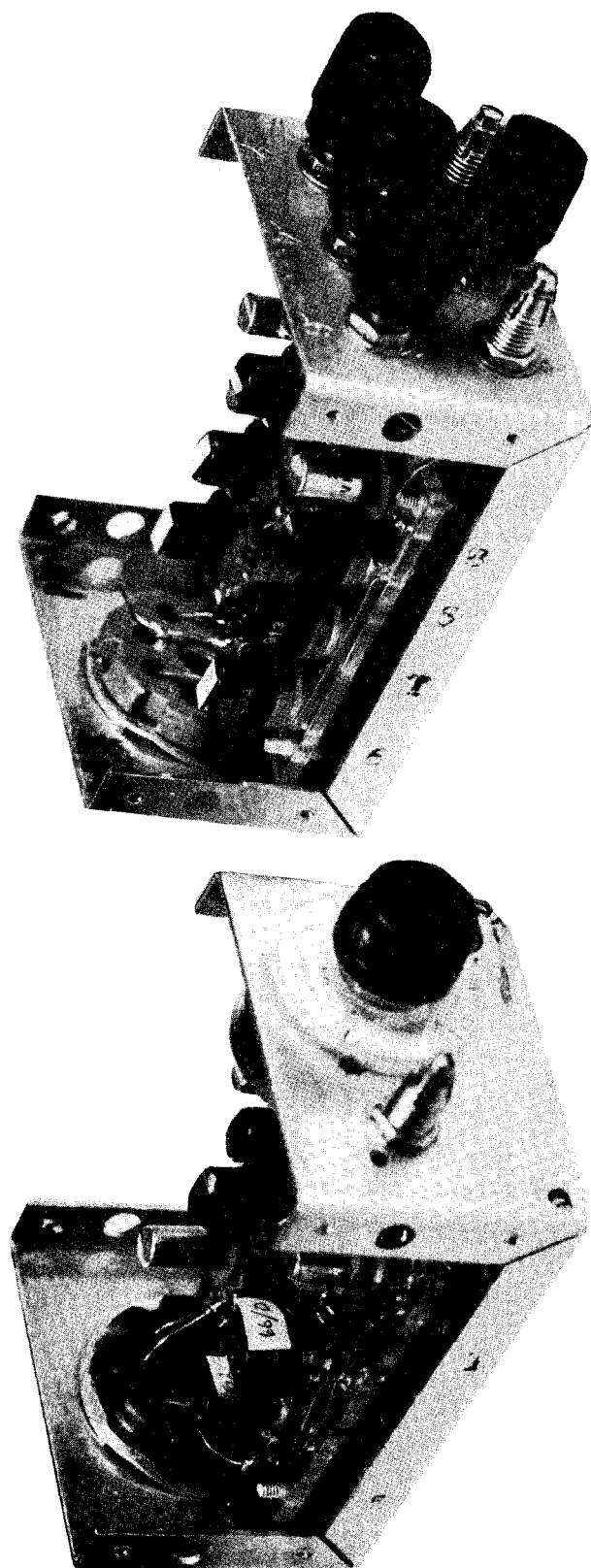
AMPLIFIER

LINEARIZER

Fig. 16 Hot-Wire Amplifier and Linearizer
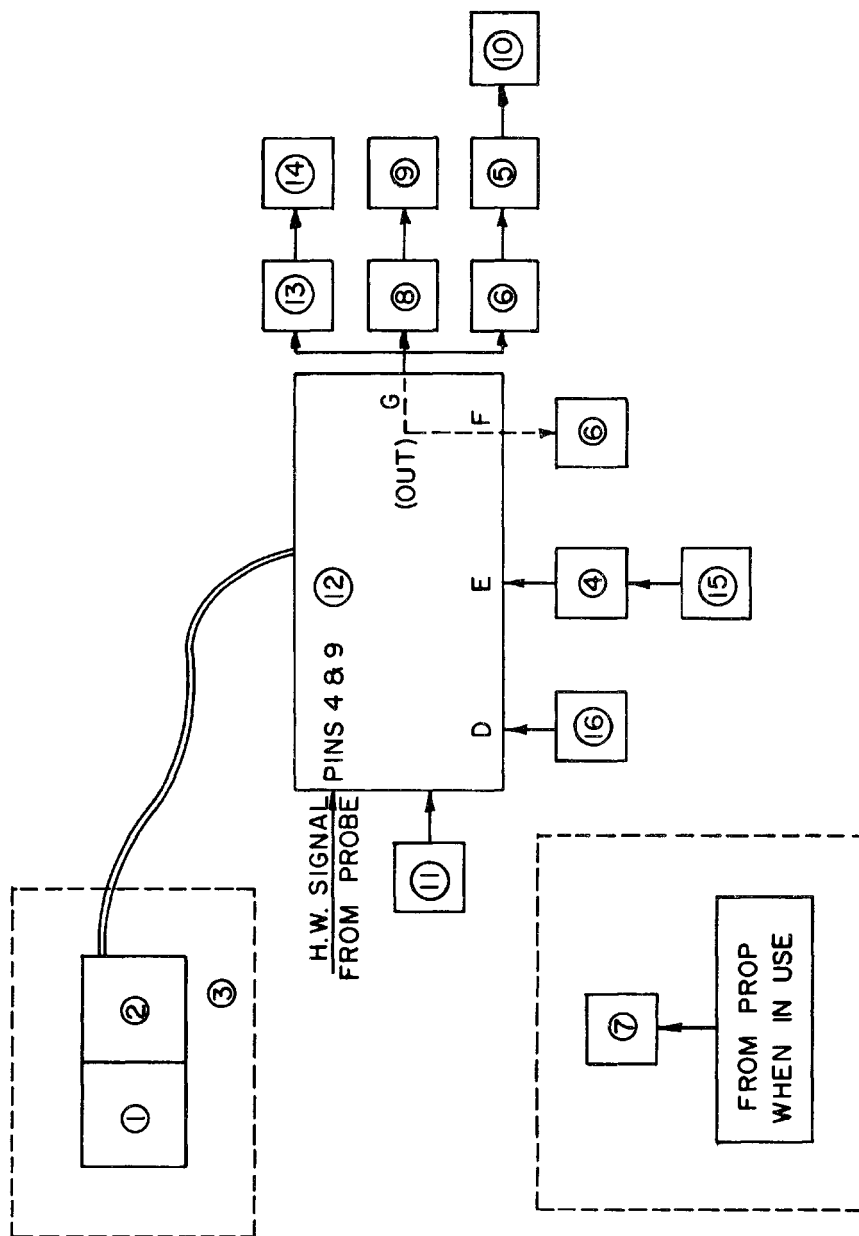
Fig. 17  Block Diagram of Peripheral Equipment Used with the
Hot-Wire Anemometer

TABLE I

PERIPHERAL EQUIPMENT FOR HOT-WIRE ANEMOMETER

1.  Model M-5 Hot-Wire Amplifier

2.  Model L-3 Linearizer

3.  Test-Lab Corp, Cat. No. 3550, "Ambli-lo" Cabinet for
    Constant Temperature

4.  Ballantine Laboratories, RMS A-C Voltmeter

5.  Hewlett-Packard, 3440A Digital Voltmeter

6.  Hewlett-Packard, Dual Trace Scope

7.  Hewlett-Packard, Electronic Counter

8.  Weston, Model 220 Decade Amplifier

9.  Consolidated Electrodynamics Corporation, 7-Channel
    magnetic-tape recorder, Type GR 2800

10. Ballantine Laboratories, True RMS Meter

11. Power Supply, 0 to 6V D-C

12. Front panel for Hot-Wire Anemometer Output

13. Panoramic Sonic Analyzer

14. Brüel and Kjaer, 1/3 Octave Analyzer

15. Audio Oscillator

16. -2.5V D-C Power Supply (two 1.5V dry cells with a
    10,000-ohm potentiometer)

d. Boundary-layer profiles at $x/L = 0.99$

Unless otherwise noted, the velocity distributions were made at radial positions of $r/D$ equal to $0.10$, $0.17$, $0.24$, and $0.35$; all circumferential measurements were made for $\Theta$ between 0 and 360 deg; all axial positions remained constant at $x/L = 0.95$; and the boundary-layer profiles were made at $x/L = 0.95$ and $\Theta = 45$ deg.

The output signal from the hot-wire anemometer was fed into a d-c voltmeter, which recorded the mean value of the fluctuations. This voltage was compared with the voltage found for the free-stream velocity from calibration test runs. Thus, at the particular point in question, the ratio of U local to $U_\infty$ was obtained.

The fluctuating component was recorded on a true rms voltmeter. When this voltage was compared with the free-stream value, the turbulence level, or rms value, was obtained. Figures 18 and 19 are typical of the graphical presentation made of these results. The complete graphical description of the flow field for each test condition is given in Appendix III.

The boundary-layer profiles were obtained in the same manner as the wake profiles, except that the angle of traverse was kept constant and the radial position was varied. A typical profile of mean velocity vs distance from the body is shown in Fig. 20.

The boundary-layer characteristics at some axial station are based on the displacement and momentum thicknesses rather than just the boundary-layer thickness.(4) This allows for more meaningful results to be concluded from a particular investigation.

The displacement thickness, defined as the decrease in volume
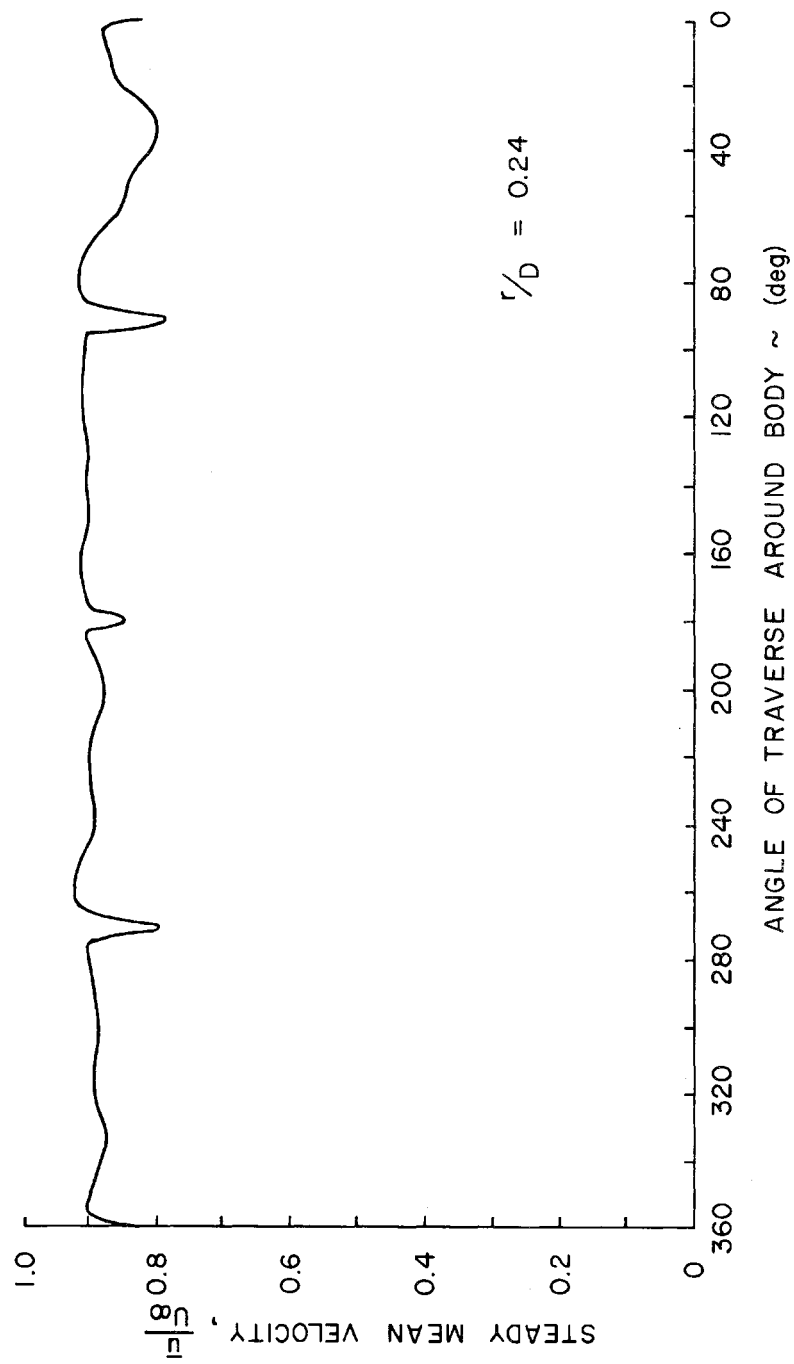
Fig. 18 Typical Steady Mean-Velocity Distribution
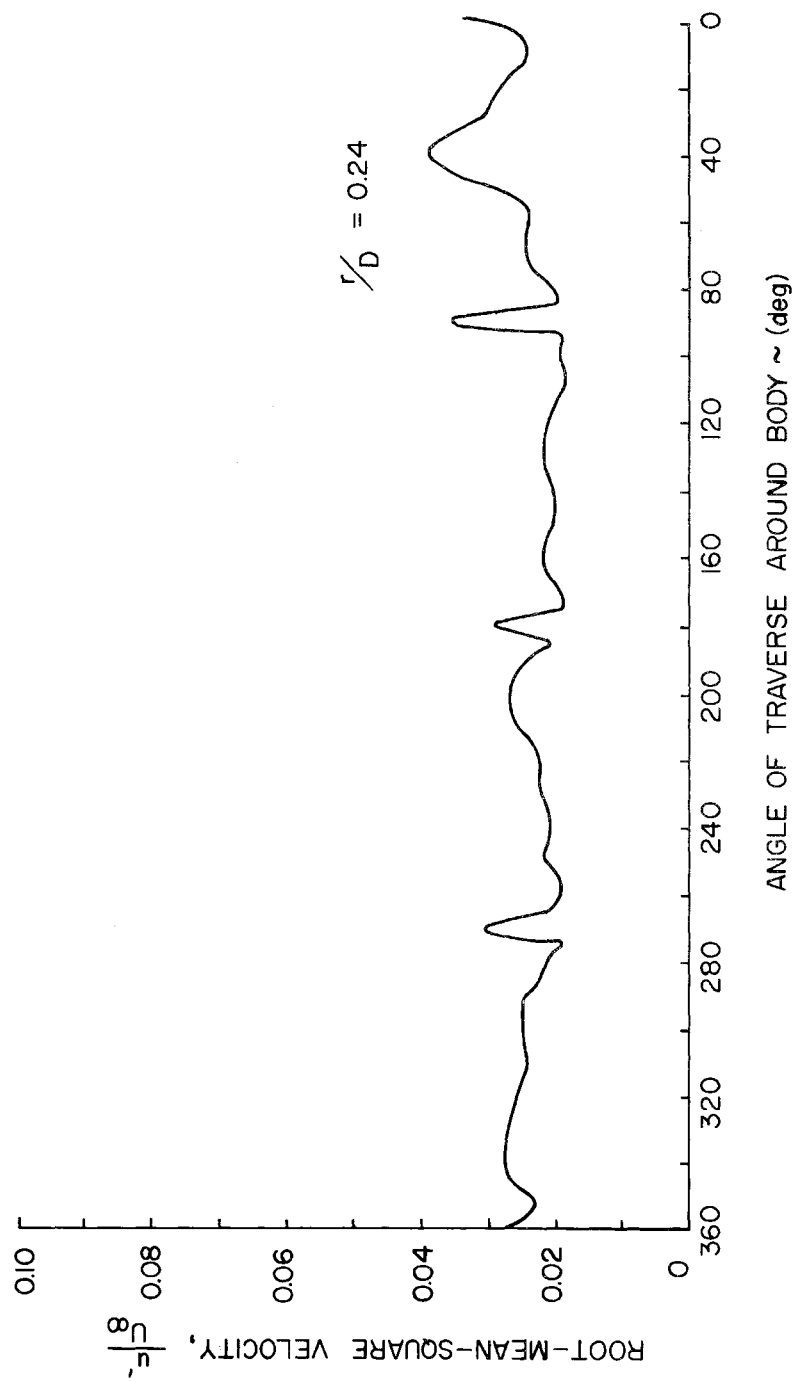
Fig. 19 Typical Root-Mean-Square Velocity Distribution
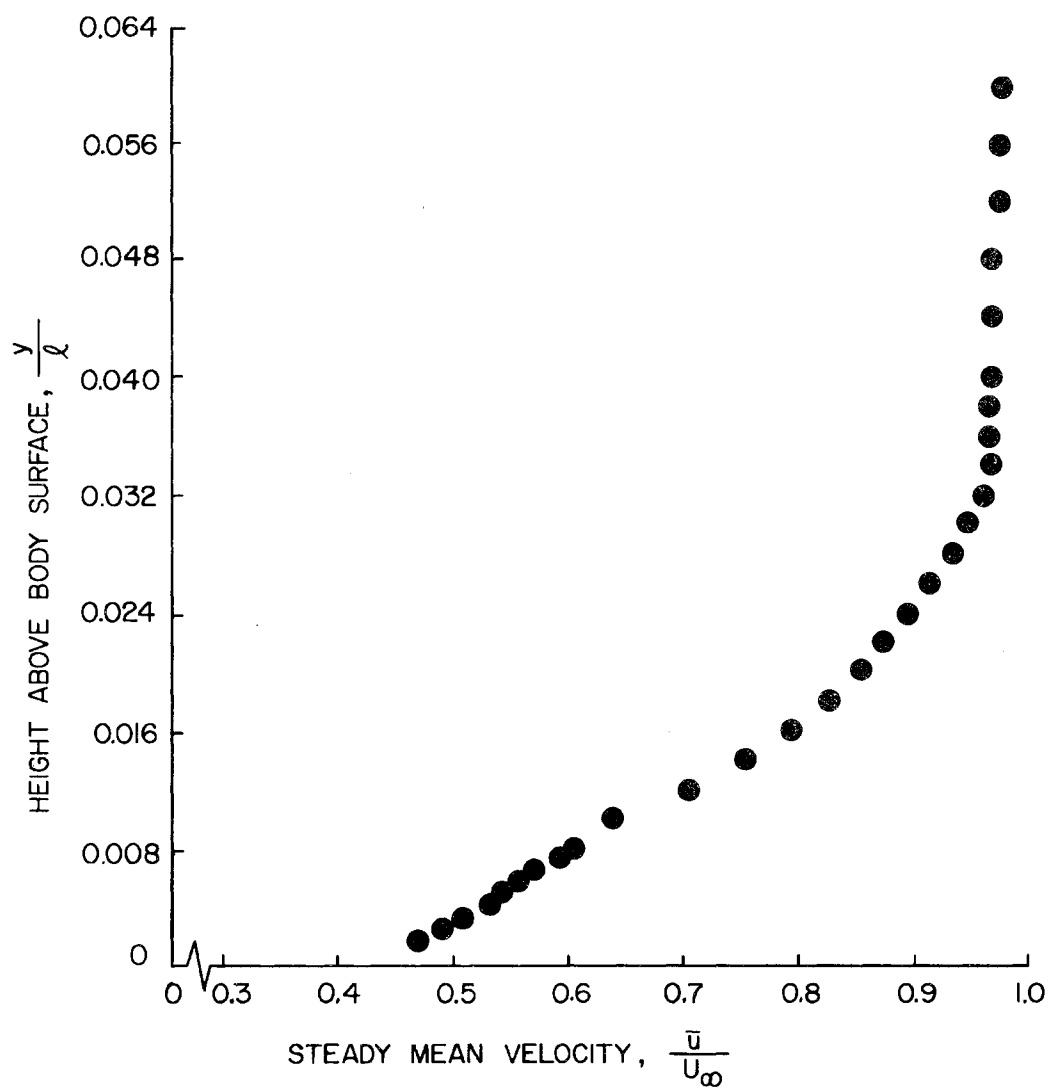
Fig. 20  Typical Boundary-Layer Profile Measured with a Hot-Wire
Anemometer

flow resulting from the influence of friction, is given by

$$\delta^* = \int_{y=0}^{y=\delta} \left(1 - \frac{\bar{u}}{U_\infty}\right) dy \qquad ,$$

where the boundary-layer profile is integrated from the body surface to the free-stream.

The momentum thickness, which represents the loss of momentum in the boundary layer, is given as

$$\vartheta = \int_{y=0}^{y=\delta} \frac{\bar{u}}{U_\infty} \left(1 - \frac{\bar{u}}{U_\infty}\right) dy \qquad ,$$

These quantities define the shape factor $H = \delta^*/\vartheta$ , which describes the boundary-layer profile at any point along the body. A more detailed discussion regarding the actual calculations, as well as the values of $\delta^*$ and $\vartheta$, can be found in Appendix II.

## D. Data-Reduction Techniques

An oscilloscope and a Panoramic Sonic Analyzer were employed as visual aids for detecting turbulence. The analyzer displays the energy level versus frequency at a particular instant. This analyzer does not give a true power spectrum; it simply indicates regions of high energy concentrations that should be more fully investigated.

The normalized power spectrum was obtained by passing the hot-wire signal through a wave analyzer and integrating it for approximately 30 sec. Figure 21 is a comparison of this power spectrum with that obtained by performing a Fourier transform of the
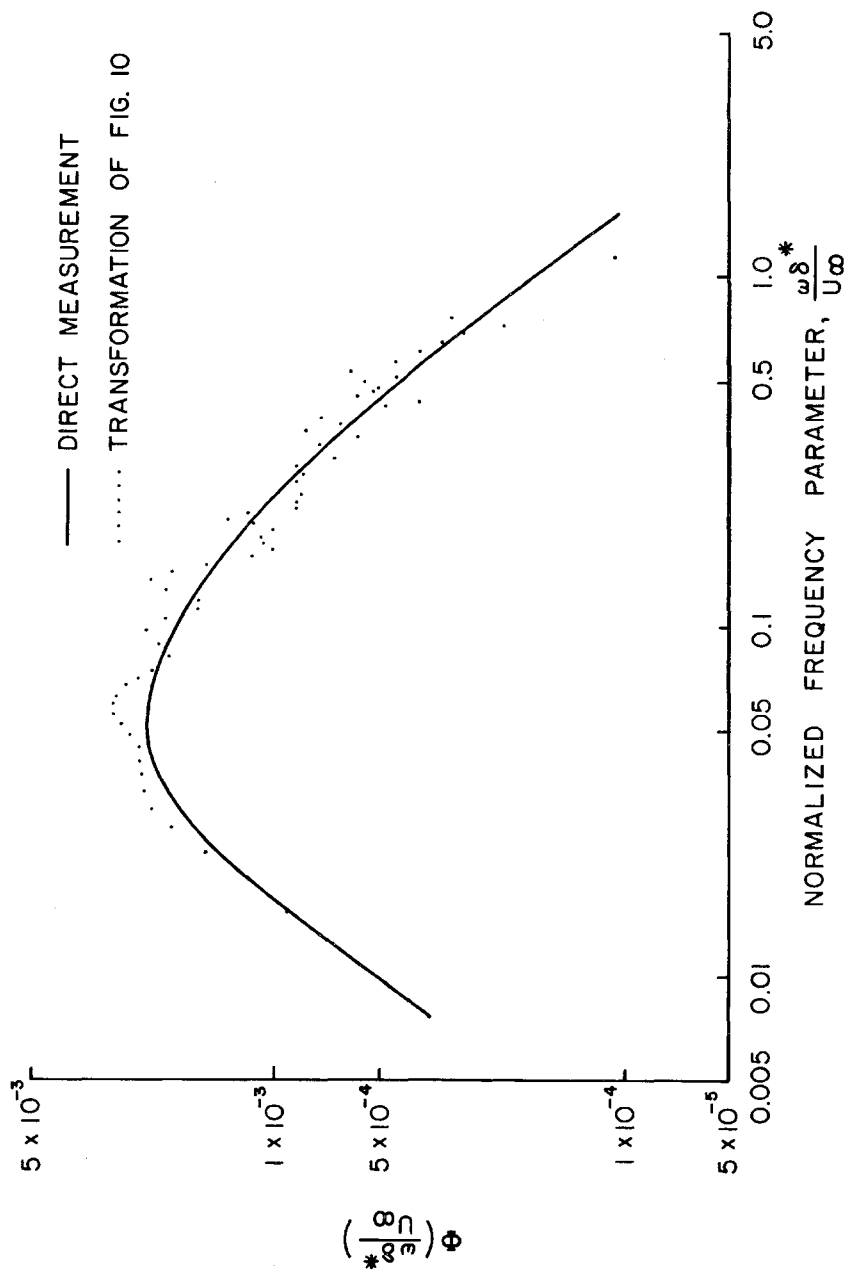
Fig. 21 Comparison of Normalized Power Spectra

autocorrelation function shown in Fig. 10. This last method represents a mathematical technique for obtaining the normalized power spectra and shows the results of this method to be in agreement with those obtained by direct measurement.

This normalized curve is shown (dotted) in Fig. 21. Note that the abscissa in this figure has been normalized with respect to the displacement thickness and free-stream velocity. This has been done to make the results compatible with the work of other investigators.(5),(6)

The cross-power spectral density was obtained in a manner analogous to the foregoing except that the cross-correlation rather than the autocorrelation function is used. Figure 11 shows a typical cross-correlation function related to the autocorrelation function of Fig. 10.

Figures 12 and 13 are the cross-power spectral densities of the real and imaginary parts, respectively, of Fig. 11. From each of the figures showing the power spectrum, it is seen that, as the frequency $\omega \delta^*/U_\infty$ increases, the available energy approaches zero. This is expected since only a finite amount of energy is available in the flow field.

The cross-power spectral densities associated with specific points in the flow-field are shown in Appendix III together with the corresponding cross-correlation functions.

Of vital interest to the propeller designer is the harmonic content of the flow field. As an illustration of the harmonic content, consider Fig. 22; this shows a large amplitude at the
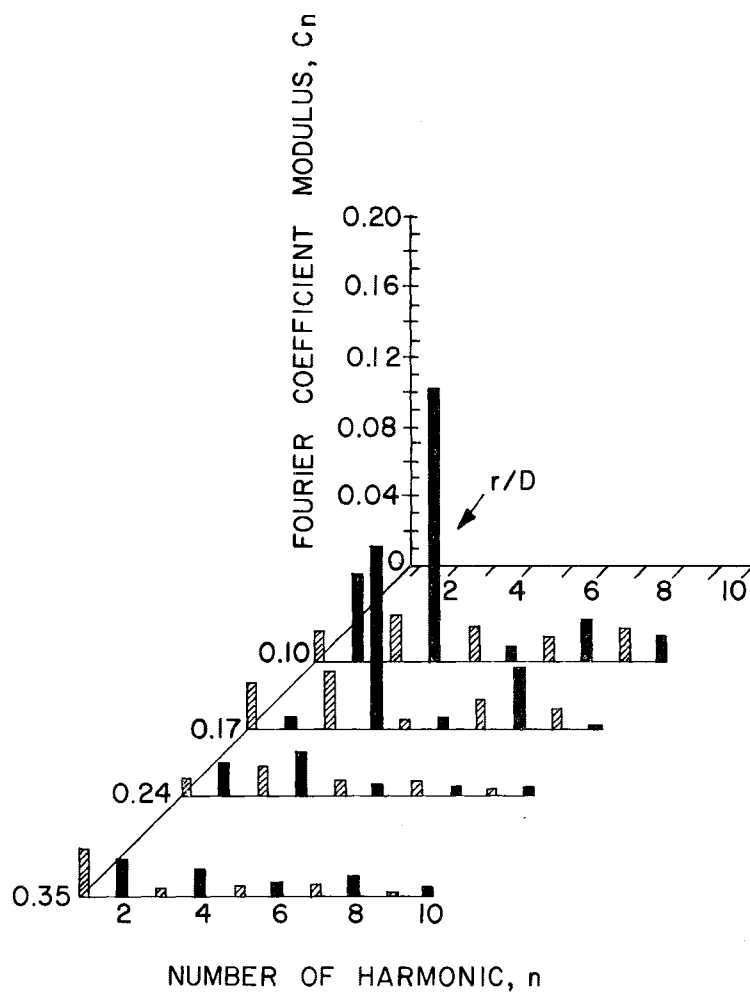
Fig. 22   Harmonic Content of Flow Field for Body with Fins
and without Propeller

fourth harmonic, which is produced by the fins.

Figure 23 is a similar analysis for the body with only the forward supporting strut. As expected, there is no real predominant harmonic, even close to the body. The differences between the two figures is due solely to the effects of the afterbody struts.

These graphs of harmonic content were obtained by performing a Fourier Analysis on the wake velocity profiles for various values of $r/D$. (These profiles are shown completely in Appendix III.) A typical velocity profile is shown in Fig. 18.

Numerically integrating such functions yielded the coefficients $A_n$ and $B_n$. The quality of the curve fit is determined by how well it approximates the original function. This, in turn, determines the number of coefficients necessary. In obtaining Figs. 2, 22, and 23 ten coefficients were chosen with

$$C_n = \text{mod}\left(A_n, B_n\right) = \sqrt{A_n^2 + B_n^2}$$

As mentioned earlier, two hot-wire probes were used so that two signals could be recorded simultaneously. This was done to obtain data for the auto- and cross-correlation functions associated with the flow field.

The stationary probe was used as the reference and was located between two fins at an angular position $\theta = 45$ deg. The axial and radial position of both probes remained constant for this test at $0.95L$ and $0.17D$ respectively. With the stationary probe in its position, the movable probe was traversed around the body. At selected locations of $\Delta\theta$, the angle between the two probes,
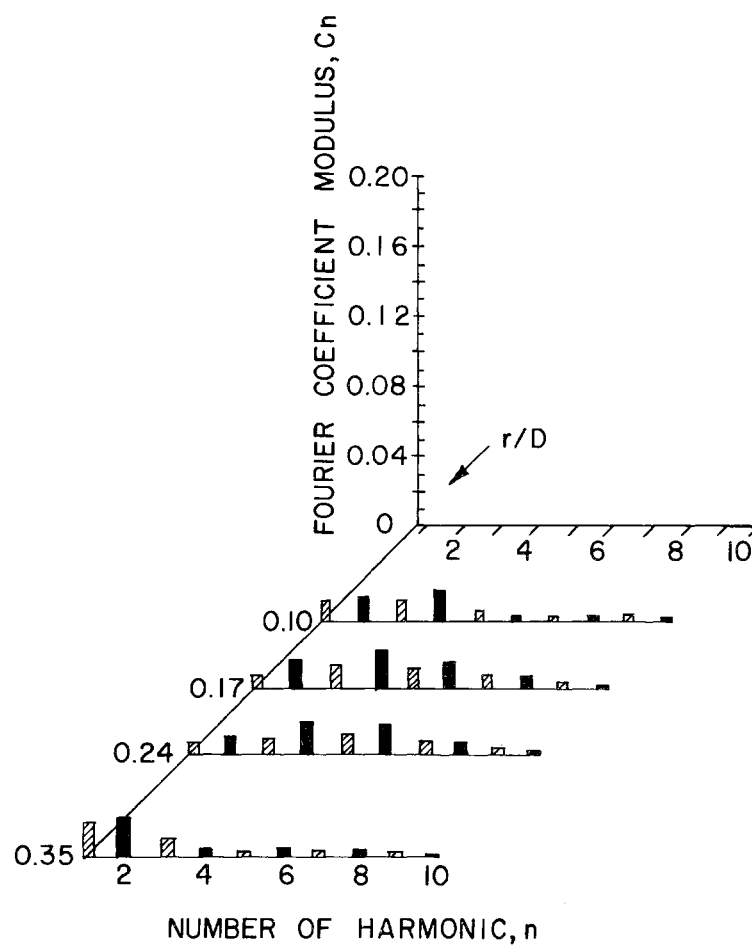
Fig. 23   Harmonic Content of Flow Field for Body with Forward
Fin Only and without Propeller

the signals from the wires were recorded on the magnetic tape recorder (CEC, Type GR 2800).

This method was used to obtain data for both the bare-body configuration and for the body equipped with propeller.

Time lags were introduced by the computer by displacing the data during the computing process. To be able to use the available computer facilities for the actual correlation, the data had to be converted to digital form. This meant that each output signal (in volts) was transformed into an integral number corresponding to its magnitude. The correlations were then performed with these numbers. Typical correlation functions are shown in Figs. 10 and 11.

Mathematically, the auto-correlation function is defined by

$$R_{ii}\left(\frac{\tau U}{\delta^*}, 0, 0, \frac{x_3}{\delta^*}\right) = \lim_{T \to \infty} \frac{1}{T} \int_{-T}^{T} u_i(t)\, u_i(t + \tau)\, dt \quad ,$$

where $u_i(t)$ is the signal from either probe representing the velocity fluctuations measured by that probe. Note that, in general, the correlation may be represented by

$$R_{ii}\left(\frac{\tau U}{\delta^*}, \frac{x_1}{\delta^*}, \frac{x_2}{\delta^*}, \frac{x_3}{\delta^*}\right) \quad ,$$

where $x_1$, $x_2$, and $x_3$ are the displacements along the coordinate axes. Here, only $x_3/\delta^*$ is considered. ($x_3$ denotes the circumferential direction, $x_2$ the radial, and $x_1$ the axial).

Thus, from the above, the autocorrelation function can be obtained for each probe at any location.

In general, the cross-correlation function is defined by

$$R_{ij}\left(\frac{\tau U}{\delta^*}, 0, 0, \frac{\chi_3}{\delta^*}\right) = \lim_{T \to \infty} \frac{1}{T} \int_{-T}^{T} u_i(t) \, u_j(t+\tau) \, dt \quad ,$$

where $u_i(t)$ and $u_j(t)$ denote the fluctuating velocities measured by the probes.

To normalize the correlation functions, let the auto-correlation for zero time lag of the movable probe be denoted by $R_{(xx)_0}$ and that for the reference probe by $R_{(yy)_0}$. Then, since the function is even, the limits of integration can be changed to 0 and T with the value of the integral doubled. Therefore,

$$R_{(xx)_0} = \lim_{T \to \infty} \frac{2}{T} \int_{0}^{T} u_1(t)^2 \, dt \quad ,$$

and

$$R_{(yy)_0} = \lim_{T \to \infty} \frac{2}{T} \int_{0}^{T} u_2(t)^2 \, dt \quad .$$

Further denote the autocorrelation of the movable probe as $R_{xx}$ and that of the stationary probe as $R_{yy}$. Then, the normalized autocorrelations become:

$$R_{(xx)_n} = \frac{R_{xx}}{R_{(xx)_0}} = \frac{\lim\limits_{T \to \infty} \frac{2}{T} \int_{0}^{T} u_1(t) \, u_1(t+\tau) \, dt}{\lim\limits_{T \to \infty} \frac{2}{T} \int_{0}^{T} u_1(t)^2 \, dt} \quad )$$

and

$$R_{(yy)_n} = \frac{R_{yy}}{R_{(yy)_o}} = \frac{\lim\limits_{T \to \infty} \frac{2}{T} \int_0^T u_2(t)\, u_2(t+\tau)\, dt}{\lim\limits_{T \to \infty} \frac{2}{T} \int_0^T u_2(t)^2\, dt}$$

For the cross-correlation of the movable probe relative to the reference probe, denote the functions as $R_{xy}$ for $\tau > 0$ and $R_{yx}$ for $\tau < 0$.

Using the previous notation for the autocorrelation at $\tau = 0$, the normalized functions are given by

$$R_{(xy)_n} = \frac{R_{xy}}{\left(R_{(xx)_o}\right)^{1/2} \left(R_{(yy)_o}\right)^{1/2}}$$

$$= \frac{\lim\limits_{T \to \infty} \frac{1}{T} \int_0^T u_1(t)\, u_2(t+\tau)\, dt}{\left[\lim\limits_{T \to \infty} \frac{2}{T} \int_0^T u_1(t)^2\, dt\right]^{1/2} \left[\lim\limits_{T \to \infty} \frac{2}{T} \int_0^T u_2(t)^2\, dt\right]^{1/2}}$$

and

$$R_{(yx)_n} = \frac{R_{yx}}{\left(R_{(xx)_o}\right)^{1/2} \left(R_{(yy)_o}\right)^{1/2}}$$

$$= \frac{\lim\limits_{T \to \infty} \frac{1}{T} \int_{-T}^0 u_1(t+\tau)\, u_2(t)\, dt}{\left[\lim\limits_{T \to \infty} \frac{2}{T} \int_0^T u_1(t)^2\, dt\right]^{1/2} \left[\lim\limits_{T \to \infty} \frac{2}{T} \int_0^T u_2(t)^2\, dt\right]^{1/2}}$$

The cross-correlation functions in their normalized form are shown in Appendix III for various values of $x_3$.

E. Description of Procedure and Equipment for Obtaining Correlation Functions by Computer Methods

The computer utilized was the DDP-19 made by Computer Control Corp. It is a solid-state, binary, parallel, 19-bit-word, single-address, general-purpose computer. The memory is random access with a magnetic core storage of 4096 words. The machine access time is 3 microseconds and it is capable of 100,000 additions per second. The input-output features include:

60-character-per-second paper-tape punch

300-character-per-second photoelectric paper-tape reader

15-character-per-second typewriter

300-line-per-minute printer.

The system contains two magnetic-tape recorders: one is a direct-recording, 10-channel, 20-inch-per-second unit with a packing density of 333 bits per inch; the other is a 75-inch-per-second unit with packing densities of 200 and 556 bits per inch. This tape system is compatible with the IBM 729 Mod II magnetic-tape unit.

Also included in the input-output features are a 200-increment-per-second plotter, three digital-to-analog conversion channels, and a fast serial input line for in-lab testing of experimental systems.

This computer has one built-in index register of 12 bits and an interrupt feature for priority control.

The original signal consisted of the hot-wire output and was

recorded on magnetic tape in analog form. These recordings represent velocity fluctuations as seen by the wire and were proportional to some voltage.

The tapes were then processed to obtain a frequency analysis of the signal. These analyses give an indication of the size and concentration of the energy content. A typical analysis can be seen in Fig. 24. Figure 25 shows the same spectrum but from wide-band frequency considerations. Once these tapes were so analyzed, it was necessary to convert the signal to digital form. Because of the digitizing equipment involved, the original tapes had to be re-recorded to filter out any signal above 1 kc. This was done by using two sets of Spencer-Kennedy Laboratories Inc., variable-frequency electronic filters, Model No. 302, and resulted in the signal shown in Fig 26. This figure is a wide-band analysis similar to Fig. 25. The rejection rate was found to be of the order of 50dB per octave from 1 kc to 2 kc.

Now that the signals were revised a bias voltage was applied in order to bring the level of the signal to a range from 0 to 10 volts d-c. This alteration was again necessitated by the electronic equipment used for digitizing.

With the voltage now in this range, the signal was digitized so that each sample voltage corresponded to an integer between 1 and 127. This is the range used by the computer for the calculations by binary methods. The digitized input signal was sampled at a rate of 3.3 kc. This corresponds to a piece of data 1500 words long. (One word is a seven-digit number representing voltage as described
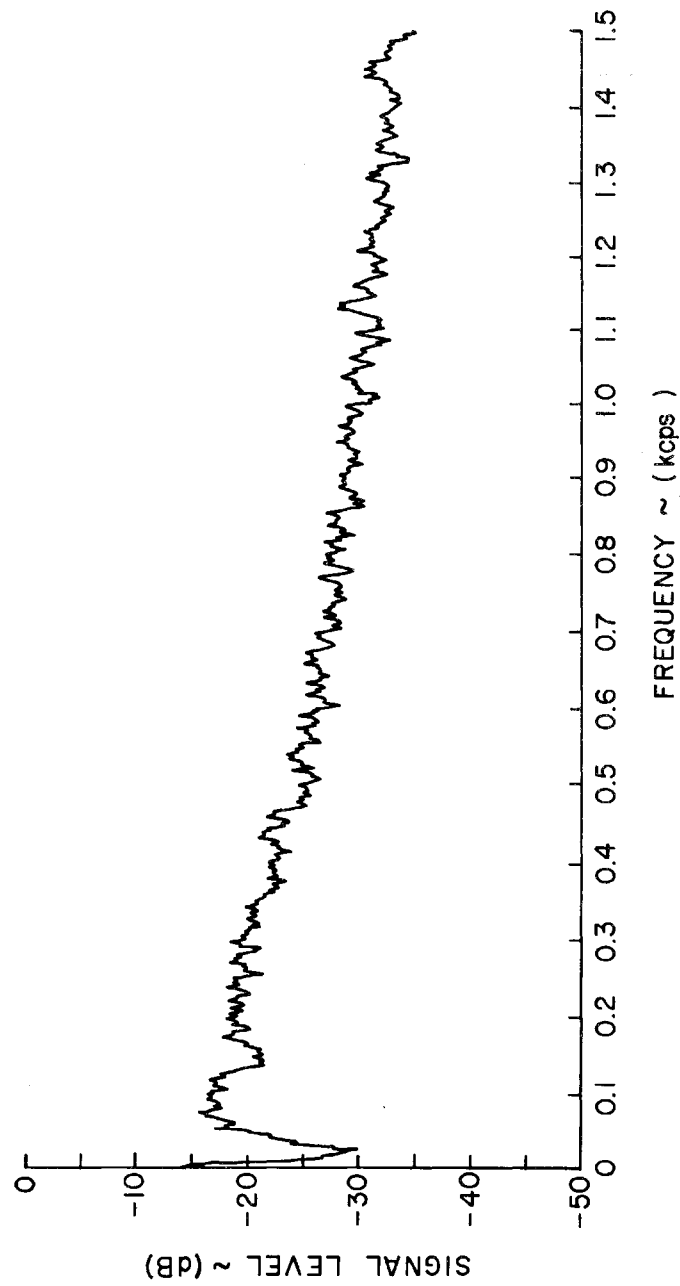
Fig. 24   Narrow-Band Frequency Analysis of Hot-Wire Signal for
Body without Propeller at r/D = 0.17 and Θ = 0 deg
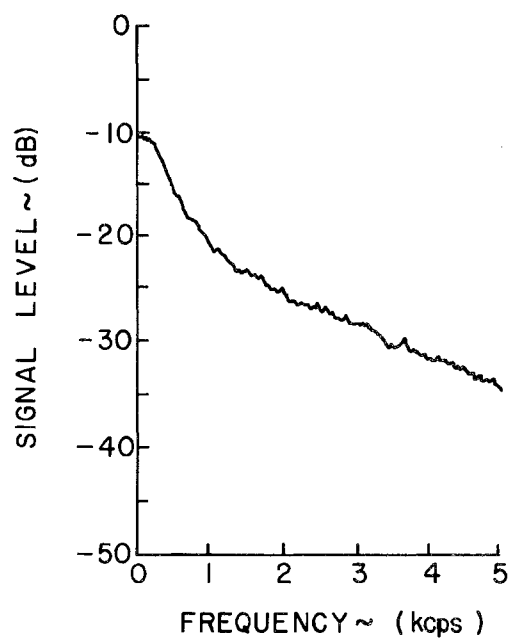
Fig. 25   Wide-Band Frequency Analysis, Before Filtering, for
Same Conditions as in Fig. 24
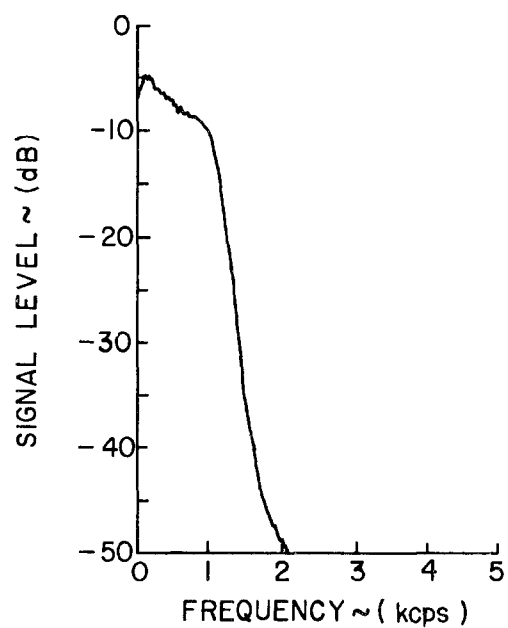


Fig. 26   Wide-Band Frequency Analysis, After Filtering above 1 kc,
for Same Conditions as in Fig. 24

above.)  In the actual sampling, there is a delay of 300 microseconds between words so that the sample taken amounted to 0.450 sec of actual data.  It was subsequently found that this sample size was insufficient to give repeatable results.  A method was used whereby the sampled data represented 2.5 sec of actual data, which was sufficient to give repeatable results.

The data from the wires was recorded on two channels of the CEC-GR2800, seven-channel tape recorder.

Figure 27 is a sample of the data in digitized form.  Each jump on the curve represents one word.  When calculating autocorrelation functions, the signals are moved relative to themselves and relative to each other in the case of cross-correlation-function calculations.  Schematically, the relative displacements can be shown as follows:

$$\boxed{\text{1500 words - wire 1}}$$

$$- t \longleftarrow \longleftarrow K \longrightarrow \boxed{\text{1500 words - wire 1}} \longrightarrow \quad + t$$

for the autocorrelation, and

$$\boxed{\text{1500 words - wire 1}}$$

$$- t \longleftarrow \longleftarrow K \longrightarrow \boxed{\text{1500 words - wire 2}} \longrightarrow \quad + t$$

for the cross-correlation.
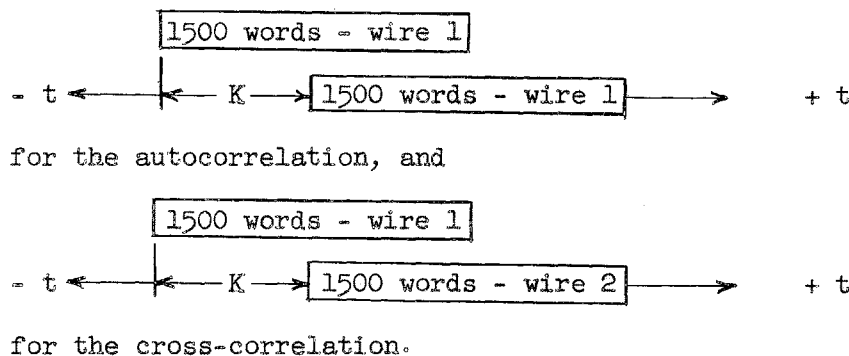
K is the increment by which the data are displaced by the computer when performing the correlation-function calculations.  It is the delay time of 300 microseconds between sample words, and is an integer ranging from zero to $N=K_{max}=1500$.  As seen in Fig. 10,

50
WORDS
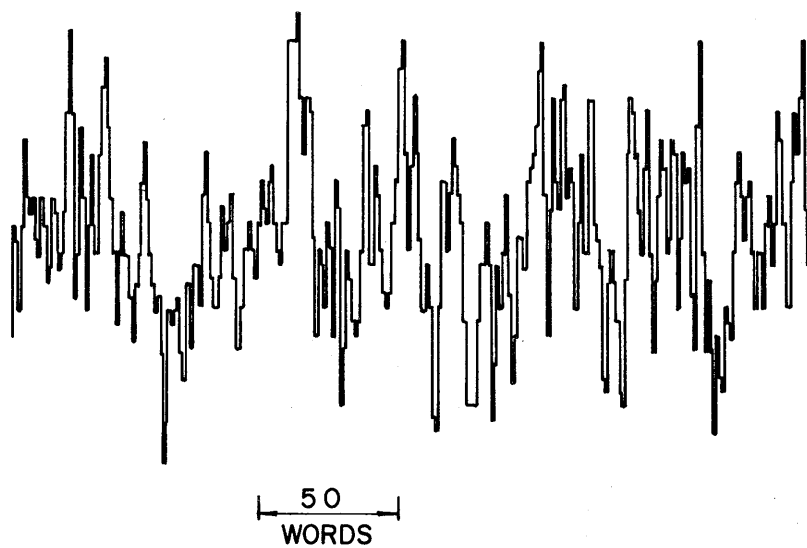
Fig. 27   Representative Sample of Hot-Wire Output Signal in
          Digitized Form

the correlation function approaches zero as K approaches 100, which corresponds to a time over which the signals are correlated of approximately 30 milliseconds.

The preceding equations for the required correlations did not include the bias necessary to raise the signal level; therefore, it was removed by subtraction when the correlation functions were computed. This was accomplished by averaging the sample words and subtracting this average from each word. Once the words were so reduced, the actual calculations were performed.

For any given time delay, $K = 0,1,\ldots N$, certain words from one channel line up with words from the other channel (see schematic). These combinations were then multiplied and the result divided by the number of words used, N-K.

CHAPTER IV

THEORETICAL CONSIDERATIONS AND DISCUSSION

A.  Character of the Solution

The theoretical approach to the problem is based on the
solution to the boundary-layer equations for an axisymmetric body of
revolution as given by Truckenbrodt.(4)

The character of the solution is such that only two
quantities need be specified:  the ideal potential flow over the
original body and the Reynolds number $\frac{U_\infty \ell}{\gamma}$  based on body length.
With only these quantities, the flow field can be obtained for the
body under consideration.  This flow field will be composed of a
laminar portion to transition, transition to turbulent flow and,
finally, the turbulent region.

The solution for the laminar portion up to the transition
point is based on the method due to Von Kármán and Pohlhausen.  This
solution applies to two-dimensional boundary layers and is used with
Truckenbrodt's method in the laminar region.  According to
Truckenbrodt, the necessary quantities preceding transition are
based on the solution for the two-dimensional flat plate.  His
solution applies these values to the turbulent boundary layer on the
axisymmetric body of revolution.  This completes the solution for
the body without fins.

The fins were added, and the solution was modified to account

for their presence. The effects of the fins on the flow were
determined with the aid of Reference 7, and the resulting flow into
the propeller was found.

B. Truckenbrodt's Method

Truckenbrodt's method consists in using the energy integral
equation to calculate the momentum thickness rather than the more
familiar momentum integral. The basic assumption in this theory is
that the velocity profile in the boundary layer obeys a power law of
the form

$$\frac{\bar{u}}{U} = \left(\frac{y}{\delta}\right)^{1/n} \qquad . \tag{1}$$

The basic equation for the distribution of the momentum thickness
along the body as a result of the energy integral equation,

$$\frac{d\left(U^3 \delta^{**}\right)}{dx} = 2\,\mathcal{V}\int_0^\infty \left(\frac{\partial u}{\partial y}\right)^2 dy \quad , \tag{1a}$$

has the form

$$\frac{\vartheta(x)}{\ell} = \frac{\left[C_1^* + \left(\frac{1}{2}c_f\right)^{(n+1)/n} \int_{x_*/\ell}^{x/\ell} \left(\frac{\bar{u}}{U_\infty}\right)^{3+2/n} \left(\frac{R}{\ell}\right)^{(n+1)/n} d\left(\frac{x}{\ell}\right)\right]^{n/(n+1)}}{\left(\frac{\bar{u}}{U_\infty}\right)^3 \left(\frac{R}{\ell}\right)} \quad , \tag{2}$$

where

$$C_1^* = \left\{ \frac{1}{2} c_{f\ell} \left[ \int_0^{\chi_t/\ell} \left(\frac{\bar{u}}{U_\infty}\right)^5 \left(\frac{R}{\ell}\right)^2 d\left(\frac{\chi}{\ell}\right) \right]^{1/2} \right\}^{(n+1)/n} \quad (3)$$

is a constant that takes into account the laminar portion of the boundary layer up to the transition point $\chi_t/\ell$ . Here, $\ell$ is the factor by which linear quantities are made dimensionless.

The symbol $C_f$ in equation 2 denotes the coefficient of skin friction of a flat plate at zero angle of attack in turbulent flow at a Reynolds number $R_\ell = \dfrac{U_\infty \ell}{\nu}$ from transition to $\chi/\ell$ . The symbol $C_{f\ell}$ in equation 3 is the coefficient of skin friction of a flat plate in laminar flow at a Reynolds number $\dfrac{U_\infty \chi}{\nu}$ from the nose to the transition point $\chi_t/\ell$ .

The quantity $\bar{u}/U_\infty$ that appears in both equations is the ideal potential velocity distribution for the body. (This is assumed known from Fig. 28). In equation 2, $\chi$ is actually a measure along the body curvature rather than along the axis. For convenience, the measure of curvature has been changed to $S$ ; $\chi/\ell$ represents the axial position. Also, $R/\ell$ is the radius of a cross-section taken normal to the axis at the position $\chi/\ell$ .

In the above equations, the constant $n$ has been empirically determined and is given as 6 for turbulent flow at a large Reynolds number. In this case $R_\ell = 5.5 \times 10^6$, based on body length.

The remaining quantity to be determined is the variation of the shape factor $L(S)$ or $H(S)$ . This will then give the

AXIAL LENGTH ALONG BODY, $x/\ell$

VELOCITY RATIO ON BODY SURFACE, $\dfrac{U_{tan}}{U_\infty}$
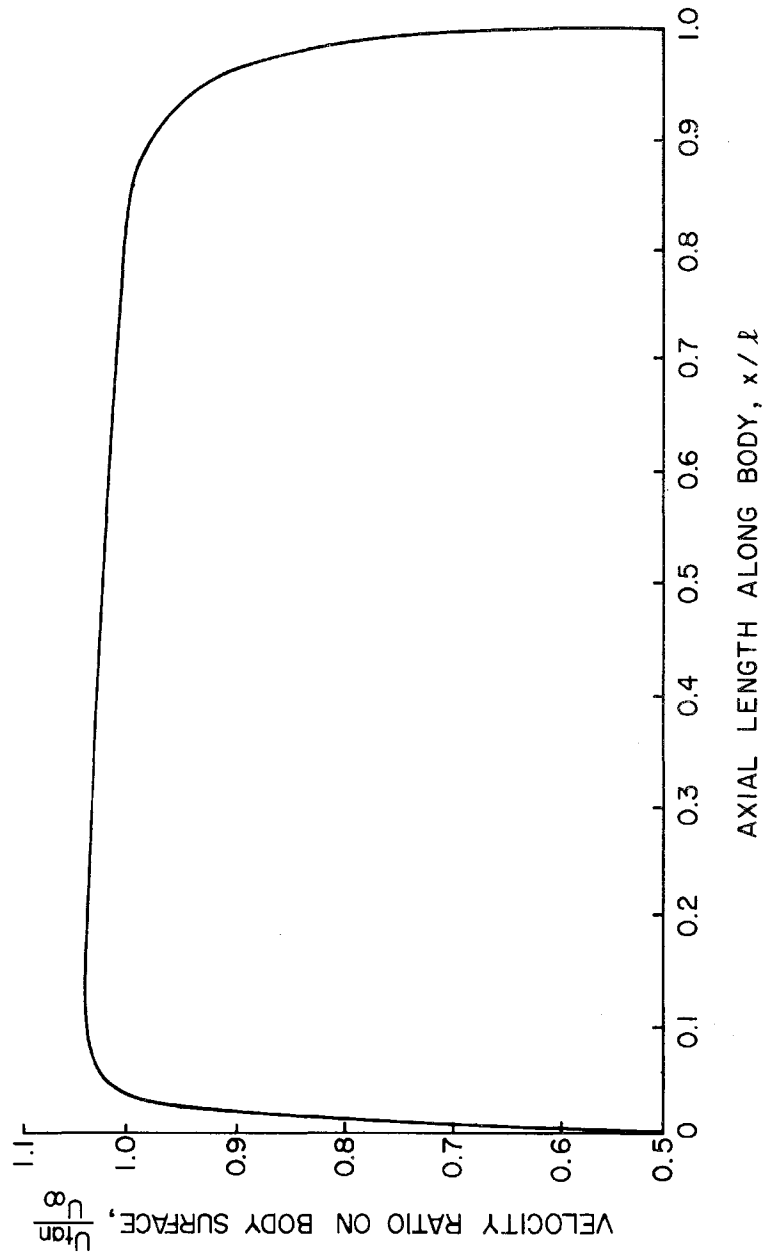
Fig. 28  Ideal Potential-Velocity Distribution for the Streamlined
Body Used in the Experiments

required displacement thickness $\delta^*$ , since $H = \delta^* / \vartheta$ . The shape factor $L$ is determined by

$$L = \frac{\xi_1}{\xi} L_1 + \ln \frac{U(\xi)}{U_1} + \frac{1}{\xi} \int_{\xi_1}^{\xi} \left[ b(\xi) - \ln \frac{U(\xi)}{U_1(\xi_1)} \right] d\xi \quad , \quad (4)$$

and $H$ is given by Fig. 29 once the value for $L$ is known.

In equation 4, the subscript " $|$ " refers to values at the transition point. The symbol $\xi$ is essentially a variable of integration that is given by

$$\xi = \left[ C_1^* + \left( \frac{1}{2} C_f \right)^{(n+1)/n} \int_{S_t}^{S} \left( \frac{\overline{u}}{U_\infty} \right)^{3 + 2/n} dS \right]^m \quad , \quad (5)$$

where $n = 6$ and $m$ is assumed to be 4. NOTE: at transition,

$$\xi_1 = \left( C_1^* \right)^m \quad .$$

Once the values at transition have been determined, as shown below, the momentum thickness is found from equations 2 and 3.

The Reynolds number based on momentum thickness can now be found:

$$R_\vartheta = \frac{U_\infty \vartheta(s)}{\nu} = R_\ell \left( \frac{\vartheta(s)}{\ell} \right) \quad , \quad (6)$$
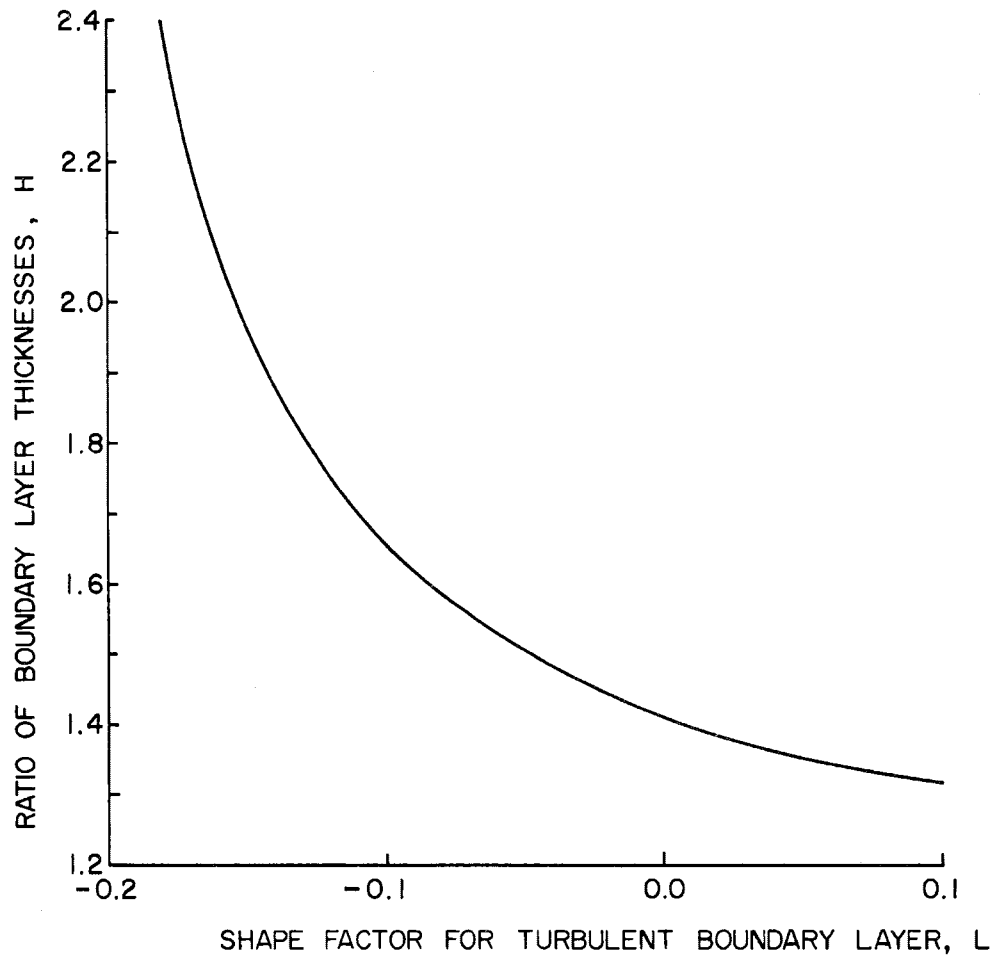
Fig. 29  Determination of Shape Factors, H and L, in Conjunction
with Equations 4 and 5

so that the quantity $b(S)$ can be obtained for equation 4 as

$$b(S) = 0.07 \log_{10} R_{\mathcal{G}} - 0.23 \quad . \tag{7}$$

Thus, $L(S)$ is known and $H(S)$ is found; therefore, $\delta^*(S)$ is specified.

C. Determination of the Transition Point--Method of Von Kármán and Pohlhausen for the Laminar-Flow Region

The problem remains to find those quantities associated with the laminar flow regime and the determination of the transition point $\chi_t / \ell$ or $S_t$. The original body configuration is established which results in the parameters $\chi / \ell$ and $y_o / \ell$. The potential flow solution is found using A. M. O. Smith's method for the exact solution of the Neumann Problem. (8) Briefly, the method involves the numerical solution of a surface source distribution that is assumed constant over finite segments of the body. The coordinates are changed from axial to meridional by simple triangulation. Thus,

$$S = \sqrt{(\Delta \chi)^2 + (\Delta y)^2} \Big/ \ell \quad . \tag{8}$$

Now, knowing the relationship between $\bar{u} / U_\infty$ and $S$, the Reynolds number, based on momentum thickness, can be found as follows:

$$R_\vartheta^2 = \left(\frac{U\vartheta}{\mathcal{D}}\right)^2 = \frac{0.47\ R_\ell}{\left(\frac{\bar{u}}{U_\infty}\right)^4} \int_0^{s \le s_t} \left(\frac{\bar{u}}{U_\infty}\right)^5 ds \qquad . \tag{9}$$

Following Pohlhausen's method, use is made of several shape factors such as

$$K = \frac{\vartheta^2}{\mathcal{D}} \frac{dU}{d\chi} \qquad , \tag{10}$$

$$\Lambda = \frac{\delta^2}{\mathcal{D}} \frac{dU}{d\chi} \qquad , \tag{11}$$

and the already familiar shape factor, $H = \delta^*/\vartheta$ . In the above, $\delta$ is the actual boundary-layer thickness. It will be seen how each of these shape factors aids in finding the transition point.

The shape factors, $K$ and $\Lambda$, can be more conveniently written with the aid of equation 9 and the body Reynolds number. Thus,

$$K = R_\vartheta^2 \frac{1}{R_\ell} \frac{1}{\left(\frac{\bar{u}}{U_\infty}\right)^2} \frac{d\left(\frac{\bar{u}}{U_\infty}\right)}{ds} \qquad . \tag{12}$$

It has been found that $K$ and $\Lambda$ satisfy the universal relation

$$K = \left(a + b\Lambda + c\Lambda^2\right)^2 \Lambda \quad , \tag{13}$$

where $a$, $b$, and $c$ are constants whose values are given in Appendix II. The shape factor $H$ can also be written in terms of $K$ and $\Lambda$:

$$H = \frac{\delta^*}{\vartheta} = \frac{d + e\Lambda}{\left(K/\Lambda\right)^{1/2}} - \Delta H \quad , \tag{14}$$

where, again, $d$ and $e$ are constants and are also given in Appendix II. The term $\Delta H$ is an empirical factor relating the change in $H$ across the transition region, since $K$ and $\Lambda$ apply only for the laminar portion. Here, $\Delta H$ was chosen of the order of 1.2.

The necessity for the above development is to find the relationship of $\Lambda$ and $\delta^*$ in terms of $S$, the arc length measured from the forward stagnation point. Associated with the flow downstream from the forward stagnation point is the ability of the boundary layer to remain stable and not to become turbulent. The limit of stability is the point at which the boundary layer changes from the stable laminar one to the unstable turbulant one. The Reynolds number associated with the limit of stability is known as the "critical" Reynolds number. As long as the local Reynolds number $U_m \delta^*/\vartheta$ remains less than the critical one $\left(U_m \delta^*/\vartheta\right)_{crit}$ , the boundary layer remains stable.

As the flow proceeds downstream, the rate of pressure decrease becomes smaller and, consequently, is followed by an increase in pressure that is due to the adverse pressure gradient. Thus, at some downstream position, $U_m \delta^*/\upsilon$ increases to the local limit of stability $\left( U_m \delta^*/\upsilon \right)_{crit}$ ; and the boundary layer becomes unstable. The position associated with this change is the transition point; it is defined as

$$\left. \begin{array}{c} \chi = \chi_t \\ \text{or} \\ s = s_t \end{array} \right\} \quad \text{for} \quad \frac{U_m \delta^*}{\upsilon} \equiv \left( \frac{U_m \delta^*}{\upsilon} \right)_{crit} . \quad (15)$$

Certain empirical findings permit the determination of the transition point with relative ease.

Figure 30 shows the variation of $\Lambda$ with $\left( U_m \delta^*/\upsilon \right)_{crit}$ , which then gives the variation of $s$ with $\left( U_m \delta^*/\upsilon \right)_{crit}$ , since $s$ vs $\Lambda$ is known from equation 11. From equation 9, $R_\upsilon$ vs $s$ is known, which is just the value of the local Reynolds number since

$$\frac{U \delta^*}{\upsilon} = \left[ \left( \frac{U \upsilon}{\upsilon} \right)^2 H^2 \right]^{1/2} = \sqrt{R_\upsilon^2 H^2} = R_\upsilon H . \quad (16)$$

Thus, Fig. 31 is obtained, which shows $U\delta^*/\upsilon$, $\left( U\delta^*/\upsilon \right)_{crit}$ vs $s$. By the definition given in equation 15, the transition point is located at the intersection of these two curves. The displacement thickness $\delta^*$ and momentum thickness $\upsilon$ are found as functions of $s$ for the laminar region simply as
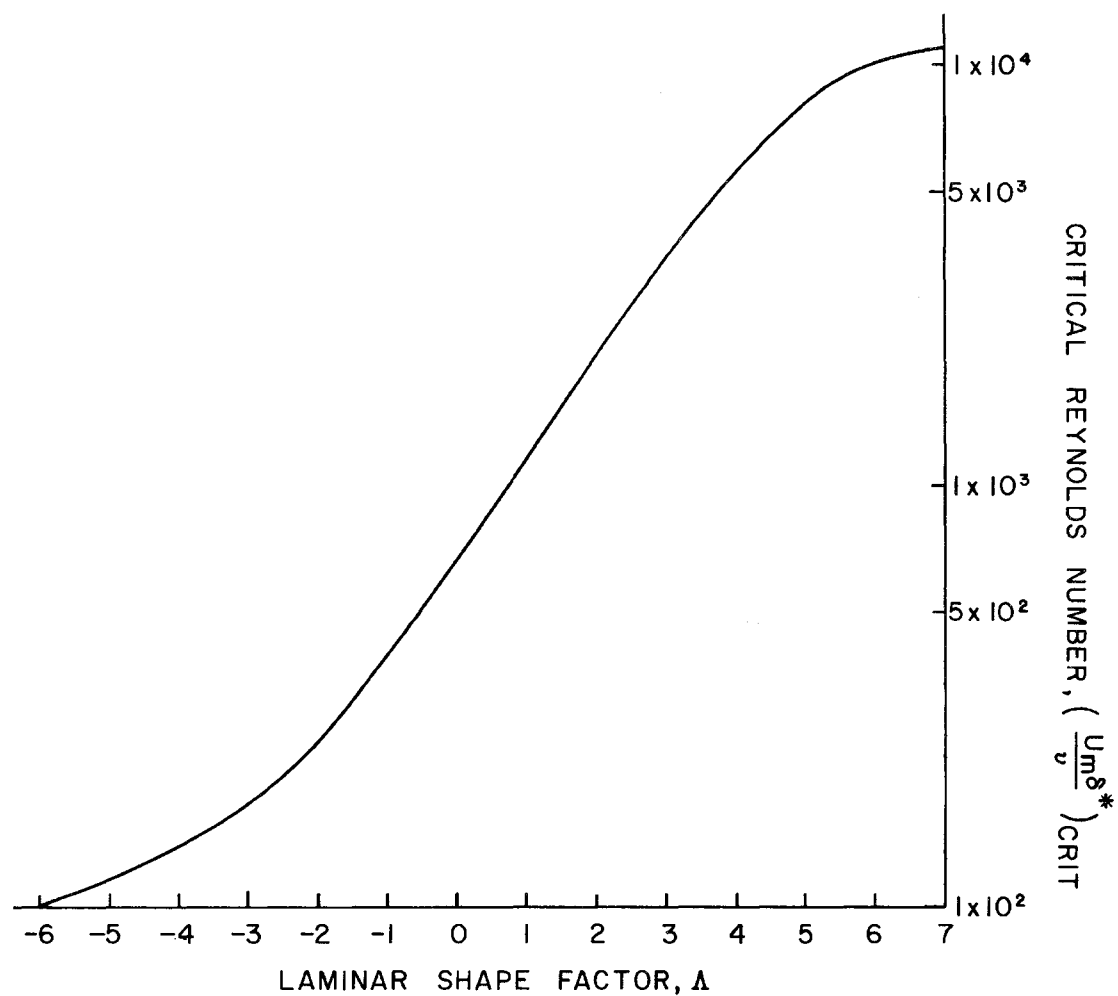
Fig. 30  Critical Reynolds Number for Bodies with Adverse Pressure
Gradient as a Function of Laminar Shape Factor $\Lambda$
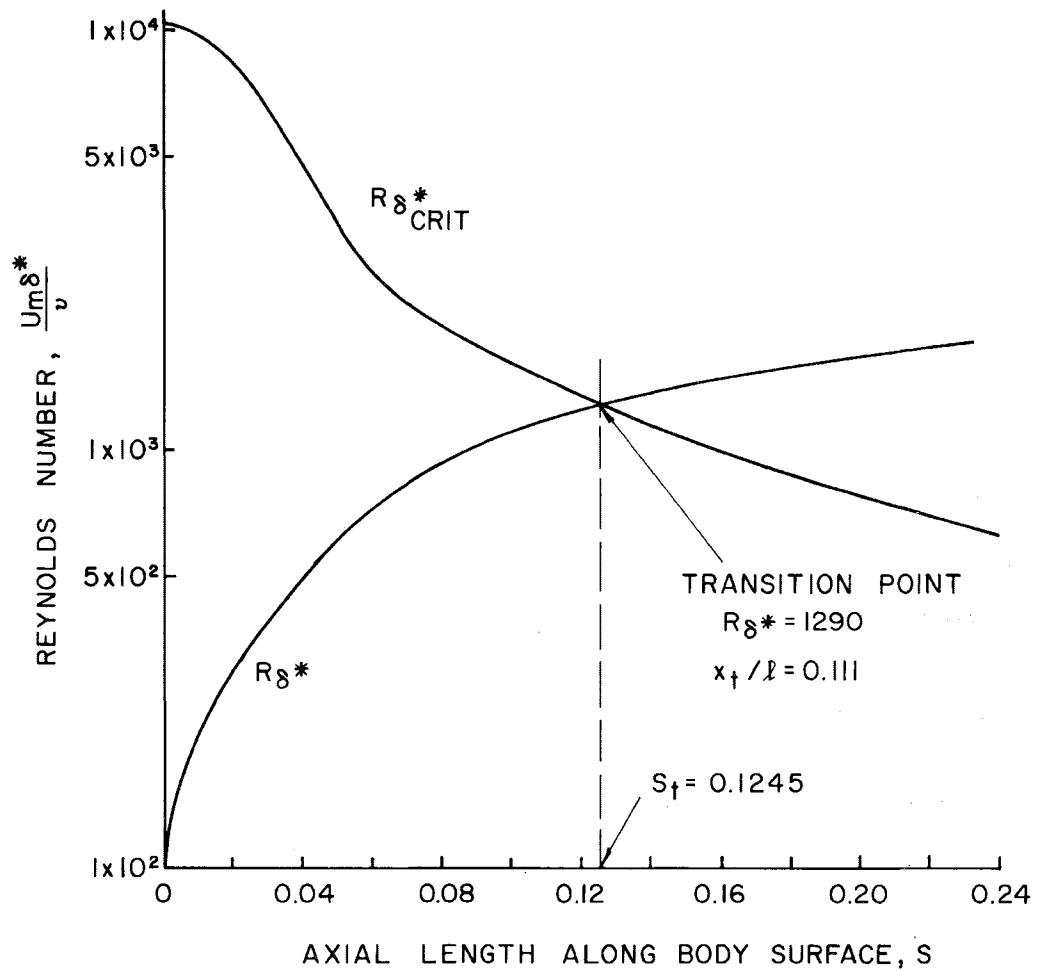
Fig. 31 Local Reynolds Number and Local Limit of Stability as a
Function of Position along Body

$$\vartheta/\ell = R_{\vartheta}/R_{\ell}$$

and $\qquad\qquad\qquad\qquad\qquad\qquad\qquad\qquad\qquad\qquad$ (17)

$$\delta^*/\ell = R_{\delta*}/R_{\ell} = \frac{\vartheta}{\ell}H \quad :$$

Therefore, all necessary items pertaining to the laminar flow field, up to and including the transition point, are now known. Thus, the calculations for the turbulent field may now be carried out with the above knowledge. The values at transition necessary for the remaining calculations are given in Appendix II.

The actual location of the transition point, as seen in Fig. 31, agrees with data presented in Reference 4 for work done on an 8:1 ellipsoid of revolution.

D. Technique for Finding the Displacement Thickness

The process of finding the displacement thickness approximation to the body involves the use of equations 2 through 8 in a process of iteration. This procedure was carried out until the values for $\delta^*$ on the $(n+1)^{th}$ approximation were within 5 per cent of those found for the $n^{th}$ case. The values used for the laminar portion and the transition region were those found after the first approximation since changes in these quantities are negligible. At the rear it took four approximations (n+1=5) to satisfy the above criterion. The final values chosen for $\delta^*$, and the other quantities associated with the boundary layer, are compared with the original body coordinates in Appendix II.

E.  Addition of Fins to the Body

After the solution for the bare-body configuration had been
obtained, the fins were added.  Reference 7 is an experimental
compilation of data for the wake profiles of struts in a streaming
flow.  With the inflow velocity at the strut leading edge known, the
characteristic parameters associated with the strut wake can be found.

The control-surface profiles are NACA 0015 symmetrical
airfoils whose profile drag coefficient $C_{do}$ was obtained with the
aid of Reference 9.  With this knowledge, the wake depth and breadth
of influence was determined (Fig. 32).

The inflow velocity to a fin was found from the boundary-layer
profile at the leading edge (Fig. 2-3, Appendix II).  This velocity
represents the actual free-stream velocity seen by the fin.  The
wake profiles were obtained at the corresponding radial distances
used in the experimental measurements.  Thus, at a particular value
of $r/D$, the profile is determined as a function of the
circumferential distance $\Theta$.  A plot of the profiles thus obtained
are shown in Fig. 3.  This figure compares these profiles with the
measured ones.

F.  The Vortex Effect

Figure 3 shows the close agreement between the predicted
wakes and the measured wakes far from the body--such as at
$r/D = 0.35$.  However, at $r/D = 0.10$, which is close to the
fin-and-body intersection, the agreement is less than anticipated
because of the presence of corner vortices shed by the fin near its
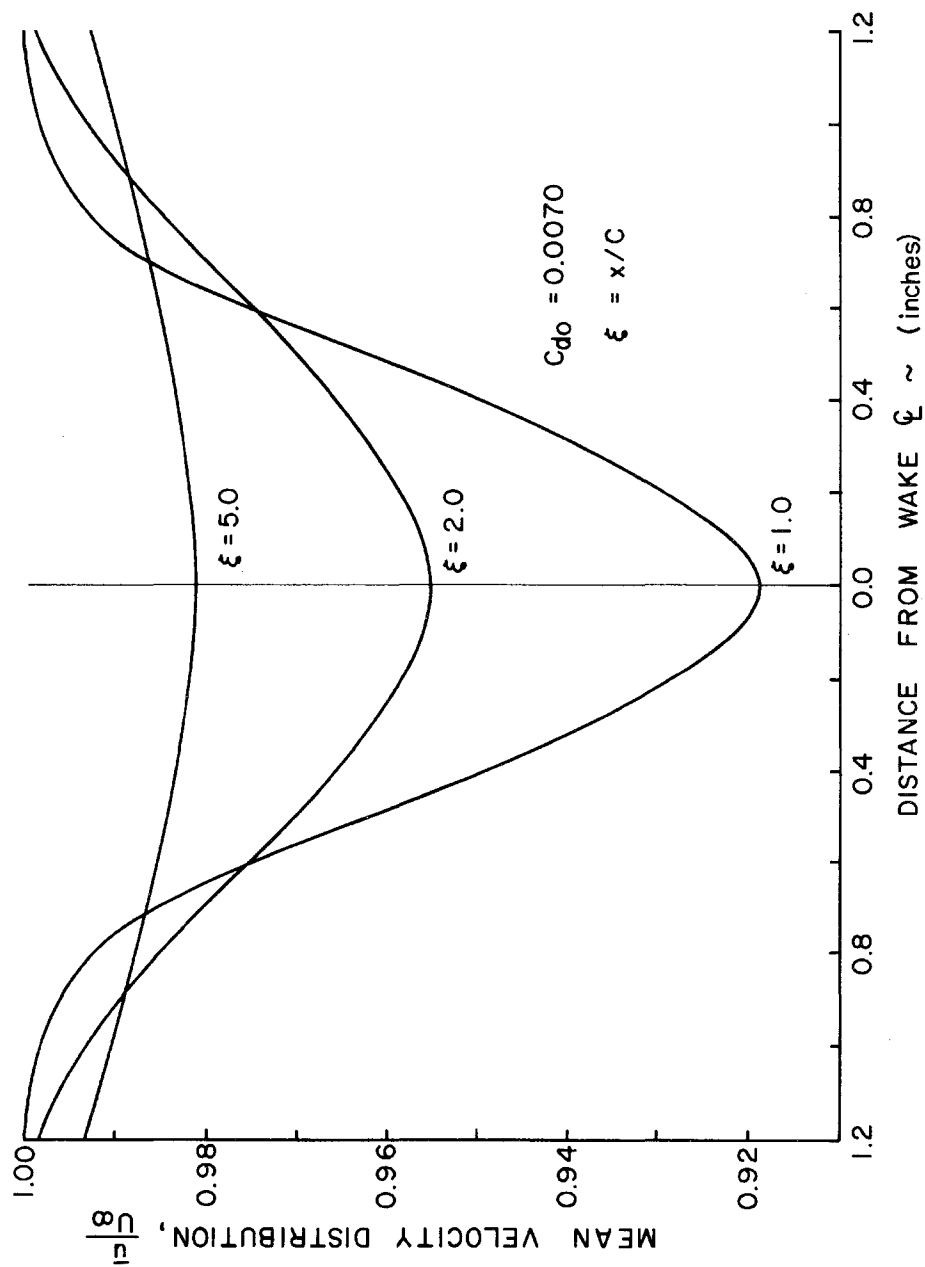root.  This vortex effect is the only flow condition that had not

Fig. 32 Mean-Velocity Wake Profile of Strut at Several Locations
Downstream of Trailing Edge

been accounted for in the use of the boundary-layer equations.

Subsequent testing has shown the presence of the vorticity and its relative strength. Figure 4 shows a vortex located on each side of a fin. The vortex was measured with the aid of a vorticity meter (Fig. 6) developed by Dr. B. W. McCormick, Jr. of the Department of Aeronautical Engineering, The Pennsylvania State University. This device was employed as a means of establishing the presence of the streamwise component of vorticity. Figure 4 shows the relative strength of the vortex before any attempts were made to eliminate it. If the vortex could be eliminated, the propeller would then be subjected to a uniform distribution of mean velocity at any value of r/D and for all values of $\Theta$ (Fig. 7). In this situation, the effects of the unsteady forces would be favorably reduced.

Efforts made to reduce the strength of the vortex included a technique whereby compressed air was forced out of holes made at the fin-and-body intersection (Fig. 5). Figure 7 shows the effects on the wake resulting from an air pressure of 5 psi. This method, then, appears to be a possible means of eliminating from the wake certain characteristics that can result in the undesirable operation of a propulsor.

CHAPTER V

CONCLUSIONS BASED ON EXPERIMENTAL STUDIES

A. Effects of the Propeller

    The results of the circumferential wake distributions, shown graphically in Appendix III, are summarized in Table II.

TABLE II

COMPARISONS OF RESULTS OF MEAN AND RMS VELOCITY BETWEEN
MODEL CONFIGURATIONS AT VARIOUS VALUES OF r/D

| r/D | Mean Velocity Ratio, $\bar{u}/U_\infty$ | | RMS Velocity Ratio, $u'/U_\infty$ | |
|------|-----------|-----------|-----------|-----------|
| | Bare Body | With Prop | Bare Body | With Prop |
| 0.35 | 0.933 | 0.919 | 0.0229 | 0.0221 |
| 0.24 | 0.765 | 0.876 | 0.0483 | 0.0241 |
| 0.17 | 0.537 | 0.697 | 0.0691 | 0.0447 |
| 0.10 | 0.326 | 0.575 | 0.0753 | 0.0358 |

(Note: the design advance ratio J is 0.406 for the model with propeller; also, $r < R_p$ when $r/D \leqslant 0.24$)

    A comparison of the measurements shows that the mean velocities are higher for the body with propeller than without. This is true when the radial position r/D is within the propeller radius ($r < R_p$). The opposite effect is noticed when traversing

radially a distance greater than the propeller radius $(r > R_p)$. It is also seen that the rms values are lower with the propulsor, which indicates that the propulsor has a smoothing effect on the flow. These rms results have agreed with previous work, and the turbulence levels obtained peak to a maximum of 10 per cent, which was measured on the bare body for $r/D = 0.10$ (Fig. 3-9). It is also to be noted that the mean-velocity distribution increases in magnitude when traversing radially outward from the body. This is expected because the flow field is greatly influenced by the turbulent boundary layer, which behaves in the same manner. This influence, which varies inversely from the body outward into the free stream, is negligible once the flow becomes potential.

It is felt that the higher mean velocities found with the propulsor are due to the streamlines being drawn into the body. The propulsor produces this effect because it acts as a favorable pressure gradient on the flow. This, then, reduces the turbulence level and speeds up the flow. Hence, the thickness of the boundary layer is decreased, and the region of potential flow is greater.

These effects produced by the propeller are more readily noted in the boundary-layer profile than in the wake profile. Figure 33 clearly illustrates the change in the flow as it passes through the propulsor. The change in the flow is thought of as being the decrease of the momentum deficit, which results from the reaction of the turbulent boundary layer to the propeller.

Figure 34 shows the change in the momentum deficit at the propeller inflow region. The change here is less than that
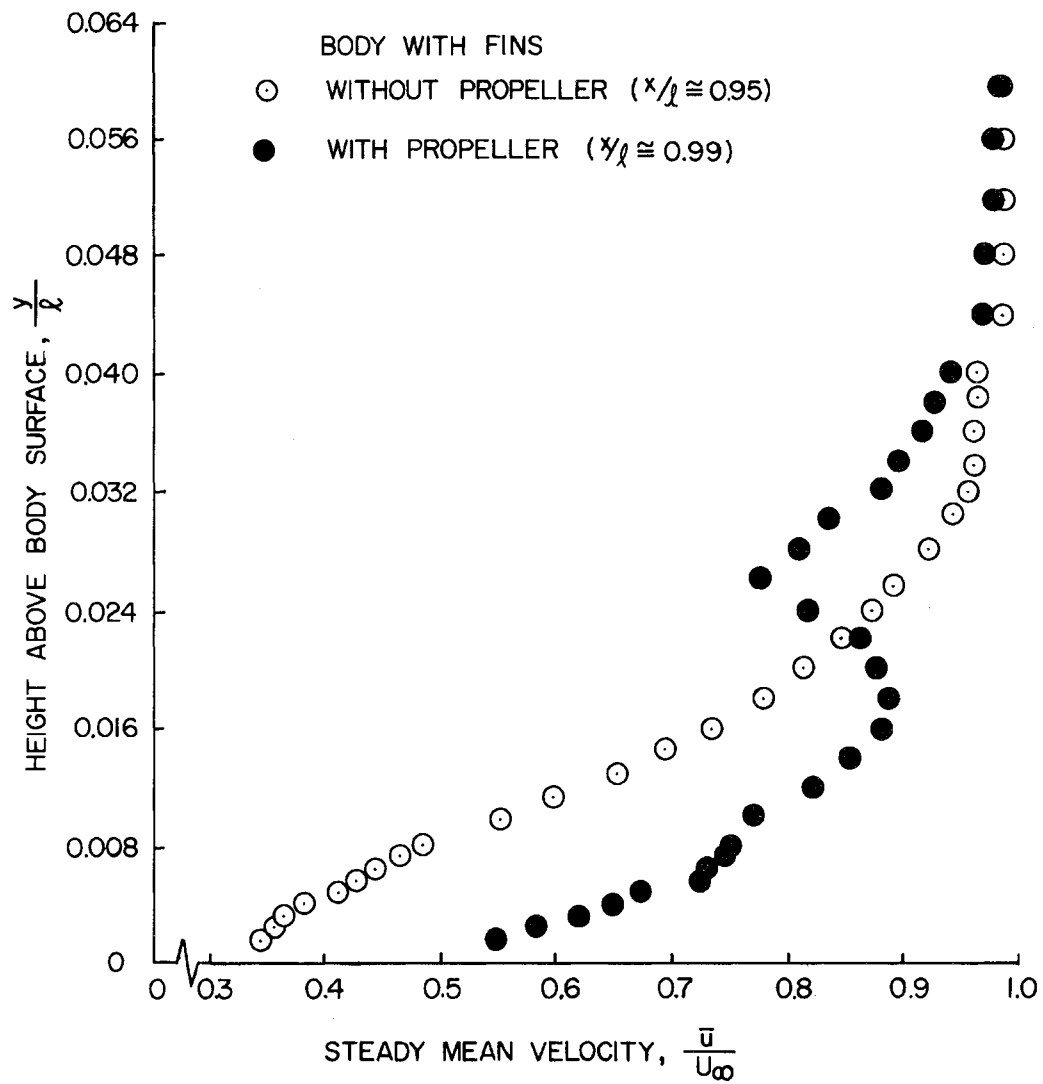
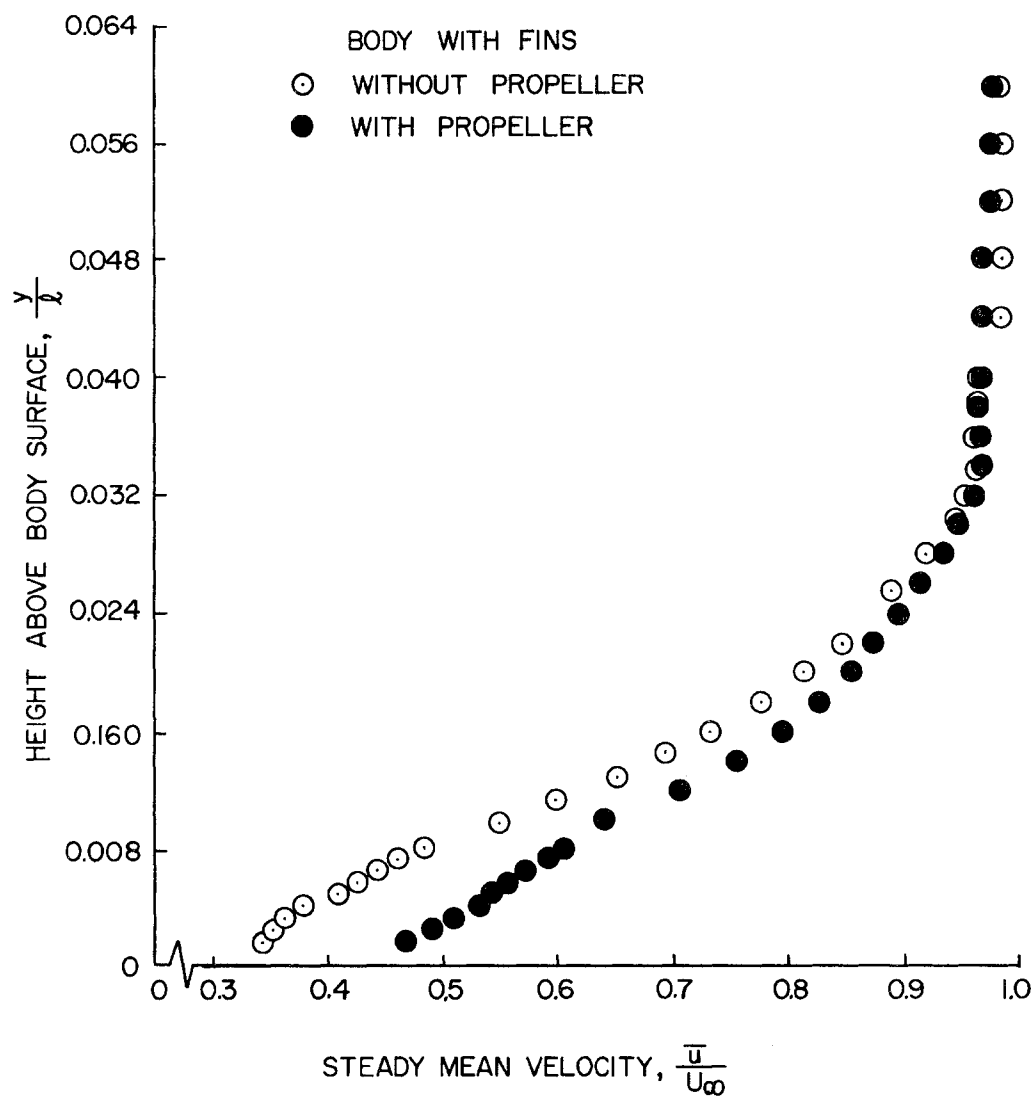Fig. 33  Boundary-Layer Profiles on Body with Fins

Fig. 34   Boundary-Layer Profiles on Body with Fins at Propeller
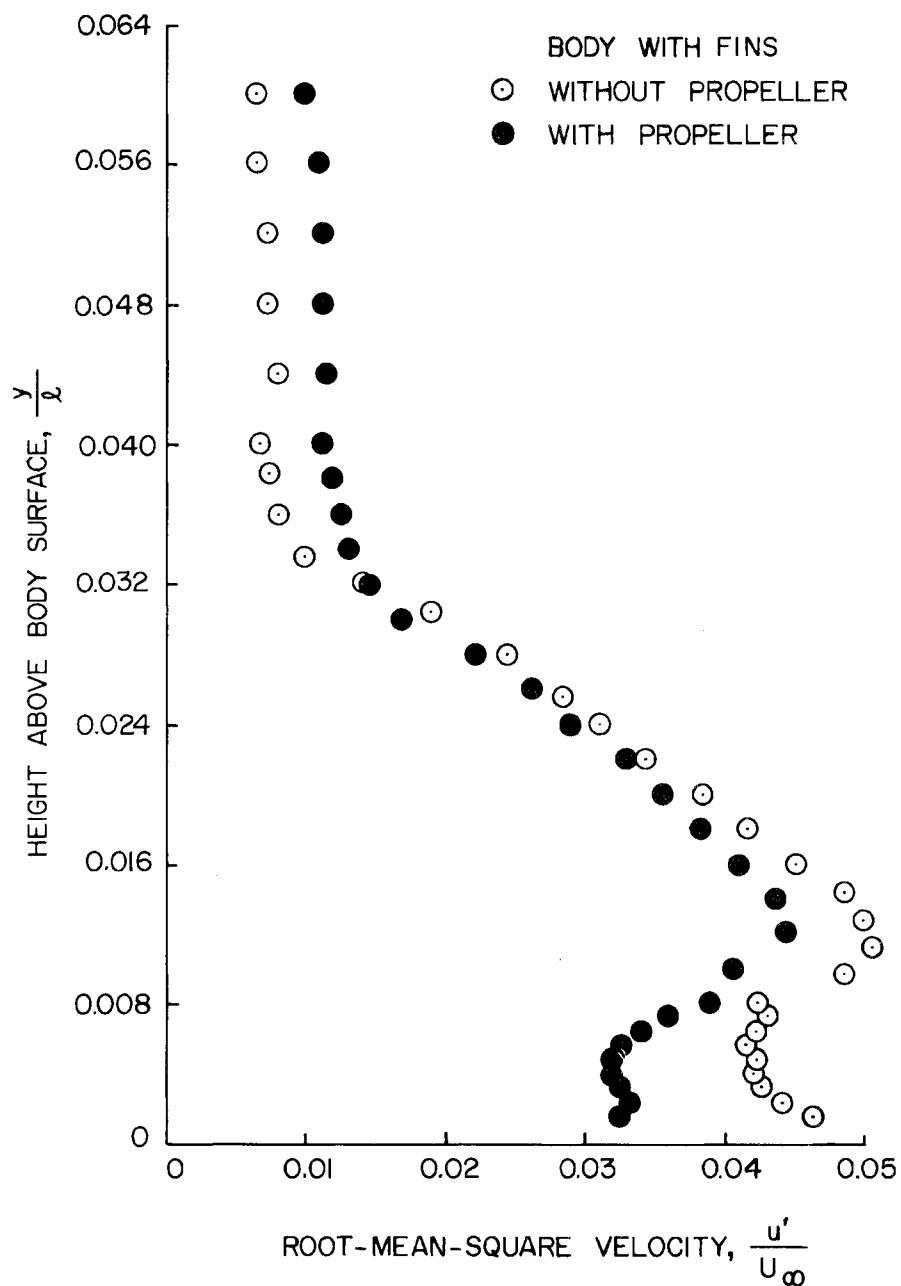Inflow

Fig. 35 Root-Mean-Square Velocity Distribution for Boundary-Layer Profile at Propeller Inflow

experienced by the flow as it passes through the propulsor.
Figure 35 further illustrates the decreasing turbulence level as a
result of the smoother flow created by the propeller. This figure
consists of the rms values for the boundary-layer profile shown in
Fig. 34.

B. Effects of the Fins

The normalized power spectra, obtained by passing the
hot-wire signal through a wave analyzer and integrator, are shown in
Fig. 9. These spectra are for the model with a propeller at two
different locations of r/D and $\Theta$. From Fig. 9 it is seen that, in
each case chosen, the maximum amount of energy occurs in a range of
nondimensional frequency $\omega \delta^*/U_\infty$, which is the equivalent of
70-80 cps. The largest amount of those shown occurs at the closest
position to the body and midway between the fins.

Associated with this energy are certain eddies produced by
the shed boundary layer. As already shown by the Fourier Analysis,
the effects on the propeller are diminished as the radial distance
increases from the body. By noting the differences between Fig. 22
and Fig. 23, and also from Table III, it is apparent that, as the
radial distance traversed exceeds the propeller radius, the
influence of the fin at the inflow region becomes negligible. This
was noted earlier when considering the region of potential flow
outside the influence of the boundary layer. However, it is seen
that the flow is greatly influenced by the fins when traversing
within a propeller radius of the body. The presence of the large
fourth harmonic close to the body (Fig. 22, r/D = 0.10 and 0.17)

TABLE III

COMPARISON OF HARMONIC CONTENT FOR THE BODY WITHOUT PROPELLER
AS A FUNCTION OF r/D AND TWO BODY CONFIGURATIONS*

Magnitude of the Fourier Coefficient Modulus, $C_n$

| n | r/D = 0.10 | | r/D = 0.17 | | r/D = 0.24 | | r/D = 0.35 | |
|---|---|---|---|---|---|---|---|---|
| 1 | 0.01713 | 0.01071 | 0.02603 | 0.00810 | 0.00972 | 0.00716 | 0.02712 | 0.01863 |
| 2 | 0.04712 | 0.01288 | 0.00831 | 0.01520 | 0.01824 | 0.01008 | 0.02056 | 0.02088 |
| 3 | 0.02638 | 0.01264 | 0.03204 | 0.01240 | 0.01609 | 0.00868 | 0.00470 | 0.00851 |
| 4 | 0.14969 | 0.01688 | 0.09900 | 0.02066 | 0.02442 | 0.01790 | 0.01504 | 0.00390 |
| 5 | 0.02134 | 0.00485 | 0.00576 | 0.01077 | 0.00812 | 0.01105 | 0.00570 | 0.00256 |
| 6 | 0.00846 | 0.00311 | 0.00732 | 0.01460 | 0.00734 | 0.01599 | 0.00868 | 0.00463 |
| 7 | 0.01378 | 0.00221 | 0.01686 | 0.00751 | 0.00814 | 0.00776 | 0.00722 | 0.00309 |
| 8 | 0.02340 | 0.00302 | 0.03384 | 0.00660 | 0.00557 | 0.00650 | 0.01227 | 0.00265 |
| 9 | 0.02001 | 0.00330 | 0.01130 | 0.00338 | 0.00345 | 0.00383 | 0.00265 | 0.00241 |
| 10 | 0.01468 | 0.00127 | 0.00211 | 0.00205 | 0.00420 | 0.00233 | 0.00507 | 0.00102 |

*Note: Under each value of r/D, the values in the left-hand column were obtained with all fins in place;
the values in the right-hand column were obtained with only the forward supporting strut in place.

gives an indication of the disturbance felt by the blade along its span. Figure 23 shows that the blade would feel relatively no disturbance along its span in the absence of fins. With this knowledge, the propeller designer is able to account for the unsteadiness and nonuniformities encountered by the blades. Thus, the response associated with the propeller-and-fin configuration is subject to control.

## C. Harmonic Content Close to Body Surface

It is of special interest to consider the harmonic content of the flow field in a region close to the body which affects the propeller. Figure 2, and the accompanying table, compare this content at a value of $r/D = 0.10$ for the cases of the body and fins, with and without the propeller. From Table IV it is seen that the magnitude of the dominant fourth harmonic is reduced. This occurs because the induction effects of the propeller reduce the influence of the turbulent boundary layer by smoothing the flow.

TABLE IV

COMPARISON OF HARMONIC CONTENT FOR THE STEADY MEAN-VELOCITY
PROFILE AT $r/D = 0.10$ FOR THE BODY WITH FINS

| n | Magnitude of the Fourier Coefficient Modulus, $C_n$ | |
| --- | --- | --- |
| | Without Propeller | With Propeller |
| 1 | 0.01713 | 0.02330 |
| 2 | 0.04712 | 0.00794 |
| 3 | 0.02638 | 0.02340 |
| 4 | 0.14969 | 0.11000 |
| 5 | 0.02134 | 0.02060 |
| 6 | 0.00846 | 0.00900 |
| 7 | 0.01378 | 0.00392 |
| 8 | 0.02340 | 0.01290 |
| 9 | 0.02001 | 0.01740 |
| 10 | 0.01468 | 0.00818 |

# REFERENCES

1. Lehman, A. F., "The Garfield Thomas Water Tunnel," Ordnance Research Laboratory, The Pennsylvania State University, 1959.

2. Kovasznay, L. S. G., Miller, L. T., and Vasudeva, B. R., "A Simple Hot-Wire Anemometer," Project Squid T.R.-JHU-22-P, University of Virginia, 1963.

3. Burstein, N. M., "Operating Instructions for Kovasznay Hot-Wire Amplifier and Linearizer Units," Ordnance Research Laboratory, The Pennsylvania State University, 1964.

4. Schlichting, H., Boundary Layer Theory, McGraw-Hill Book Company, New York, 1960.

5. Willmarth, W. W., and Woolridge, C. E., "Measurements of the Correlation Between the Fluctuating Velocities and the Fluctuating Wall Pressure in a Thick Turbulent Boundary Layer," University of Michigan, 1962.

6. Willmarth, W. W., and Woolridge, C. E., "Measurements of the Fluctuating Pressure at the Wall Beneath a Thick Turbulent Boundary Layer," University of Michigan, 1962.

7. Silverstein, A., Katzoff, S., and Bullivant, W. K., "Downwash And Wake Behind Plain and Flapped Airfoils," NACA Report No. 651, 1939.

8. Douglas Aircraft Report No. ES26988, April 25, 1958.

9. Hoerner, S. F., Fluid Dynamic Drag, Dr. S. F. Hoerner, Midland Park, N. J., 1958.

10. Milne-Thomson, L. M., Theoretical Hydrodynamics, The Macmillan Company, New York, 1960.

APPENDIX I

A METHOD FOR CONDUCTING REFERENCE CHECKS ON THE ELECTRONIC

EQUIPMENT USED WITH THE HOT-WIRE ANEMOMETER

In theory, a calibration curve of output voltage versus velocity should be a straight line. However, after a period of time, due to the characteristics of the electronic equipment, this straight-line calibration curve could change. The following method allowed the hot-wire output to be checked relative to that of a pitot probe.

In a wind-tunnel facility, other than that being used for testing, a cylinder was mounted normal to the flow and the hot-wire and pitot probes were positioned behind it. The pitot probe establishes the mean values of the velocity fluctuations at various tunnel speeds by producing a difference in height between two mercury columns. From these pressure readings a curve was drawn to obtain mean velocity versus tunnel speed, which shows the response to the turbulence generator (cylinder). The hot-wire probe was placed in relatively the same position, and its response was recorded. Once the mean values of the velocity were established with the pitot probe, any necessary changes were made on the basis of this comparison to insure the proper response of the hot-wire probe.

Once it had been established that this hot-wire probe and its

accompanying electronic equipment were functioning properly, the probe was then switched to the electronics for the other probe. The response of the reference probe in the other channel was observed and necessary changes made on this channel to insure its correct operation.

By means of this checking procedure, the hot-wire anemometer was then used to obtain quantitative results of mean velocity fluctuations and root-mean-square values of the turbulence level.

APPENDIX II


RESULTS OF CALCULATIONS FROM THE BOUNDARY-LAYER EQUATIONS

OF VON KÁRMÁN AND POHLHAUSEN, AND TRUCKENBRODT


By the method outlined in Chapter IV, the necessary

quantities associated with the laminar portion of the boundary layer

were obtained. On the basis of Fig. 31, the transition point was

obtained satisfying equation 15. (These computations were made for

the body without fins or propeller.) Table 2-I presents the

approximation to the body found for the laminar displacement

thickness and associated quantities. These computations were

obtained with the aid of an IBM 1620 digital computer. As seen

from Fig. 31, the transition point occurs for $S = 0.1245$, which

corresponds to $X/\ell = 0.111$.

The associated quantities necessary for the remaining

computations are now found as functions of the transition point:

$$R_{\delta^*} = R_{crit} = 1290 \text{ (from Fig. 31)}$$

$$C_f = 0.0033184 \text{ (for equation 2)}$$

$$C_{f\ell} = 0.00170 \text{ (for equation 3)}$$

$$\bar{u}/u_\infty = 1.034 \text{ (from Fig. 28)}$$

$$H_1 = H - \Delta H = 1.322 \text{ (from } \delta^*, \vartheta, \text{ equation 14, and Reference 4)}$$

$$L_1 = 0.0805 \text{ (from Fig. 29)}$$

$$C_1^* = 0.1485 \times 10^{-5} \text{ (from equation 3)}$$

$$\xi_1 = (C_1^*)^m = 0.4863 \times 10^{-23} \text{ (from equation 5)}$$

TABLE 2-I

APPROXIMATION TO ORIGINAL BODY BY LAMINAR DISPLACEMENT
THICKNESS FROM THE NOSE TO TRANSITION

(All dimensions are normalized with respect to the body length.)

| x | $y_O$ | $y_F$ | $\delta^*$ | $\vartheta$ | $H=\delta^*/\vartheta$ |
|---|---|---|---|---|---|
| 0.00000 | 0.00000 | 0.00000 | 0.00000 | 0.000000 | 0.000 |
| .00645 | .00949 | .00953 | .00004 | .000019 | 2.100 |
| .02086 | .02324 | .02331 | .00070 | .000035 | 2.000 |
| .03674 | .03043 | .03054 | .00011 | .000055 | 2.000 |
| .05263 | .03550 | .03564 | .00014 | .000069 | 2.000 |
| .06852 | .03935 | .03952 | .00017 | .000085 | 2.000 |
| .08425 | .04250 | .04270 | .00020 | .000100 | 2.000 |
| .10014 | .04525 | .04547 | .00022 | .000125 | 1.760 |
| .11100 | .04668 | .04693 | .00025 | .000193 | 1.322 |

Note: The last value in each column is for the condition of
transition.

The constants associated with equations 13 and 14, which are necessary for the calculation of the shape factors $K$ and $\Lambda$, are given as (4):

$$a = \frac{37}{315} \, , \qquad b = \frac{1}{945} \, , \qquad c = \frac{1}{9072} \, ;$$

and

$$d = \frac{3}{10} \, , \qquad e = \frac{-1}{120} \, .$$

At transition, $K$ and $\Lambda$ were found to be 0.016 and 1.2, respectively.

Once these values at transition had been established, it was a relatively straightforward procedure to account for the turbulent portion of the body. The use of equations 2 through 8 (section IV) gave successive approximations for the displacement thickness.

Table 2-II and Figs. 2-1a and 2-1b show these approximations for the displacement thickness and associated quantities. As before, all quantities have been nondimensionalized as those in Table 2-I, with $y_n$ being the $n^{th}$ approximation, $n = 1,2,3,4$.

In addition to the theoretical predictions for $\delta^*$ and $\vartheta$ directly, these quantities were also found on the basis of boundary-layer profiles at the probe location. In section III C some characteristic results of test measurements are shown: boundary layer profiles are shown, Fig. 20, and $\delta^*$ and $\vartheta$ are defined.

At the probe position $x/\ell = 0.95$, $\delta^*$ and $\vartheta$ were obtained from Fig. 34, without propeller, by a simple integration
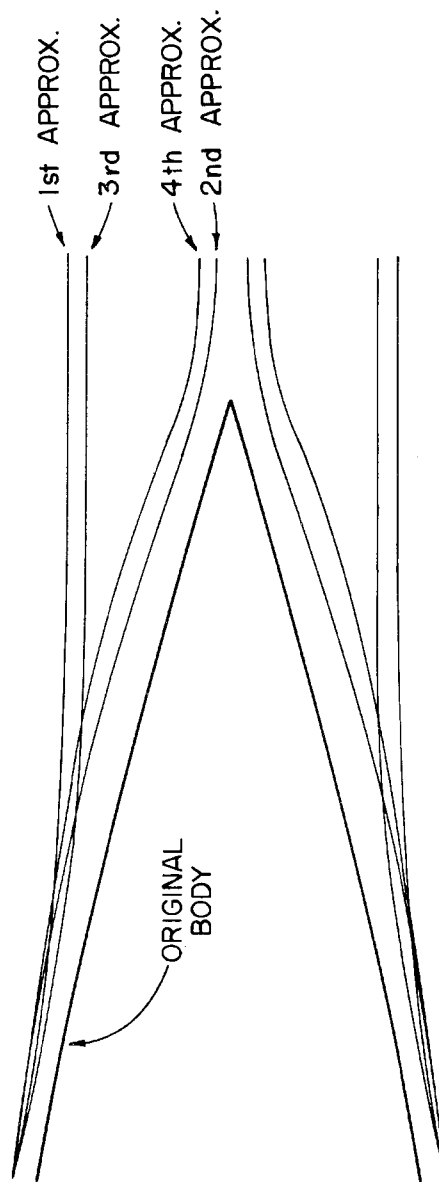
Fig. 2-1a Successive Approximations of Displacement Thickness for the Original Body
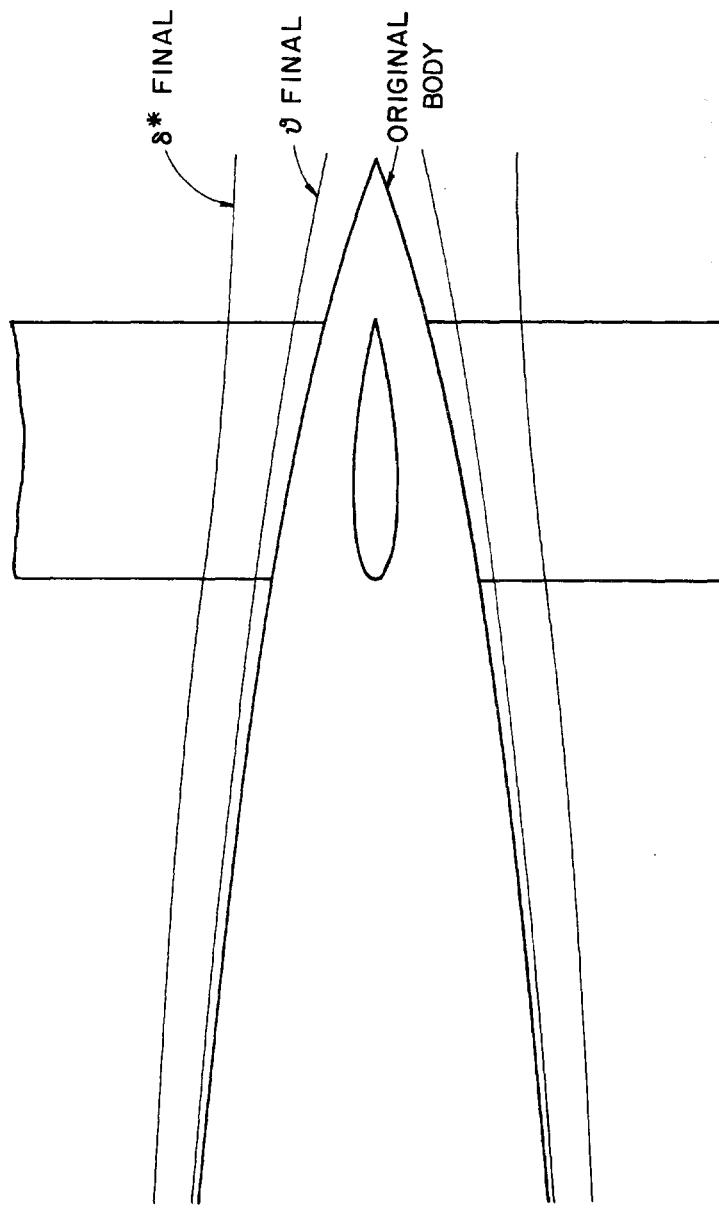
Fig. 2-1b  Final Approximation of Displacement Thickness and Momentum Thickness for the Original Body

of this boundary-layer profile. The integration resulted in

$$\delta^* = 0.00989,$$

$$\vartheta = 0.00551,$$

and H = 1.80.

By interpolating the data from Table 2-II, the predicted values were obtained:

$$\delta^* = 0.00935,$$

$$\vartheta = 0.00505,$$

and H = 1.85.

By employing equation 1 (section IV) with $n = 2/(H-1)$ , a boundary-layer profile is obtained that compares favorably with the measured profile. Figure 2-2 shows this comparison between the measured and predicted boundary layers at the probe position.

Figure 2-3 and 2-4 further illustrate the use of equation 1 for obtaining predicted boundary-layer profiles. These figures are for the flow at a strut leading edge and at the location of the propeller.

Note: The apparent "bulge" in the dotted curve of Fig. 2-2 shows that the flow is starting to reverse itself, which is an indication that the separation point is at hand. This effect is also noticeable in the predicted curve of Fig 2-2, and in Fig. 2-4, which appear as a "shallowness", when compared with Fig. 2-3, which is a "full" boundary-layer profile.

## TABLE 2-II

### APPROXIMATION TO ORIGINAL BODY BY DISPLACEMENT
### THICKNESS FROM TRANSITION TO TAIL

| x | $y_0$ | $y_1$ | $y_2$ | $y_3$ | $y_4$ | $y_F$ | $\delta^*$ | $\theta$ | H |
|---|---|---|---|---|---|---|---|---|---|
| 0.11100 | 0.04668 | 0.04693 | 0.04693 | 0.04693 | 0.04693 | 0.04693 | 0.00025 | 0.000193 | 1.322 |
| .11619 | .04767 | .04795 | .04795 | .04795 | .04795 | .04795 | .00028 | .000201 | 1.390 |
| .13307 | .04993 | .05028 | .05028 | .05028 | .05028 | .05028 | .00035 | .000243 | 1.440 |
| .15211 | .05224 | .05264 | .05264 | .05264 | .05264 | .05264 | .00040 | .000284 | 1.405 |
| .17345 | .05454 | .05500 | .05500 | .05500 | .05500 | .05500 | .00046 | .000325 | 1.415 |
| .19595 | .05669 | .05720 | .05720 | .05720 | .05720 | .05720 | .00051 | .000363 | 1.405 |
| .21779 | .05843 | .05899 | .05899 | .05899 | .05899 | .05899 | .00056 | .000400 | 1.400 |
| .23831 | .05974 | .06035 | .06035 | .06035 | .06035 | .06035 | .00061 | .000435 | 1.400 |
| .25917 | .06076 | .06143 | .06142 | .06142 | .06142 | .06142 | .00066 | .000474 | 1.390 |
| .28101 | .06157 | .06230 | .06229 | .06229 | .06229 | .06229 | .00072 | .000515 | 1.400 |
| .30286 | .06215 | .06293 | .06293 | .06293 | .06293 | .06293 | .00078 | .000556 | 1.405 |
| .32471 | .06255 | .06339 | .06338 | .06338 | .06338 | .06338 | .00083 | .000596 | 1.390 |
| .34656 | .06276 | .06365 | .06365 | .06365 | .06365 | .06365 | .00089 | .000638 | 1.390 |
| .36841 | .06284 | .06379 | .06378 | .06378 | .06378 | .06378 | .00094 | .000679 | 1.385 |
| .38993 | .06279 | .06379 | .06379 | .06379 | .06379 | .06379 | .00100 | .000718 | 1.390 |

TABLE 2-II (continued)

| x | $y_0$ | $y_1$ | $y_2$ | $y_3$ | $y_4$ | $y_F$ | $\sigma^*$ | $\Theta$ | H |
|---|---|---|---|---|---|---|---|---|---|
| 0.41112 | 0.06260 | 0.06367 | 0.06366 | 0.06366 | 0.06366 | 0.06366 | 0.00106 | 0.000758 | 1.400 |
| .43263 | .06229 | .06341 | .06341 | .06341 | .06341 | .06341 | .00112 | .000800 | 1.400 |
| .45448 | .06186 | .06304 | .06303 | .06303 | .06303 | .06303 | .00117 | .000844 | 1.385 |
| .47534 | .06134 | .06258 | .06258 | .06257 | .06258 | .06258 | .00124 | .000886 | 1.400 |
| .49321 | .06085 | .06214 | .06212 | .06212 | .06212 | .06212 | .00127 | .000924 | 1.375 |
| .50910 | .06035 | .06168 | .06167 | .06166 | .06167 | .06167 | .00132 | .000954 | 1.385 |
| .52830 | .05967 | .06106 | .06104 | .06104 | .06104 | .06105 | .00138 | .000994 | 1.390 |
| .55082 | .05878 | .06023 | .06022 | .06021 | .06022 | .06022 | .00144 | .001040 | 1.385 |
| .57333 | .05778 | .05931 | .05929 | .05929 | .05929 | .05929 | .00151 | .001100 | 1.375 |
| .59585 | .05669 | .05828 | .05827 | .05826 | .05826 | .05827 | .00158 | .001150 | 1.375 |
| .61771 | .05549 | .05716 | .05713 | .05713 | .05713 | .05714 | .00165 | .001200 | 1.375 |
| .63757 | .05431 | .05606 | .05604 | .05603 | .05604 | .05604 | .00173 | .001250 | 1.385 |
| .65727 | .05305 | .05486 | .05484 | .05484 | .05484 | .05485 | .00180 | .001310 | 1.375 |
| .67928 | .05150 | .05341 | .05339 | .05338 | .05339 | .05339 | .00189 | .001380 | 1.370 |
| .70244 | .04969 | .05173 | .05168 | .05168 | .05169 | .05170 | .00201 | .001460 | 1.375 |
| .72479 | .04779 | .04995 | .04992 | .04989 | .04992 | .04992 | .00213 | .001540 | 1.385 |
| .74547 | .04589 | .04818 | .04812 | .04811 | .04812 | .04813 | .00224 | .001640 | 1.365 |
| .76534 | .04390 | .04635 | .04629 | .04626 | .04630 | .04630 | .00240 | .001730 | 1.390 |
| .78520 | .04177 | .04437 | .04430 | .04428 | .04430 | .04431 | .00254 | .001850 | 1.370 |
| .80374 | .03964 | .04243 | .04237 | .04235 | .04233 | .04237 | .00273 | .001950 | 1.400 |

TABLE 2-II (continued)

| x | $y_0$ | $y_1$ | $y_2$ | $y_3$ | $y_4$ | $y_F$ | $\delta^*$ | $\theta$ | H |
|---|---|---|---|---|---|---|---|---|---|
| 0.82095 | 0.03749 | 0.04051 | 0.04036 | 0.04034 | 0.04039 | 0.04040 | 0.00291 | 0.002100 | 1.385 |
| .83816 | .03520 | .03845 | .03835 | .03831 | .03828 | .03835 | .00315 | .002230 | 1.410 |
| .85537 | .03273 | .03629 | .03611 | .03602 | .03616 | .03615 | .00342 | .002420 | 1.410 |
| .87257 | .03004 | .03401 | .03384 | .03380 | .03357 | .03381 | .00377 | .002630 | 1.435 |
| .88978 | .02710 | .03163 | .03130 | .03086 | .03168 | .03137 | .00427 | .002900 | 1.475 |
| .90533 | .02422 | .02941 | .02920 | .02857 | .02910 | .02907 | .00485 | .003120 | 1.555 |
| .92023 | .02115 | .02741 | .02677 | .02522 | .02750 | .02650 | .00535 | .003770 | 1.420 |
| .93612 | .01754 | .02564 | .02423 | .02373 | .02500 | .02420 | .00666 | .003970 | 1.675 |
| .95213 | .01363 | .02495 | .01997 | .02236 | .02250 | .02180 | .00817 | .004520 | 1.805 |
| .96868 | .00927 | .02495 | .01476 | .02201 | .01778 | .01910 | .00983 | .005280 | 1.860 |
| .98858 | .00348 | .02495 | .00857 | .02201 | .01162 | .01590 | .01242 | .006670 | 1.860 |
| 1.00000 | .00000 | .02495 | .00505 | .02201 | .00750 | .01350 | .01350 | .008700 | 1.550 |
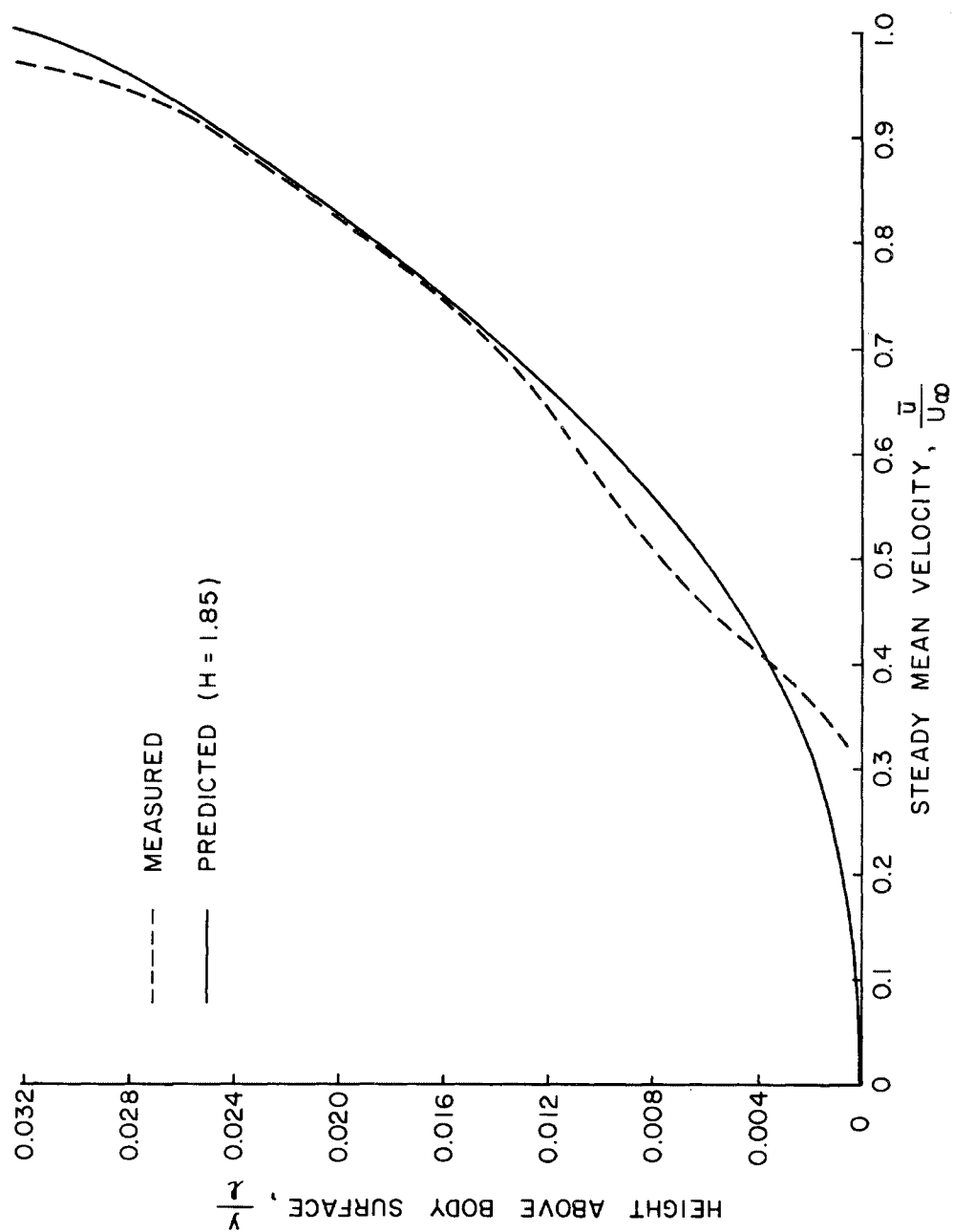
Fig. 2-2 Comparison of Boundary-Layer Profiles at the Probe
        Position
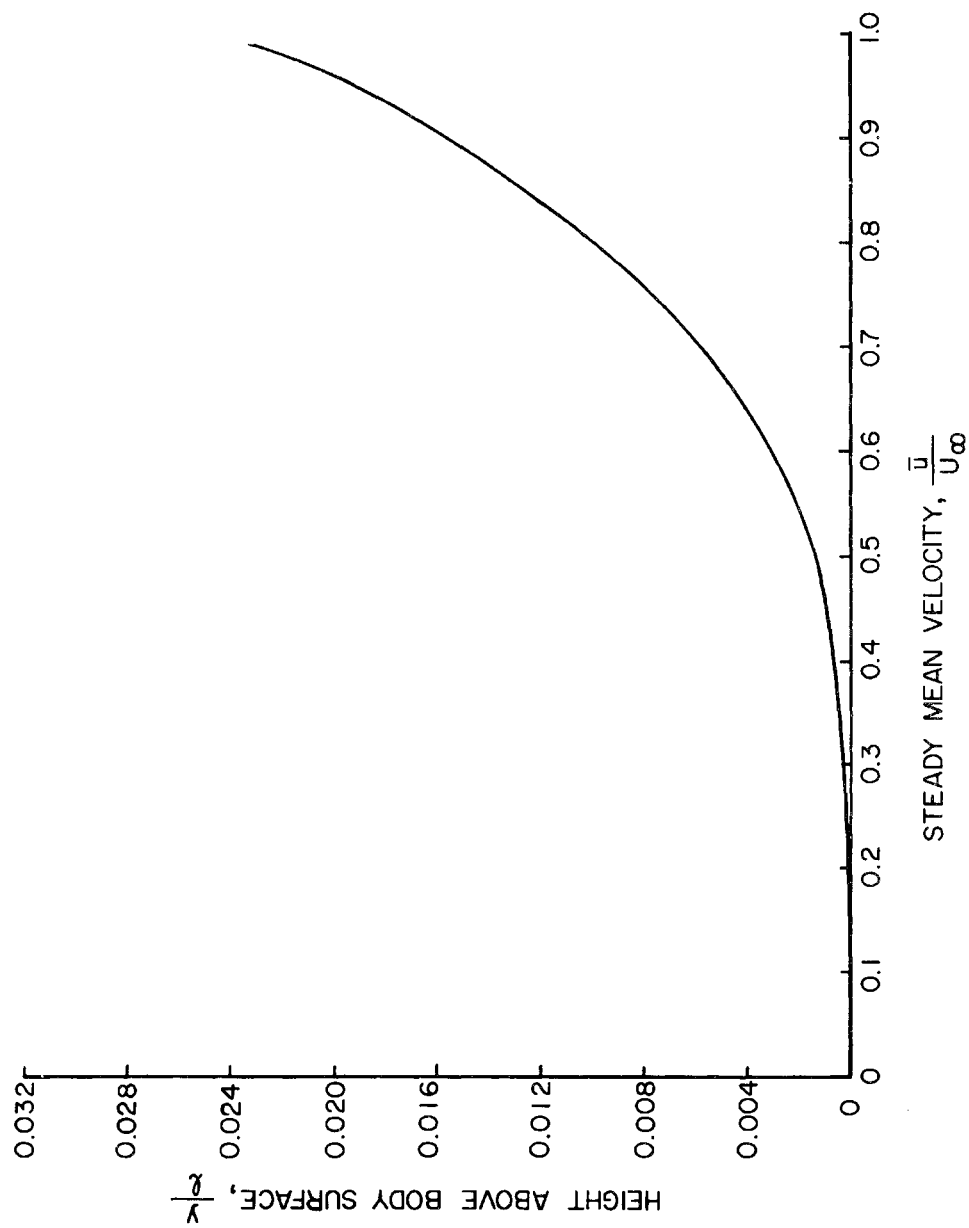
Fig. 2-3  Predicted Boundary-Layer Profile at Strut Leading Edge
(From Equation 1)

STEADY MEAN VELOCITY, $\dfrac{\bar{u}}{U_\infty}$

HEIGHT ABOVE BODY SURFACE, $\dfrac{y}{l}$
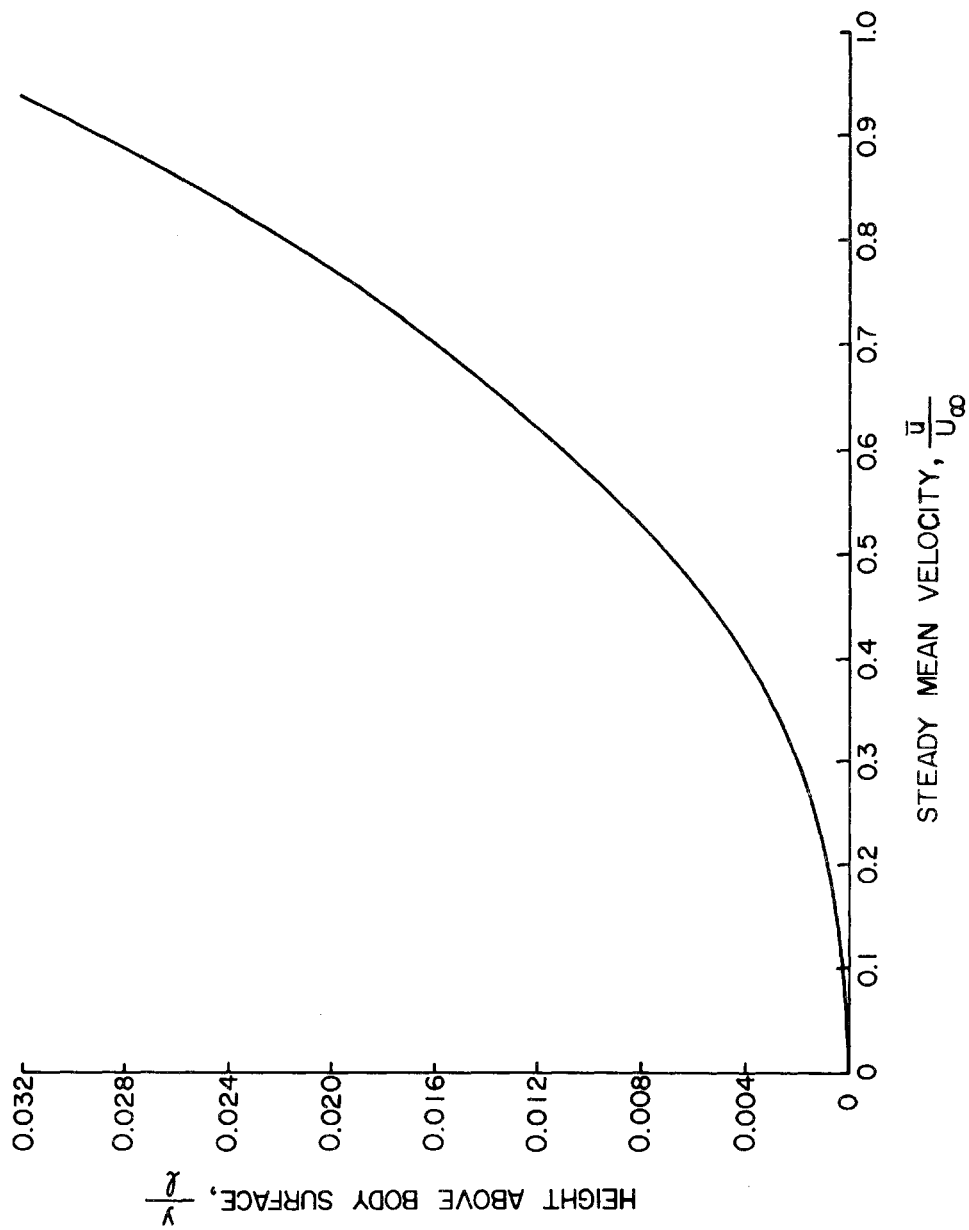
Fig. 2-4  Predicted Boundary-Layer Profile at Propeller Position
(From Equation 1)

APPENDIX III

GRAPHICAL PRESENTATION OF THE EXPERIMENTAL

MEASUREMENTS MADE IN THE BOUNDARY LAYER

The complete results of the hot-wire measurements are
presented in Figs. 3-1 through 3-9. These results include the mean
velocity and rms velocity distribution as a function of
circumferential angle of traverse $\Theta$. Each graph is for a different
value of $r/D$ for the test conditions of the body and fins both
with and without propeller. Figure 3-1 gives the mean velocity
distribution for all values of $r/D$ on one graph to show the overall
variation with distance from the body. Table II was established on
the basis of the average values of these results.
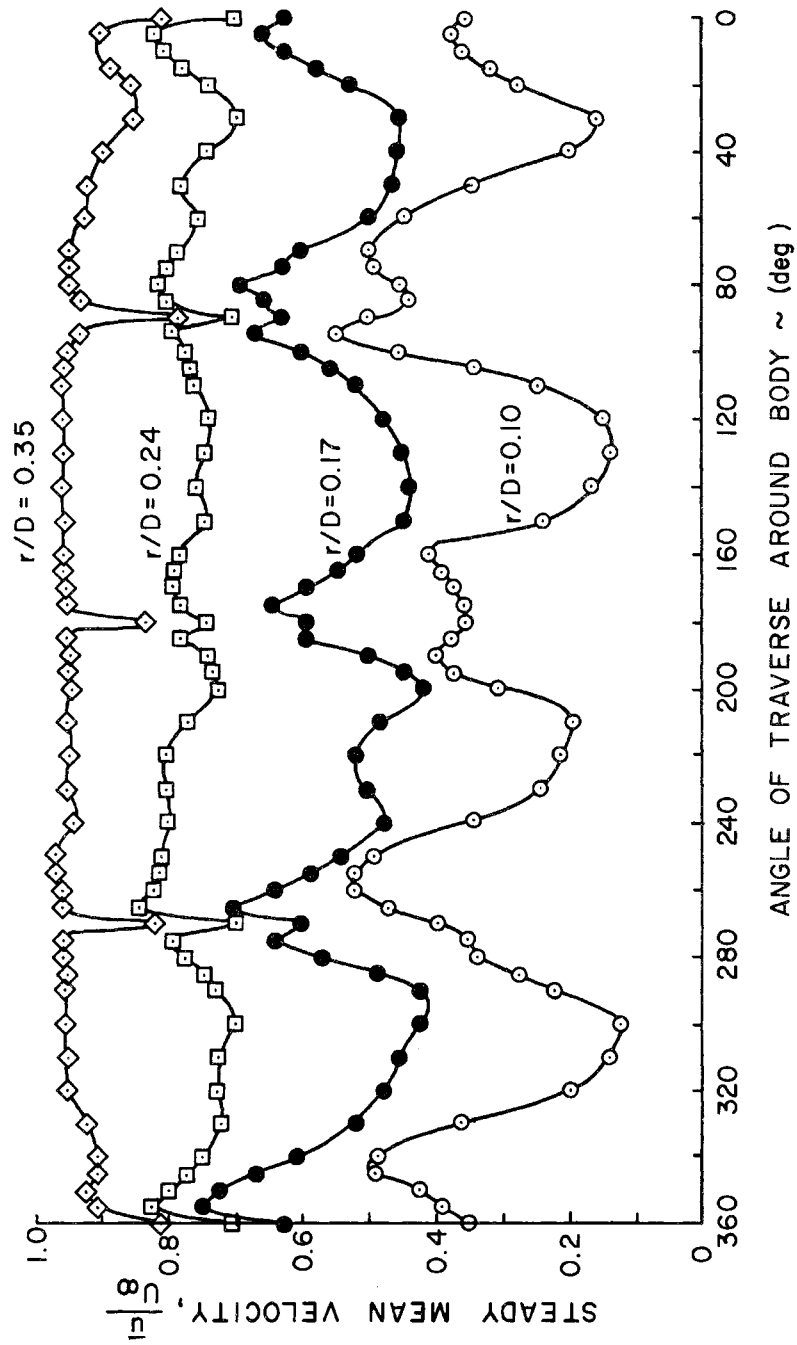
Fig. 3-1  Steady Mean-Velocity Distribution as a Function of
Radial Distance for Body without Propeller
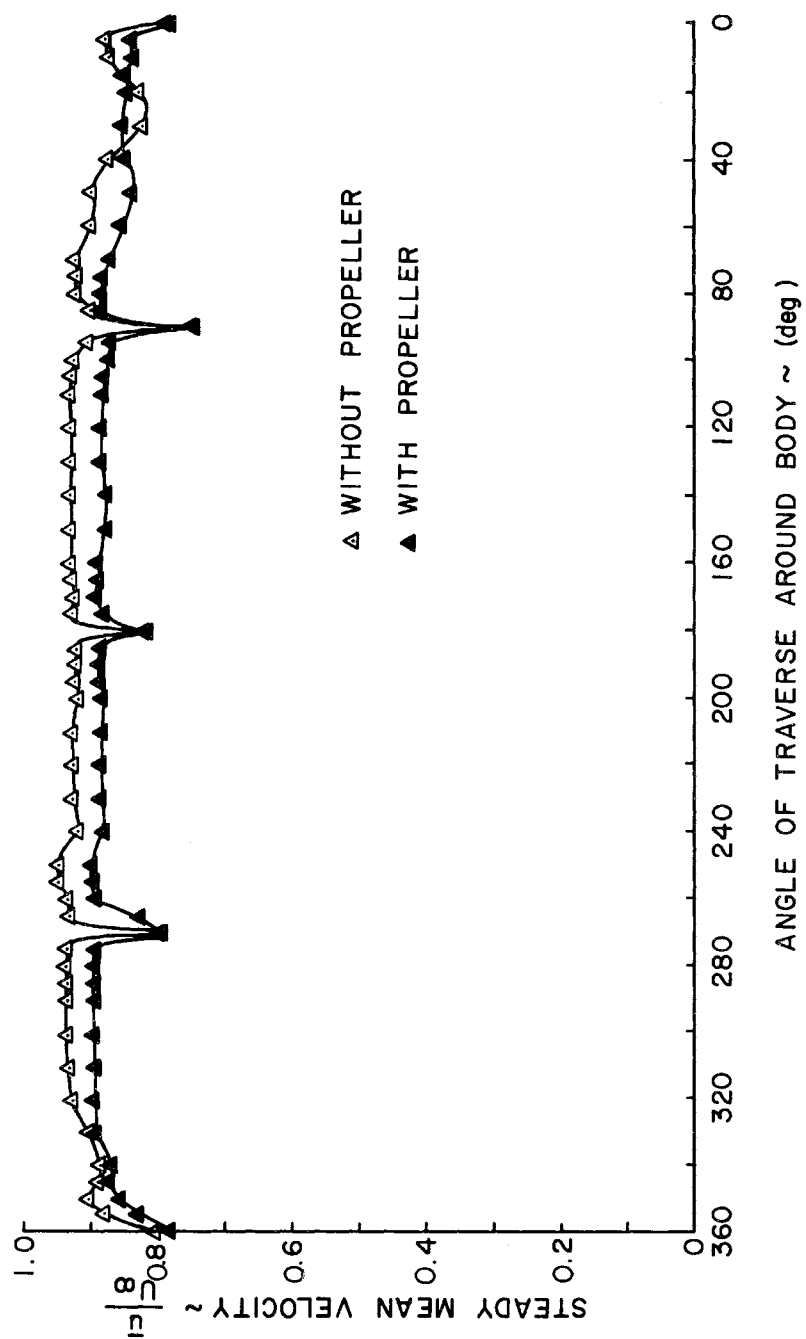
Fig. 3-2 Steady Mean-Velocity Distribution for $r/D = 0.35$
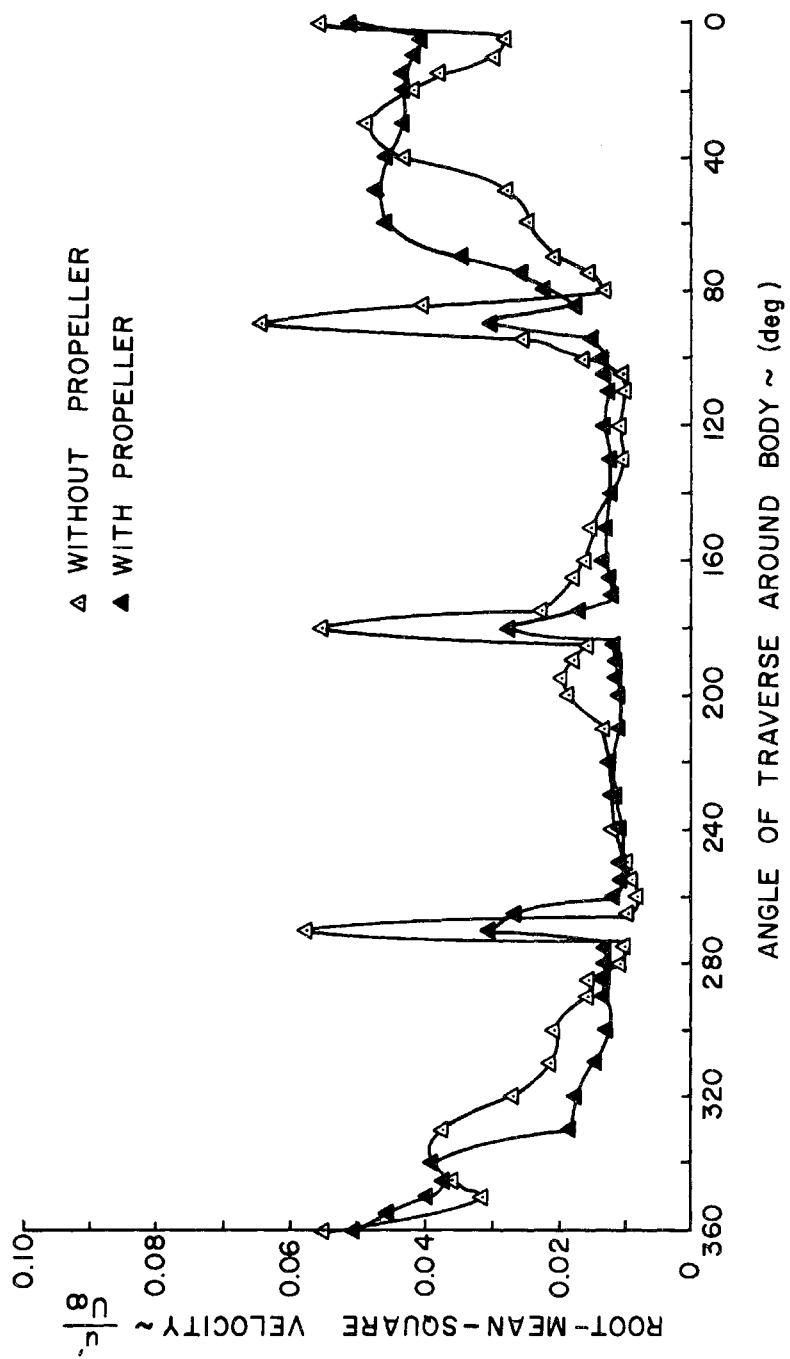
Fig. 3-3  Root-Mean-Square of the Random-Velocity Fluctuations
for r/D = 0.35
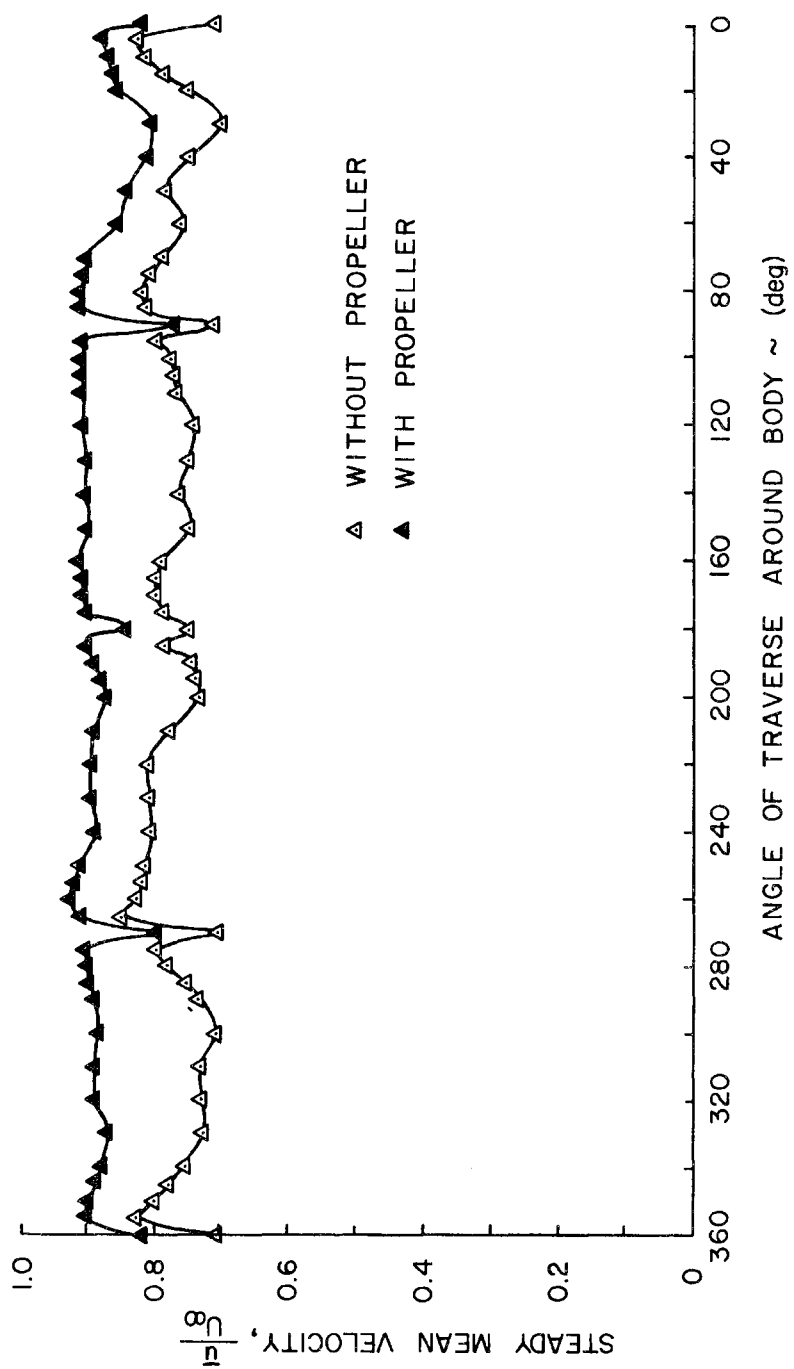
Fig. 3-4  Steady Mean-Velocity Distribution for r/D = 0.24
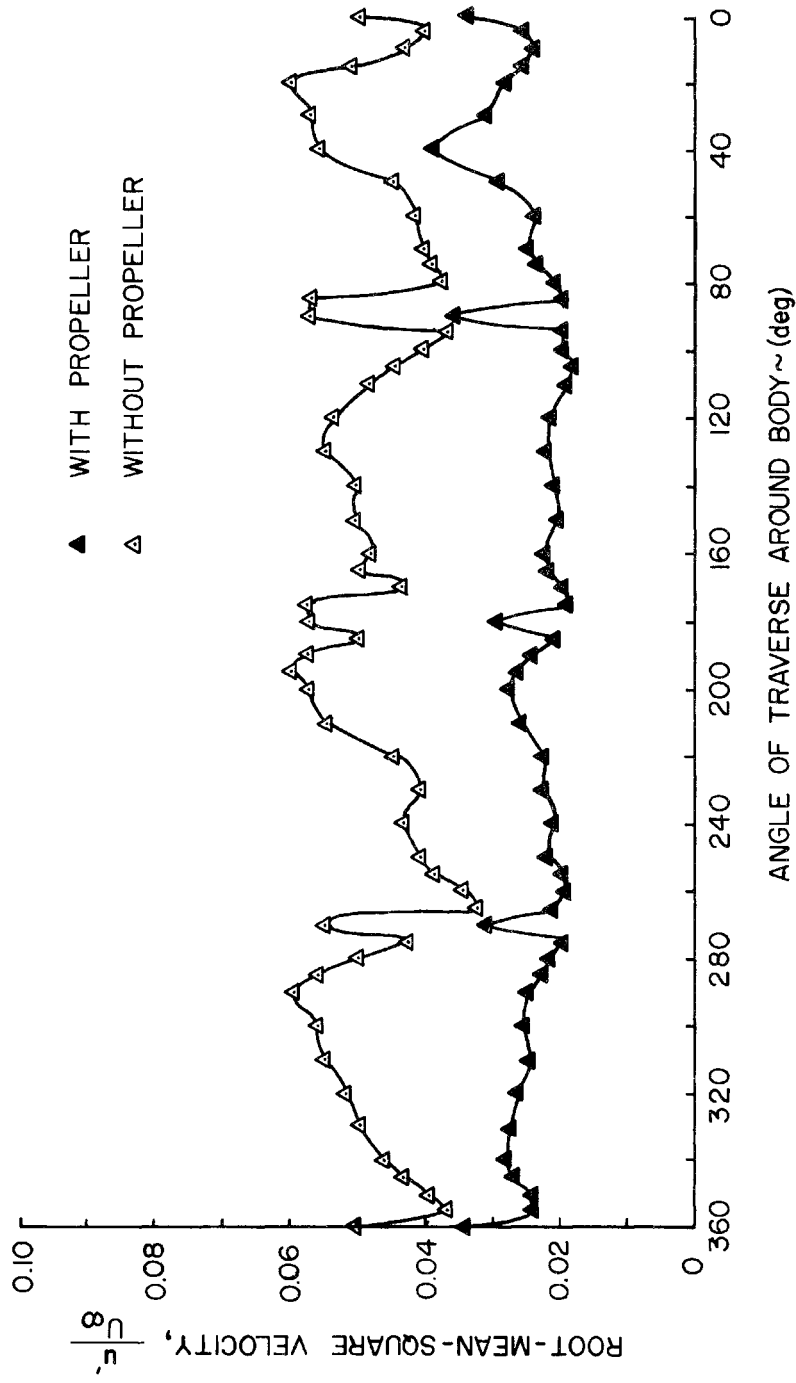
Fig. 3-5  Root-Mean-Square of the Random Velocity Fluctuations
for r/D = 0.24
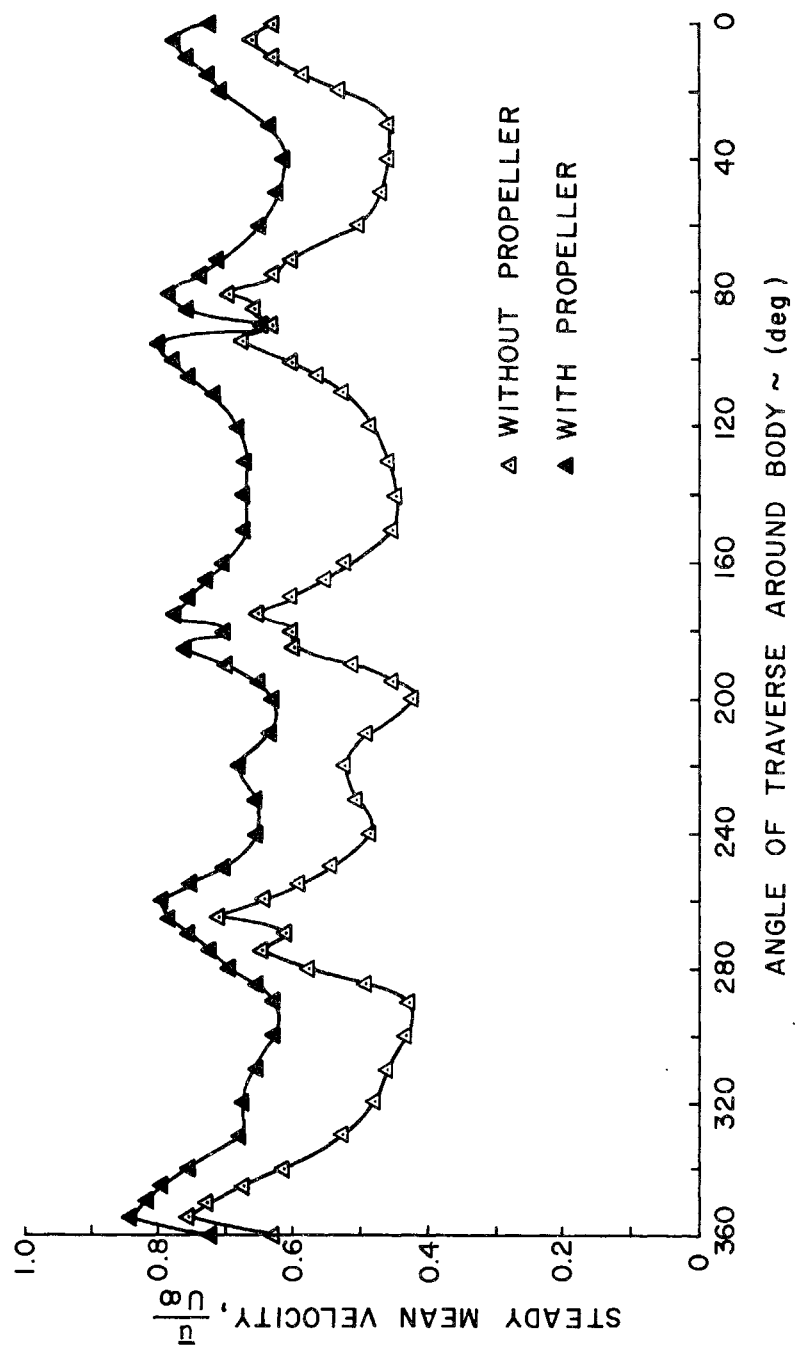
Fig. 3-6 Steady Mean-Velocity Distribution for $r/D = 0.17$
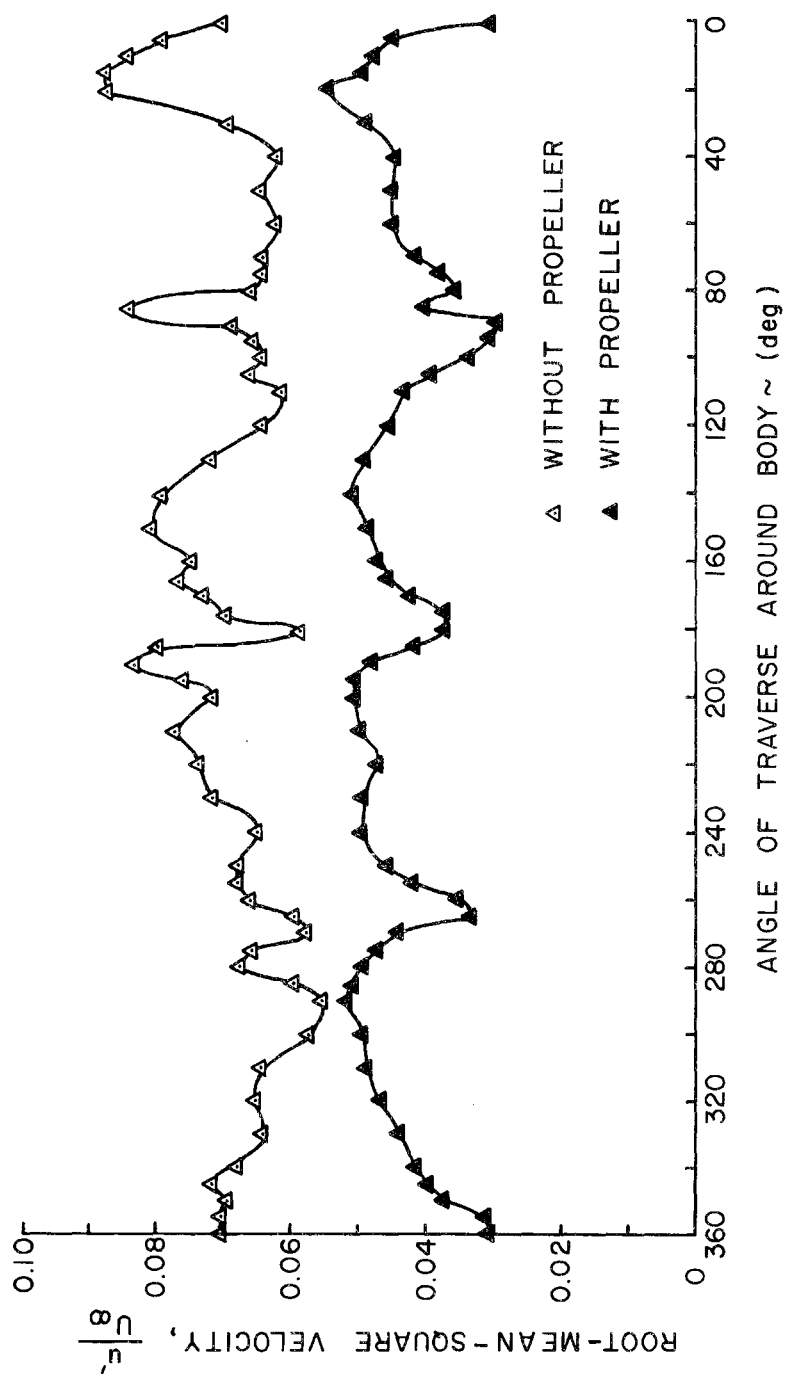
Fig. 3-7 Root-Mean-Square of the Random-Velocity Fluctuations
for r/D = 0.17

99
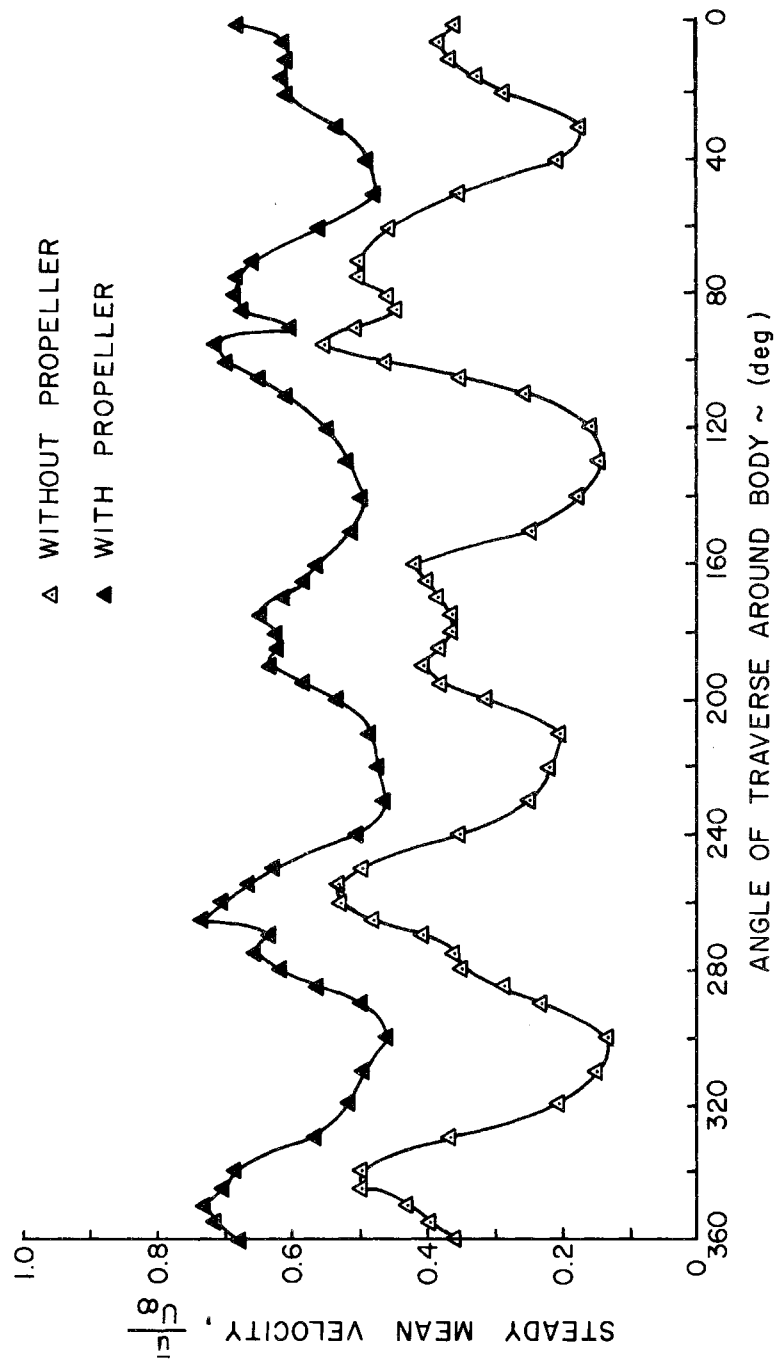


Fig. 3-8 Steady Mean-Velocity Distribution for r/D = 0.10
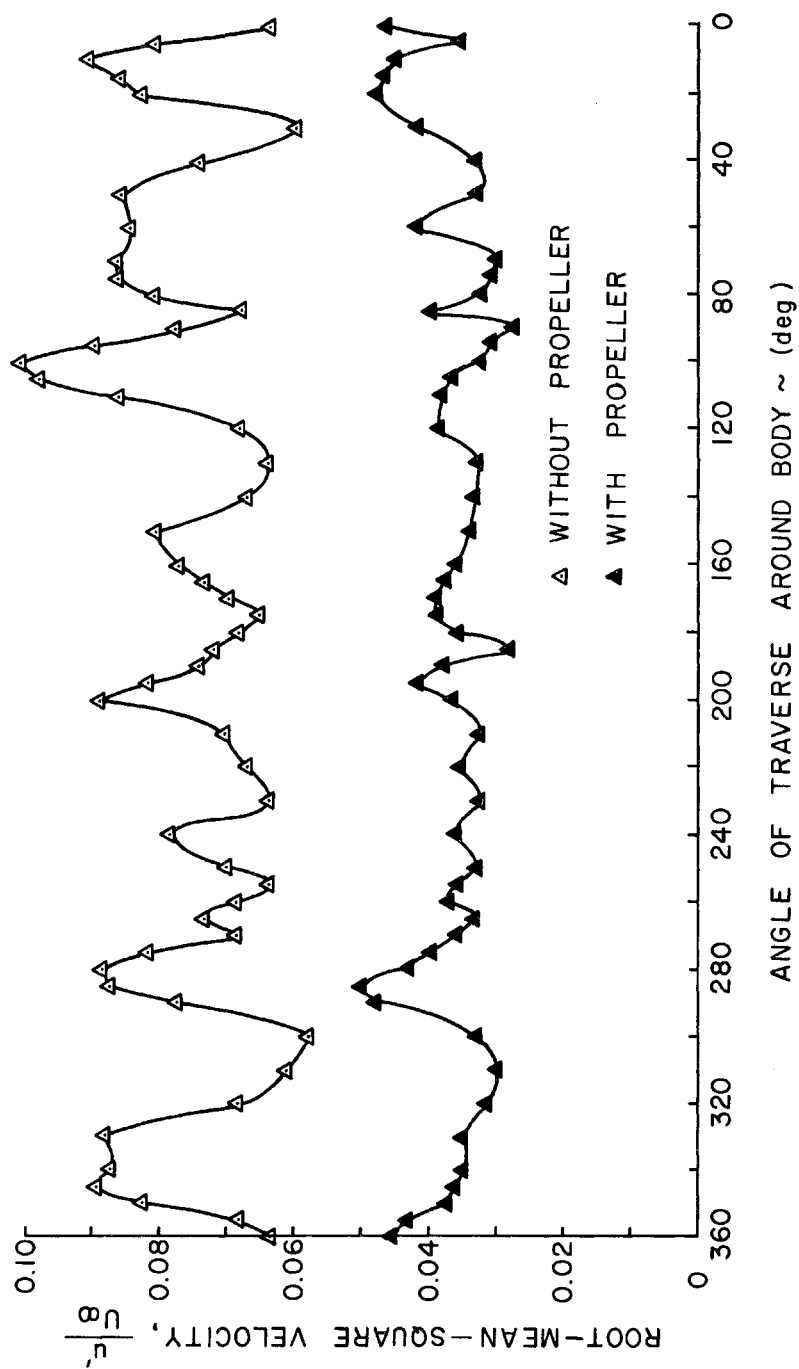
Fig. 3-9  Root-Mean-Square of the Random-Velocity Fluctuations
for r/D = 0.10

The following figures are results of the cross correlations obtained at representative distances of probe separation. These cases are for the body with fins. In Figs. 3-10 and 3-11 the distance between the probes is 0.25 in. Figures 3-12 and 3-13 are for a distance between probes of 5.9 in. These figures represent the extreme cases of probe separation.

In addition to these cross-correlation functions, their associated cross-spectral densities are also shown. As before, these were obtained by performing a Fourier transform of the original functions. The cross-spectral densities are shown in Figs. 3-14 through 3-21.
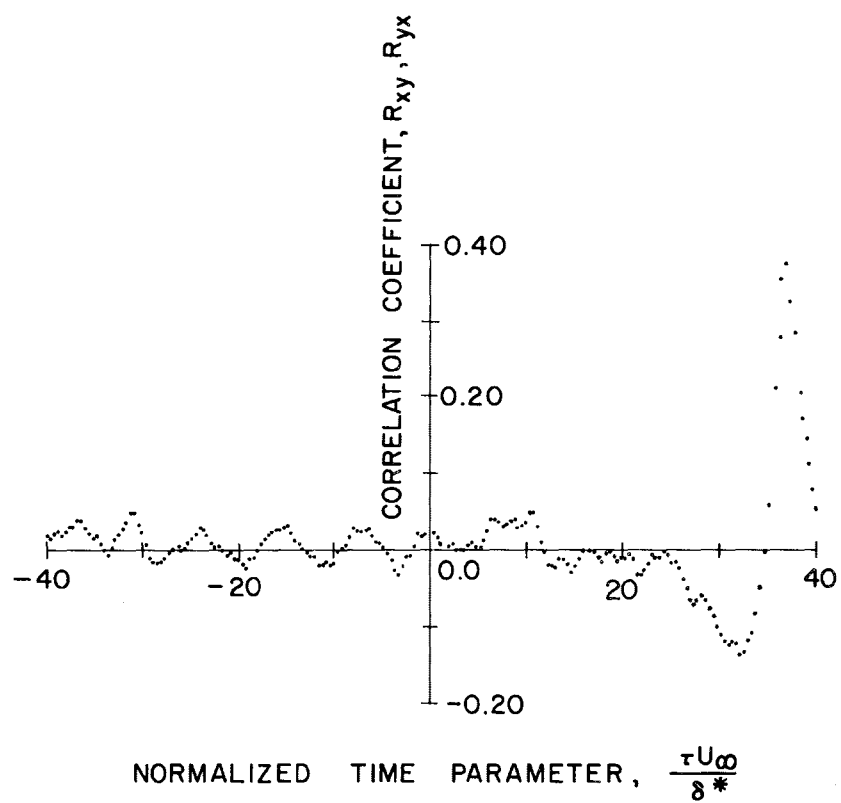
Fig. 3-10 Cross-Correlation Function for Body and Fins with
Propeller for $x_3$ = 0.25 inches
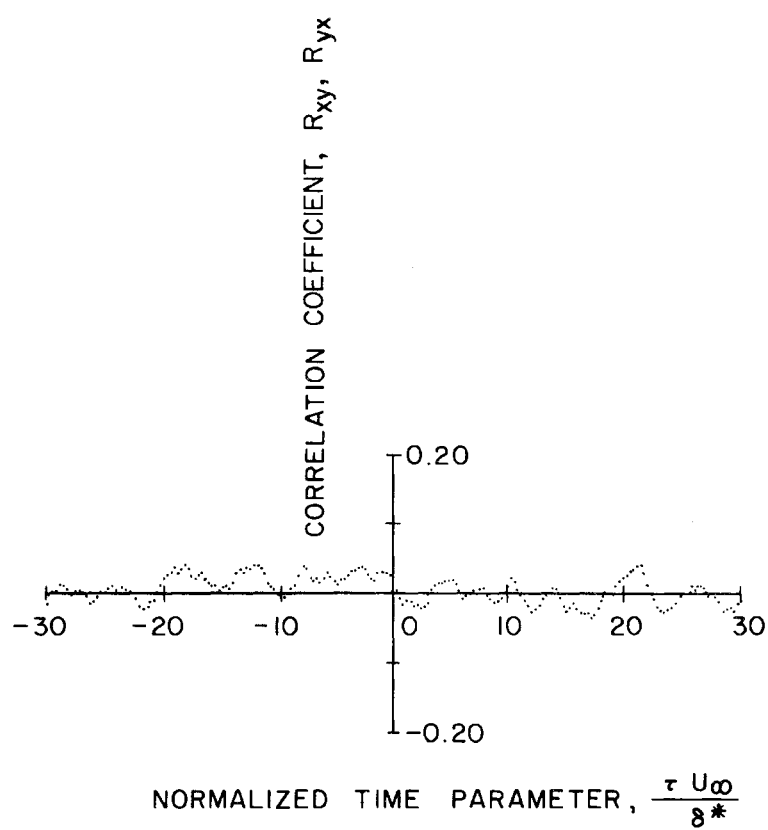
Fig. 3-11  Cross-Correlation Function for Body and Fins without
Propeller for $x_3$ = 0.25 inches
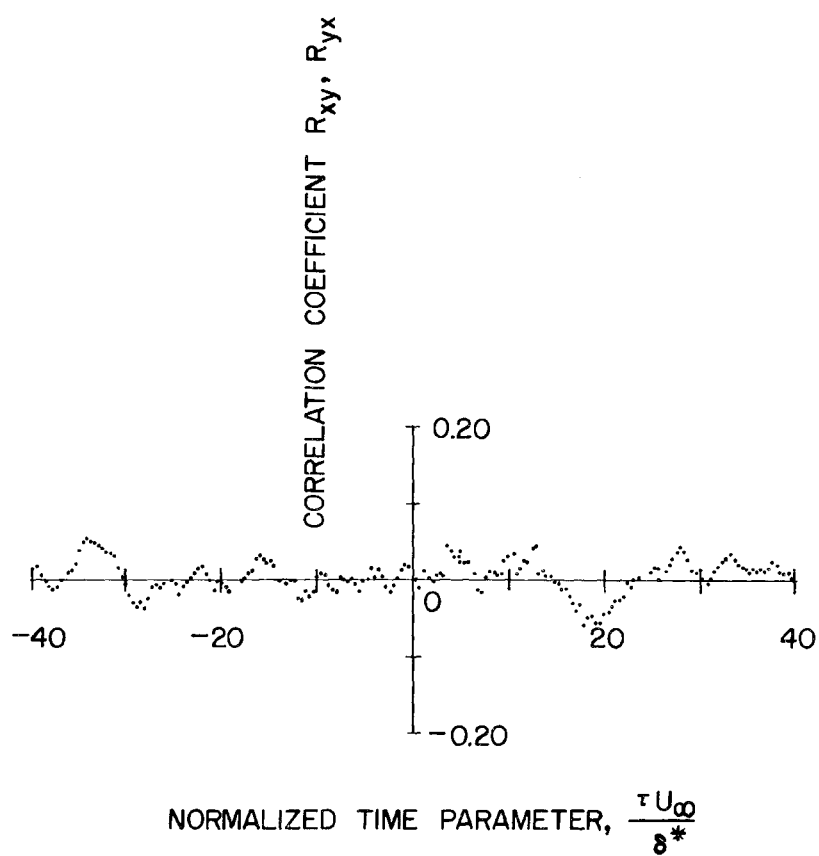
Fig. 3-12  Cross-Correlation Function for Body and Fins with Propeller for $x_3$ = 5.9 inches
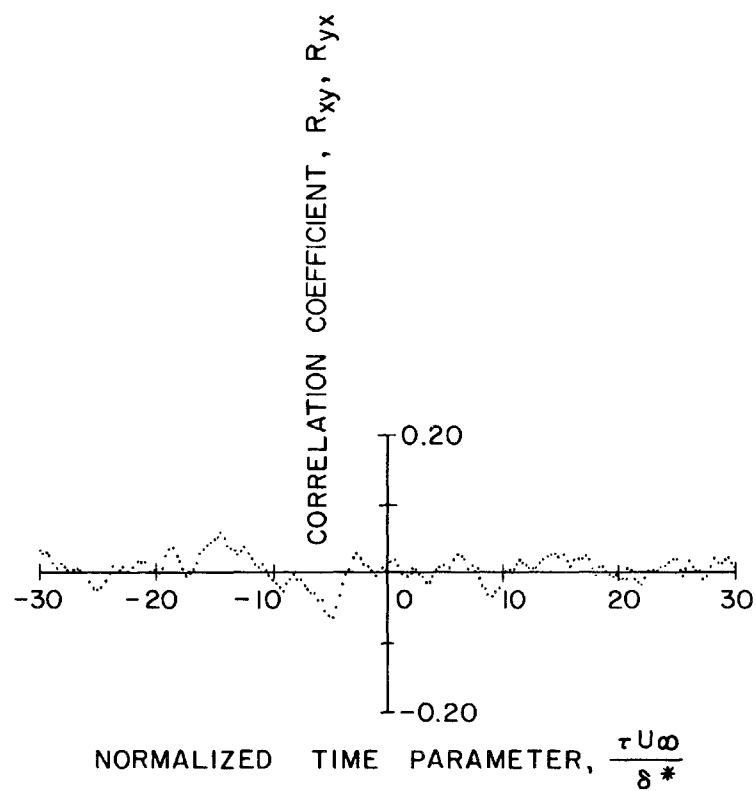
Fig. 3-13  Cross-Correlation Function for Body and Fins without
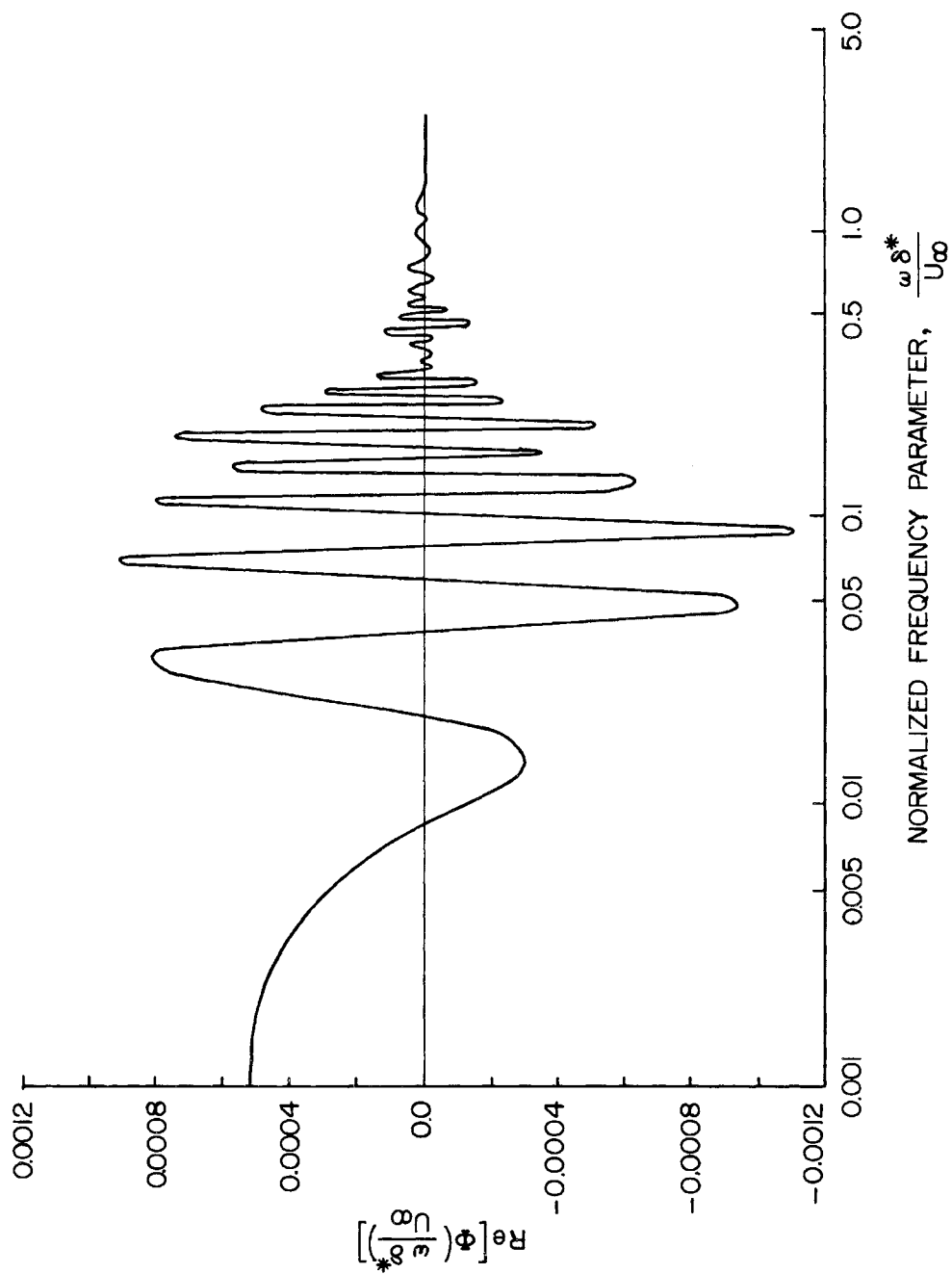Propeller at $x_3$ = 5.9 inches

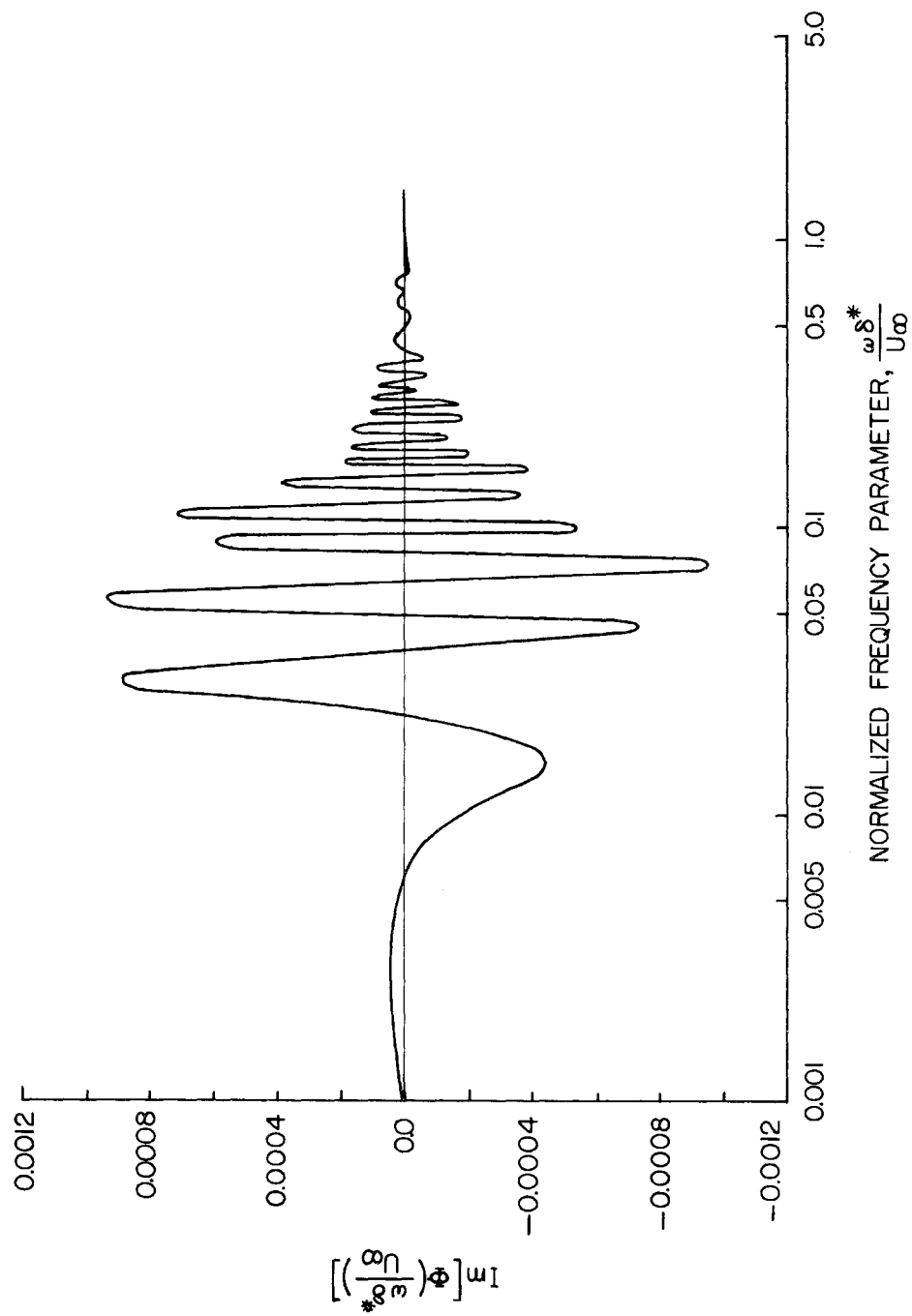Fig. 3-14  Real Part of Cross-Power Spectral Density for Body
and Fins with Propeller for $x_3$ = 0.25 inches

Fig. 3-15  Imaginary Part of Cross-Power Spectral Density for Body and Fins with Propeller for $x_3 = 0.25$ inches
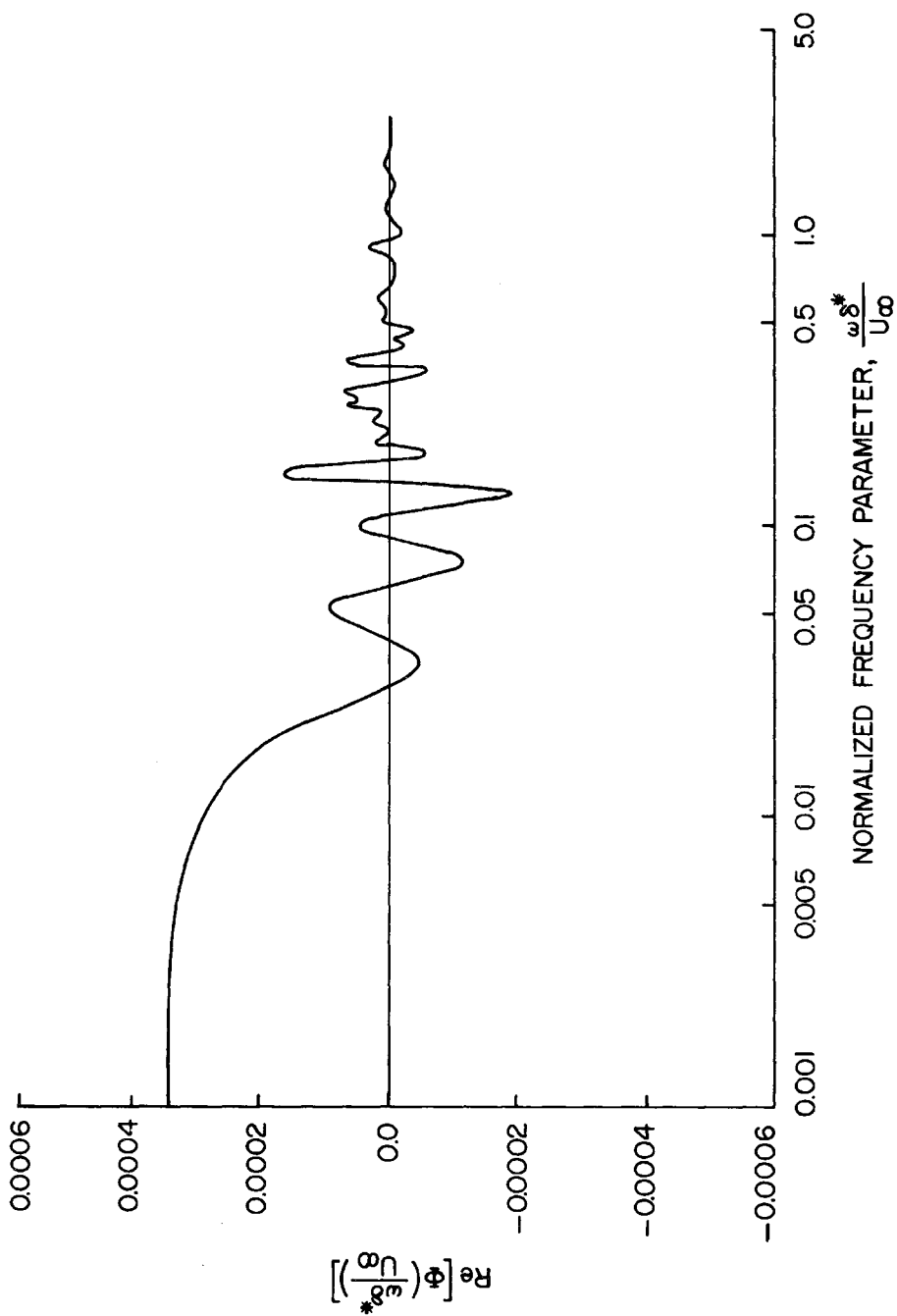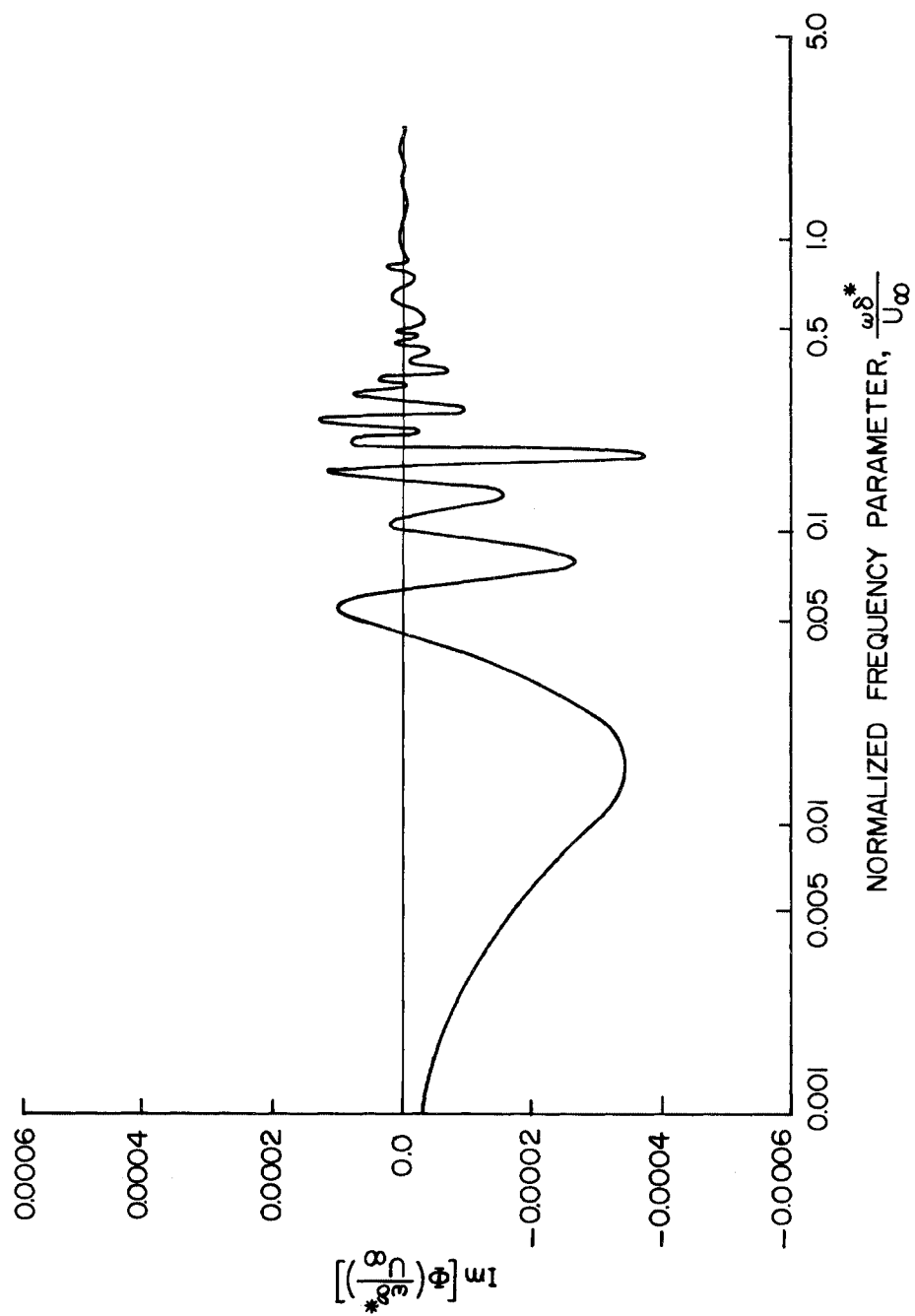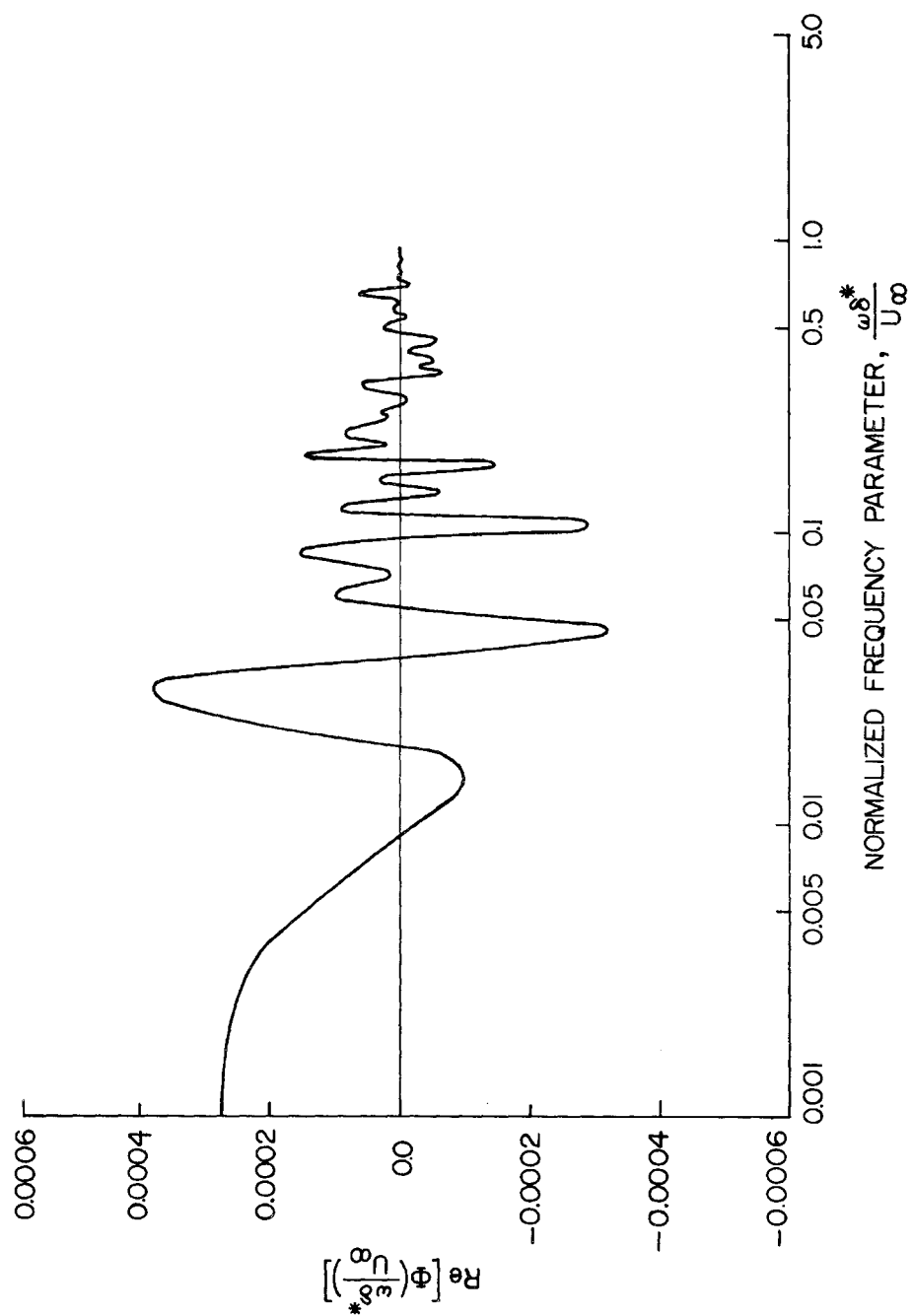
Fig. 3-16  Real Part of Cross-Power Spectral Density for Body and Fins without Propeller for $x_3 = 0.25$ inches

Fig. 3-17  Imaginary Part of Cross-Power Spectral Density for Body and Fins without Propeller for $x_3 = 0.25$ inches

Fig. 3-18 Real Part of Cross-Power Spectral Density for Body and Fins with Propeller for $x_3$ = 5.9 inches
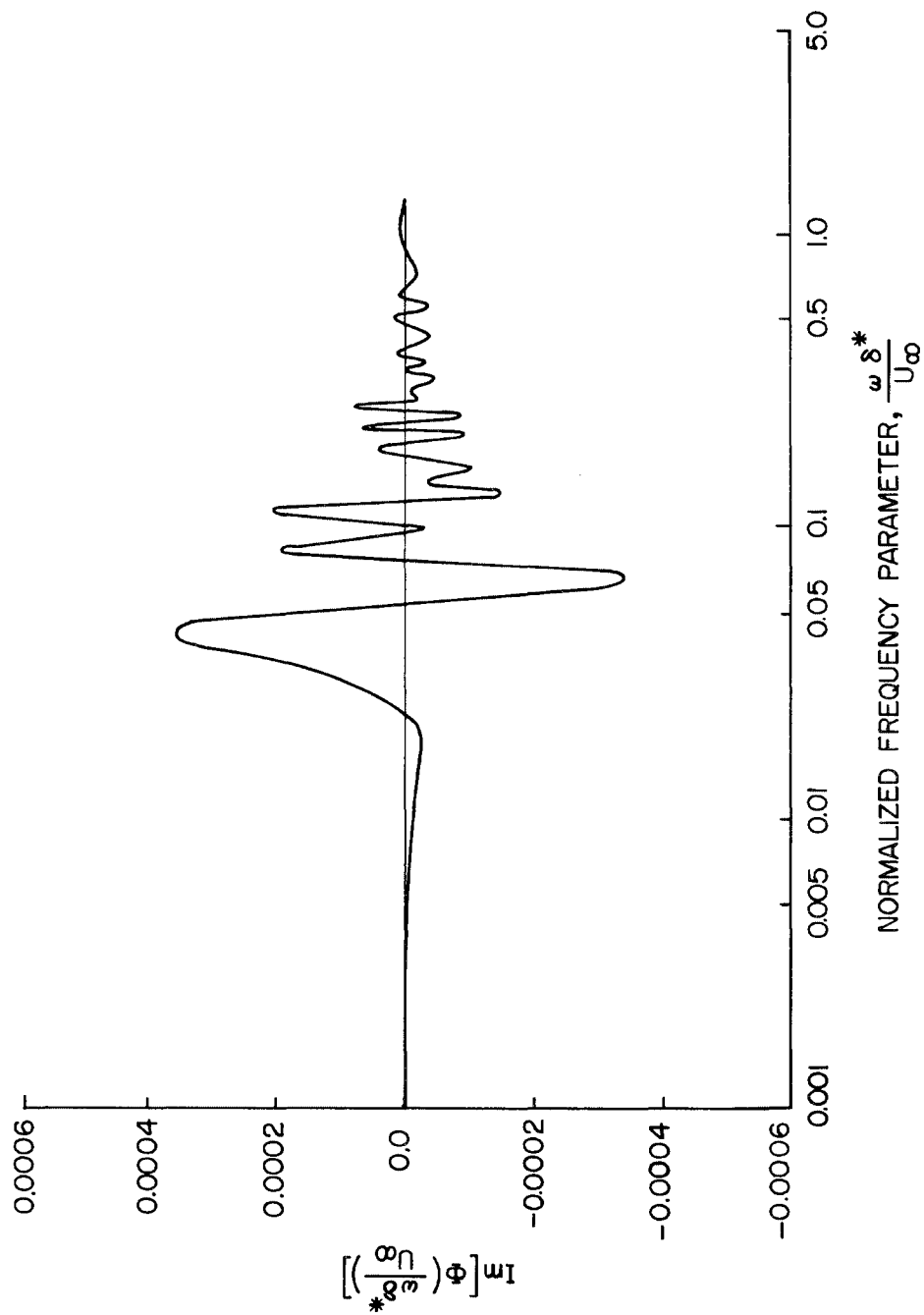
Fig. 3-19   Imaginary Part of Cross-Power Spectral Density for Body
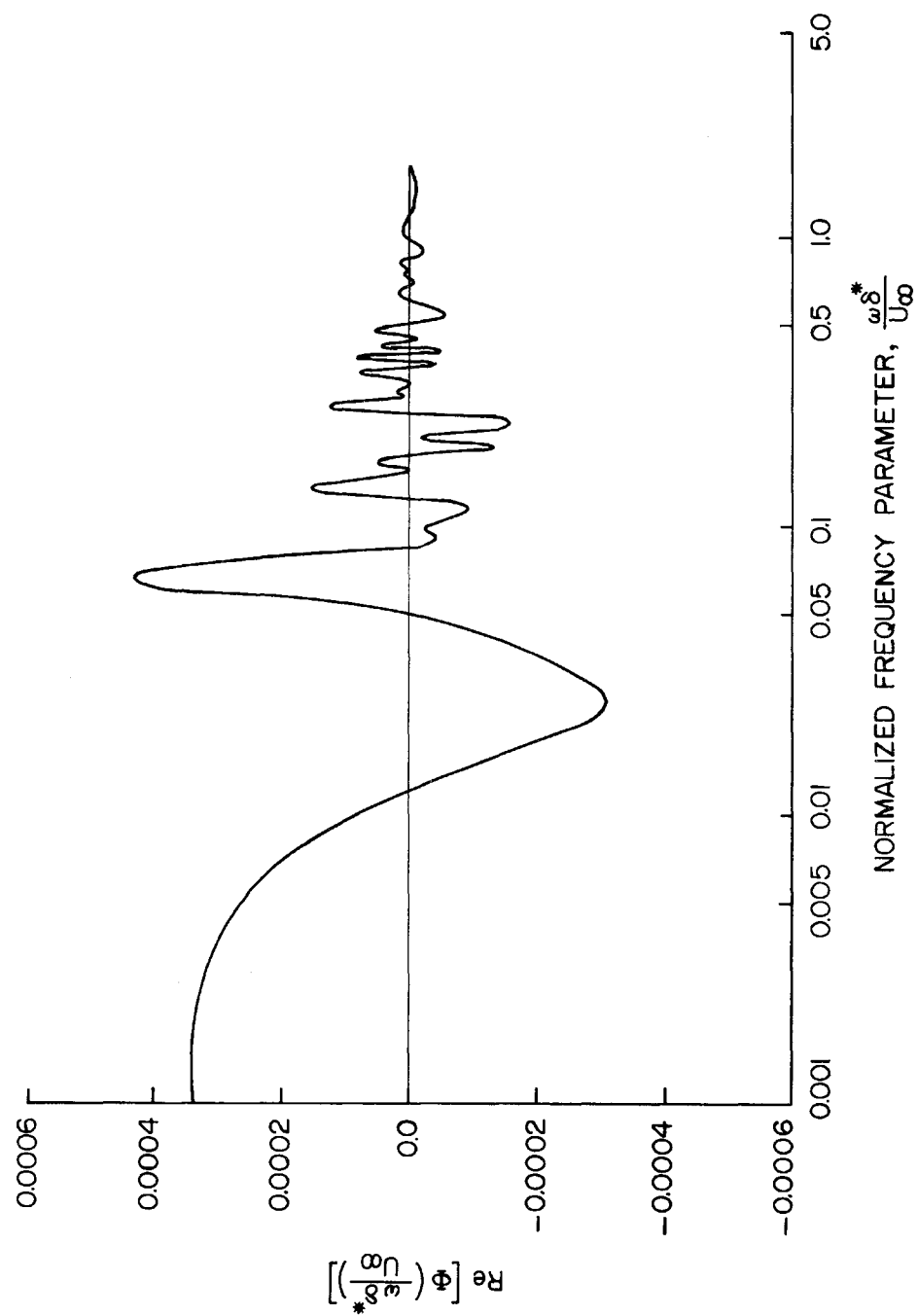and Fins with Propeller for $x_3$ = 5.9 inches

Fig. 3-20   Real Part of Cross-Power Spectral Density for Body and
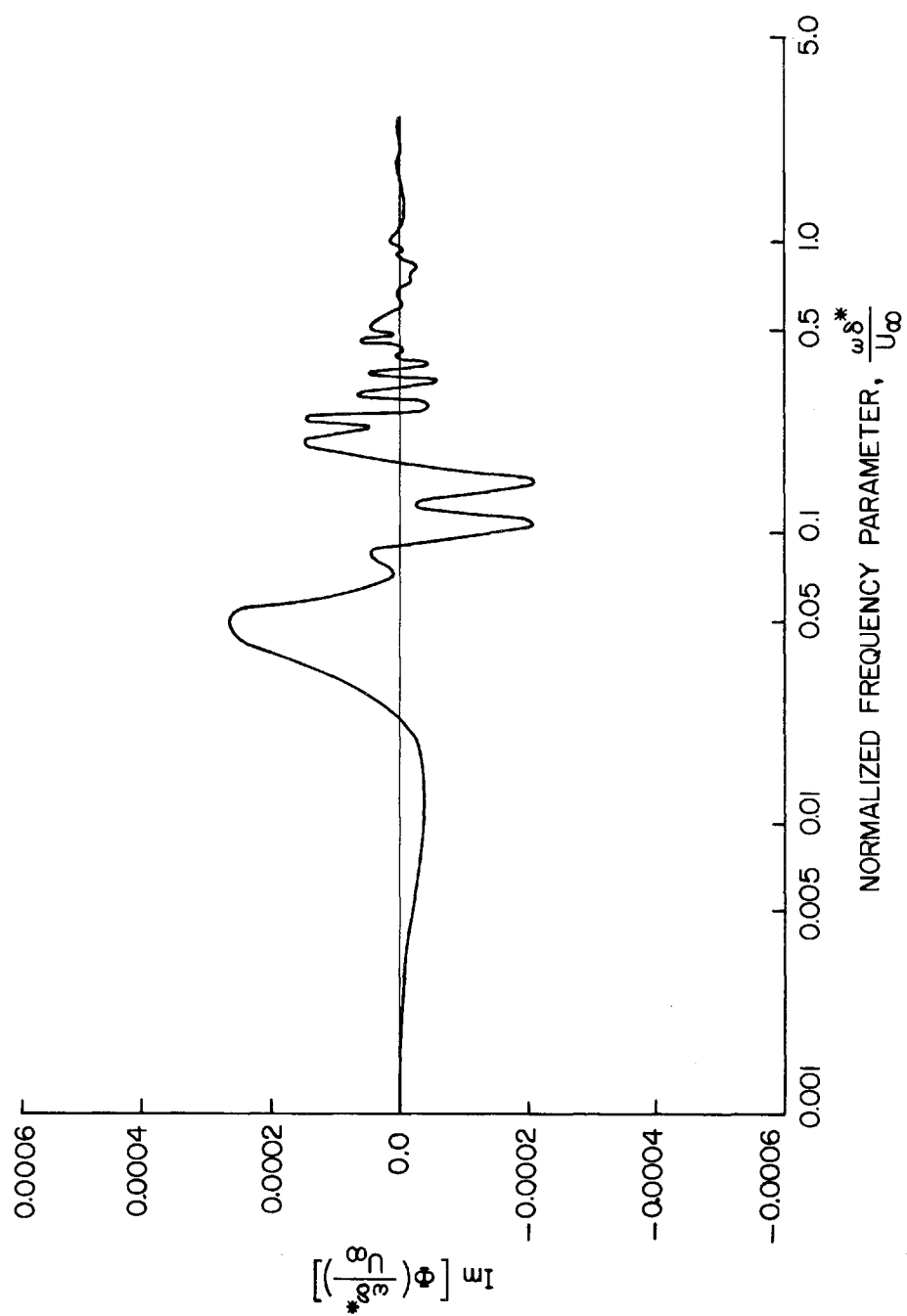Fins without Propeller for $x_3$ = 5.9 inches

Fig. 3-21  Imaginary Part of Cross-Power Spectral Density for Body and Fins without Propeller for $x_3$ = 5.9 inches

This page intentionally left blank.